DOE-FG02-88ER40414
Study of Heavy-Ion Reactions and Transuranic Nuclei

THE UNIVERSITY OF ROCHESTER

Nuclear Science Research Group

ROCHESTER, NEW YORK 14267-0216, USA

Progress Report

W. U. Schröder, Editor

August/September 2010

Surface Boiling - a New Type of Instability of Highly Excited Atomic Nuclei

J. Tõke and W.U. Schröder

Departments of Chemistry and Physics

University of Rochester, Rochester, New York 14627

ABSTRACT

The evolution of the nuclear matter density distribution with excitation energy is studied within the framework of a finite-range interacting Fermi gas model and microcanonical thermodynamics in Thomas-Fermi approximation. It is found that with increasing excitation energy, both infinite and finite systems become unstable against infinitesimal matter density fluctuations, albeit in different ways. In modeling, this instability reveals itself via an apparent negative heat capacity of the system and is responsible for the volume boiling in the case of infinite matter and surface boiling in the case of finite systems. The latter phenomenon, unique to small systems, appears to provide a natural explanation for the observed saturation-like patterns in experimental functional dependence of nuclear temperature on the excitation energy deposited.

I. INTRODUCTION

Understanding the limits of stability of nuclear matter has been a focus of numerous theoretical and experimental studies [1–3]. While theoretical studies are mainly concentrated on instabilities in infinite matter resulting, e.g., in phase separation, the relevance of their findings for finite nuclei found in nature is far from obvious. The reason here is that it might not be possible to bring the bulk matter in finite nuclei to the state showing in theoretical analysis the kind of instability of interest. Quite obviously, unlike in theoretical modeling, it is not possible to control the volume, pressure, or the temperature of actual nuclei. As a result, best one can hope for is that by solely feeding (excitation) energy to the system one might arrive at a point where the metastability against statistical decays is no longer sustainable, signaling the onset of instability. The kind of instability of a particular interest is one that is bound to occur as a function of controlling parameters regardless of the way the system is formed, i.e., not due to trivial dynamical effects of, e.g., shock waves or "over-zealous" (and unrealistic) inertial expansion into spinodal domain. To discover such instabilities in theoretical modeling, one must then vary the controlling parameter in infinitesimally small steps, allowing the system to reach at each step a metastable thermodynamical equilibrium where the system may decay only as a result of *finite* statistical fluctuations in parameters describing the system as a whole. The onset of instability is in such a case signaled by the loss by the system of immunity against *infinitesimally small* fluctuations in one or more parameters, where such fluctuations no longer give rise to restoring driving forces, but rather to disruptive forces. Mathematically, such instabilities reveal themselves in modeling through the appearance of negative compressibility, negative heat capacity, or negative derivative of chemical potential with respect to concentration [1, 4, 5].

The present work is part of a continued effort [6–12] to construct a (microcanonical) thermodynamical framework for understanding phenomena of apparently statistical nature observed in highly excited nuclear systems produced in the course of heavy-ion collisions. More specifically, it focuses on the negative heat capacity predicted [9] for a thermally expanding bulk nuclear matter considered within the interacting Fermi gas model within Thomas-Fermi approximation. Now, for the first time, the onset of this

negative heat capacity is identified as the boiling point for bulk nuclear matter, however, occurring at conditions substantially different from those typically attributed to boiling. Furthermore, model calculations performed for finite systems using finite-range interacting Fermi gas model combined with Thomas-Fermi approximation demonstrate that, on the excitation energy scale, much before the bulk matter would come to boiling, the surface matter starts boiling off, not allowing one to reach temperatures in excess of this surface boiling-point temperature. The phenomenon of surface boiling, discovered here via theoretical modeling, appears unique for small systems interacting via finite-range forces, such as is the case of atomic nuclei. It finds a solid experimental confirmation in the form of caloric curves "saturating" at temperatures of several MeV [2], expected for surface boiling.

The present paper is structured as follows. In Section II the adopted theoretical formalism is presented based on finite-range interacting Fermi gas model and Thomas-Fermi approximation in conjunction with microcanonical statistical thermodynamics. In Section III, the boiling instability in bulk matter at zero pressure is revisited with clear demonstration of its nature. In Section IV, the evolution of the density profile of finite droplets of nuclear matter with increasing excitation energy is studied revealing the onset of instability against the infinitesimal fluctuations in the local matter density profiles, where such infinitesimal fluctuations are seen to give rise not to restoring forces but to effective driving forces amplifying the fluctuations to the point where parts of the surface matter separate from the system in what constitutes surface boiling. The conclusions are presented in Section V

II. THEORETICAL FRAMEWORK

A phenomenological model has been proposed and used earlier [6–12] to allow treatment of excited nuclei as droplets of unconfined Fermi gas/liquid in microcanonical equilibrium. In this model, it is assumed that the system, whether finite or infinite, is bound together by a binding energy resulting from the interaction of nucleons with a mean field, reduced by the kinetic energy resulting from zero-temperature Fermi-motion. The former (potential) energy will be called interaction energy (E_{int}) and the latter (ki-

netic) energy will be named Pauli energy (E_{Pauli}), as it results from the action of the Pauli principle. The zero-temperature binding energy depends on the matter density and, generally, on the matter density distribution, as both, the interaction and Pauli energy depend on the matter density distribution. It will be named configuration energy (E_{config}). The total energy of the system (E_{tot}) consists of the configuration energy and thermal excitation energy (E_{therm}). Note that the configuration energy, while calculated at zero temperature includes non-thermal excitation energy - the difference between E_{config} and the true ground-state energy.

$$E_{config} = E_{int} + E_{Pauli} \ \ and \tag{1}$$

$$E_{tot} = E_{config} + E_{therm} \tag{2}$$

The absence of confinement manifests itself by the requirement for the external pressure to be zero. This implies that the pressure at the boundary of the matter must be zero, as well, a condition that allows one to determine the dependence of the matter density distribution on the excitation energy or E_{tot}. Furthermore, since according to the first law of thermodynamics, and for equilibrated systems at zero pressure:

$$dE_{tot} = TdS, \tag{3}$$

requirement that the pressure p at the boundary be zero is equivalent to a requirement for the entropy S to be at maximum for fixed total energy of the system, i.e., for all allowed microstates of the system to be populated with equal probability. This is the essence of microcanonical equilibrium. Note that because of the pressure p=0, there is no requirement for the volume being kept constant, a common requirement for the microcanonical equilibrium. Actually, this volume increases with increasing excitation energy to keep p=0, which is simply a manifestation of thermal expansion of the matter. In Eq. 3 T is the temperature.

In view of the staggering number of configurations allowed at even moderate excitation energies, it is not practical to evaluate the true system entropy S. What is possible, however, is to evaluate configuration entropies S_{config} for families of configurations of interest and, as a result, find the configuration, the system is most likely to dwell in. One

uses here the fact that according to microcanonical thermodynamics, the probability for the system to dwell in any particular configuration scales with the exponent of the configuration entropy representing the configuration microcanonical partition function Z_{config}. Although for many practical purposes, the entropy of the most likely configuration may be used to approximate the system entropy, one should keep in mind that on some occasions, such as phase transitions, this approximation breaks down as a result of growth of statistical fluctuations. As will be shown in the following sections, the approximation breaks down at volume (infinite matter) and surface (finite matter) boiling points, a fact that manifests itself through the appearance of negative *configuration* heat capacity.

In the present study, the configuration entropy is evaluated using the Fermi gas formula

$$S_{config} = 2\sqrt{a_{config}(E_{tot} - E_{config})}, \tag{4}$$

where a_{config} is the configuration level density parameter (*little a*).

Equation 4 is the base equation of the model, allowing one to evaluate S_{config} for any configuration of interest characterized solely by the configuration matter density distribution $\rho_{config}(\vec{r})$. Such an evaluation involves evaluating a_{config} and E_{config}. The former is done using Thomas-Fermi approximation [6] and the latter is done by integrating over volume the energy density given by a suitable equation of state, with a folding provision for mocking up the effects of the finite range of nucleon-nucleon interaction. For a_{config} one writes [6]

$$a_{config} = \alpha_o \rho_o^{2/3} \int\int\int \rho^{1/3}(\vec{r}) d\vec{r}, \tag{5}$$

where α_o expresses the value of the level density parameter per nucleon at normal matter density ρ_o.

For uniform matter, the finite range of interaction is of no consequence and the configuration energy can be written simply as

$$E_{config}(\rho) = V\epsilon_{EOS}(\rho) \tag{6}$$

where V is the system volume and $\epsilon_{EOS}(\rho)$ is the configuration energy density given by the equation of state as a function of matter density ρ.

For nonuniform matter distribution, the finite range of nucleon-nucleon interaction plays and important role. In this study, its effects are mocked up by folding the interaction part of the configuration energy density over volume with a Gaussian folding function, i.e.

$$E_{int} = R \int\int\int\int\int\int \epsilon_{int}(\rho(\vec{r} - \vec{r'}))e^{-\frac{(\vec{r}-\vec{r'})^2}{2\mu^2}} d\vec{r}d\vec{r'}, \tag{7}$$

where R is the normalization factor for the folding Gaussin, μ is a folding width parameter adjusted to reproduce the surface diffuseness of the ground state configuration of 1 fm (the Süssmann width).

To obtain the configuration energy, one must additionally calculate the configuration Pauli energy from

$$E_{Pauli} = \frac{3}{5} E_o^{Fermi} \rho_o^{-2/3} \int\int\int \rho^{5/3}(\vec{r}) d\vec{r} \tag{8}$$

and take the sum $E_{config} = E_{int} + E_{Pauli}$. In Eq. 8, E_o^{Fermi} denotes the Fermi energy at normal matter density, characteristic of the EOS adopted.

For the equation of state, the present study adopted the standard form consistent with Skyrme-type nucleon-nucleon interaction, which implies the interaction energy density (appearing in Eq. 7) in the form

$$\epsilon_{int}(\rho) = \rho[a(\frac{\rho}{\rho_o}) + \frac{b}{\sigma + 1}(\frac{\rho}{\rho_o})^{\sigma}] \tag{9}$$

The values of the parameters a, b and σ in Eq. 9 are determined by the requirements for the binding energy, matter density, and the incompressibility modulus to have prescribed values. The values chosen in this study of a=-62.43 MeV, b=70.75MeV, and σ = 2.0 imply a normal density of $\rho_o = 0.168 fm^{-3}$, binding energy per nucleon at normal density of ϵ_{EOS}/ρ_o=-16MeV, the incompressibility modulus of $K = 240 MeV$, and Fermi energy at normal density of E_o^{Fermi}=38.11MeV.

Note that the above formalism makes several simplifying approximations, such as neglecting the Coulomb forces, setting the effective nucleonic mass to 1, neglecting isospin effects, etc. These approximations may be dropped when issues other than studied in this work are to be addressed.

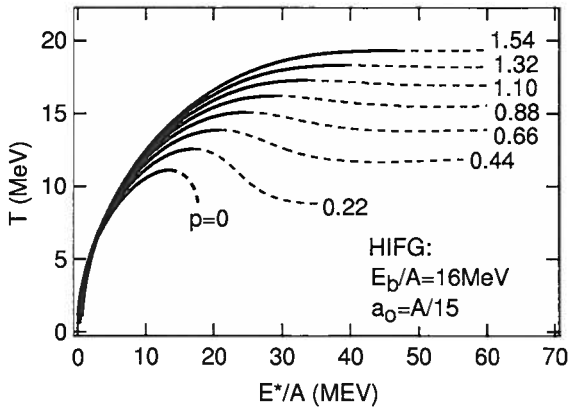

FIG. 1: Caloric curves for uniform matter configuration calculated for different external pressures.

III. BOILING INSTABILITY IN BULK NUCLEAR MATTER

The response of the bulk nuclear matter to the excitation energy was studied using the formalism outline above and assuming a uniform matter distribution. In this study, matter density was varied so as to find an equilibrium density securing maximum (configuration) entropy S_{config} for any given excitation energy $E*$. Subsequently, (microcanonical) temperature T was determined for the equilibrium uniform configuration using

$$T = \sqrt{\frac{E^* - E_{config}}{a_{config}}} \tag{10}$$

This analogous to the study reported earlier [9], where a simple harmonic (soft) EOS was assumed rather than the more realistic Skyrme-forces based one. The results of calculations are illustrated in Fig. 1, where both, the equilibrium density ρ_{eq} and temperature T are plotted as functions of excitation energy per nucleon. As seen in this figure, while the equilibrium density decreases monotonically with increasing excitation energy, temperature reaches maximum value at E^*/A=17 MeV and then begins dropping with increasing E^*. Which means that the system enters a domain of instability at around $E/A*$=17 MeV where the heat capacity turns negative. In this domain, acquisition by any part of system of an infinitesimally small amount of excitation energy from

a neighboring parts would lead to lowering of temperature in this part, which now will cause driving more heat to it and a further lowering of temperature, until that part leaves the system. In fact, the system would never arrive at a configuration showing nominally negative heat capacity but would rather boil off "offending" parts of the matter to allow the remainder to cool down to sustainable excitation energy per nucleon. The presence of a domain of negative heat capacity can be inferred already from the appearance of "van-der-waalsian" isotherms in plots of pressure *versus* specific volume or (uniform) matter density. This is illustrated in Fig. 2 along the zero-pressure line representing the system trajectory as a function of excitation energy in this representation. Note that the specific volume is uniquely related to the excitation energy of the system. As seen in this figure, as the excitation energy is increased from zero (density lowered from normal density), the system trajectory first crosses isotherms with increasing temperatures. Then, upon reaching a specific isotherm tangential to the trajectory at point B the this trajectory begins crossing isotherms with ever decreasing temperatures consistent with what is seen in Fig. 1. Here, one observes that the boiling sets in at a pressure that is significantly lower than the pressure of saturated vapor for the given boiling temperature. The latter is evident from the Maxwell construct of the liquid-gas coexistence for the isotherm involved shown in dashed line in Fig. 2.

A further insight into the (volume) boiling phenomenon is provided in Fig. 3 where the reduced two-phase configuration entropy $S_{config} - S_{uniform}$ surface is shown as a function of total excitation energy and its possible division between the two equal parts of the system. As seen in this figure, at low excitations entropy favors uniform configurations where the two parts have equal excitation energies. With increasing excitation energy, fluctuations in the excitation energy distribution grow to the point where a uniform distribution no longer provides a fair description of the system and, accordingly, the configuration temperature no longer provides an adequate representation of the system temperature. With a further increase of excitation energy, the entropy favors asymmetric split of the excitation energy between the two parts. In fact, the entropy would grow indefinitely with an indefinite expansion of one part of the system at the expense of the remainder until that part leaves the system or in other words, boils off. Note that in Fig. 3 the mass numbers in the two parts of the model system are kept constant but the

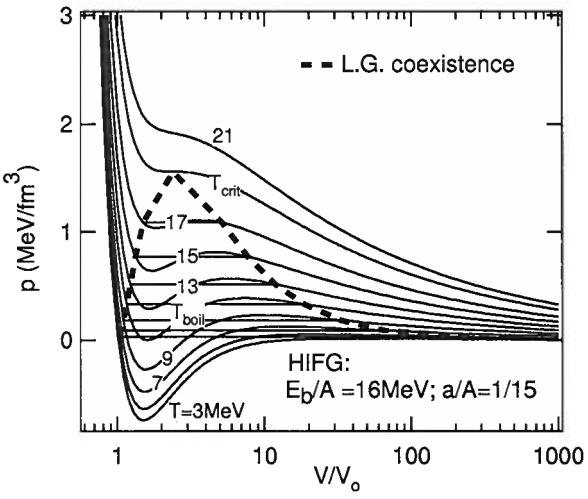

FIG. 2: Isotherms for the model matter. The isotherm corresponding to boiling temperature is shown in bold line and the adiabatic system trajectory in bold dashes. Shown is the Maxwell construct for the liquid-gas coexistence line corresponding to the boiling-point temperature.

volumes occupied by these parts are free to adjust so as to maximize the configuration entropy for a given split of excitation energy.

The results show that in quantitative terms the model volume boiling temperature of over 11 MeV is substantially higher than the limiting temperatures observed in experimental studies of caloric curves [2] making it unlikely for the volume boiling to be responsible for the observed plateaus on these curves. On the other hand, as demonstrated in the following section, in finite systems, the more vulnerable surface domain begins boiling off at lower temperatures consistent with the observed plateaus on caloric curves.

IV. SURFACE BOILING IN FINITE SYSTEMS

The model calculations for a finite system were performed for a system of 100 nucleons. The folding width parameter μ was 1.4fm. The system density distribution was parameterized in terms of error function [6] as

$$\frac{\rho}{\rho_o} = \frac{1}{2}[1 - erf(\frac{r - R_{half}}{\sqrt{2}d})], \tag{11}$$

the system decreases (panel e). The central pressure is seen to decrease (panel e) due to the reduction in surface tension. Importantly, the caloric curve (panel f) features a maximum followed with a domain of negative heat capacity. The negative heat capacity is seen to set in around an excitation energy per nucleon of approximately 5 MeV. It signals onset of an instability where a part of the surface domain may draw excitation energy from neighboring parts and while doing so expands and cools down. As a result, it will now draw even more energy from hotter neighbors and cool down even further until it separates from the system in a process that can be identified as surface boiling. The situation here is very much analogous to the case of volume boiling, except that the surface boiling sets in at much lower temperatures consistent with weaker bonding in the surface domain.

The loss of monotonicity at around $E*/A$=4.5 MeV seen in panels a-e of Fig. 4 is due to the fact that the rather arbitrarily chosen two-phase configuration entropy ceases to provide a good approximation for the system entropy as the system approaches the boiling point.

V. SUMMARY

The modeling of the behavior of hot bulk matter and hot finite nuclei has revealed that both kind of systems are subject to boiling off of matter when brought to sufficiently high excitation energies. In realistic finite systems the surface boiling sets in at considerably lower excitation energies than would the volume boiling of the bulk matter, which should prevent the system from ever experiencing volume boiling. The surface boiling, occurring in model calculations at temperatures around 5MeV provides a natural explanation for the observed plateaus on caloric curves and observed limiting excitation energies that can be equilibrated in nuclear systems. The surface boiling appears unique to small systems where the surface domain plays relatively important role. The present study employs a number of approximations and simplifications, which may be dropped in follow-up studies. For example, the developed formalism can be readily adapted for handling iso-asymmetric systems allowing one to study isospin effects in boiling off of surface matter.

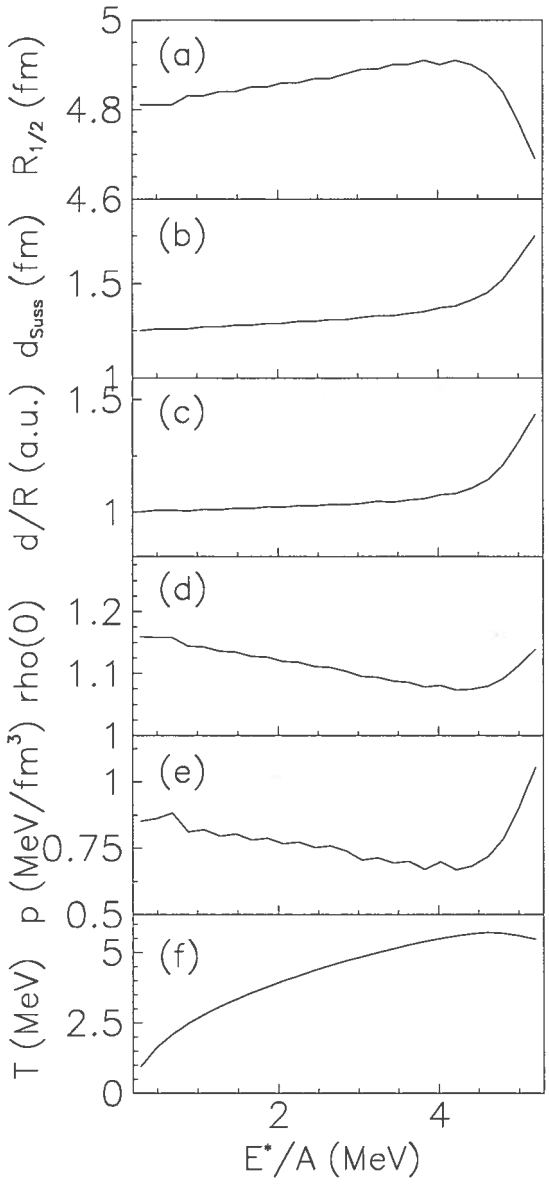

FIG. 4: Evolution of finite system parameters with excitation energy (See text).

Acknowledgments

This work was supported by the U.S. Department of Energy grant No. DE-FG02-88ER40414.

---

[1] H. Müller and B. Serot, Phys. Rev. C **52**, 2072 (1995).

[2] J. Natowitz et al., Phys. Rev. C **65**, 34618 (2002).

[3] S. Shlomo and V. Kolomietz, Rep¿ Prog. Phys. **68**, 1 (2005).

[4] J. Lattimer and D. Ravenhall, Astr. Journ. **223**, 314 (1978).

[5] M. Barranco and J. Buchler, Phys. Rev. C **22**, 1729 (1980).

[6] J. Tõke and W. J. Swiatecki, Nucl. Phys. A **372**, 141 (1981).

[7] J. Tõke and W. U. Schröder, Phys. Rev. Lett. **82**, 5008 (1999).

[8] J. Tõke, J. Lu, and W. U. Schröder, Phys. Rev. C **67**, 034609 (2003).

[9] J. Tõke, L. Pieńkowski, L. Sobotka, M. Houck, and W. U. Schröder, Phys. Rev. C **72**, 031601 (2005).

[10] J. Tõke, J. Lu, and W. U. Schröder, Phys. Rev. C **67**, 044307 (2003).

[11] J. Tõke and W. U. Schröder, *Proc. IWM2005 Int. Worksh. on Multifragmentation and Rel. Topics* (Società Italiana di Fisica, Bologna, Italy, 2006), p. 379.

[12] J. Tõke and W. Schröder, Phys. Rev. C **79**, 064622 (2009).

NSTAR - A Capture Gated Plastic Neutron Detector

I. A. Pawełczak, J. Tõke, E. Henry, M. Quinlan, H. Singh, W. U. Schröder

Department of Chemistry, University of Rochester, Rochester, NY 14627

Abstract

The NSTAR ("Neutron Sandwich Transmuter/Activation-γ Radiator") prototypes were developed and their performances were evaluated using radioactive sources and a pulsed-neutron beam. The NSTAR operating principle is similar to that of Gd-loaded liquid scintillation detectors, where the scintillator has dual functions as neutron moderator and sensor of delayed capture γ-rays, but spatially separates scintillator from neutron converter components. The time dependent NSTAR response to neutrons consists of a prompt, energy related light flash followed by a delayed signal characteristic in both light output and delay time. This feature allows to discriminate between neutrons and γ-rays on average and provides the basis for multiplicity determination. The detectors are scalable, economic to construct of environmentally benign components, and can be ruggedized. Prototype detector modules consist of [12 x 20 x (50 or 100) cm^3] stacks of plastic scintillator slabs (Saint Gobain BC-408) alternating with thin Gd converter films viewed by fast photomultipliers (Philips XP2041). The effective Gd/scintillator ratio is 0.5 wt.%. Results of tests of NSTAR with ^{252}Cf and neutrons from the D(d,n)^{3}He reactions are in good agreement with theoretical estimates based on neutron transport simulations. Characteristics of the detector module include an average neutron capture time of $\langle t_c \rangle = (21.7 \pm 0.2)$ μs and a detection efficiency of $\varepsilon = (26 \pm 3)$ for DD neutrons. The NSTAR has been applied to determine the multiplicity distribution of neutrons produced in D(d,n)^{3}He reactions by a neutron generator.

Keywords: Neutron detector, Gd-loaded scintillator, Neutron multiplicity

1. Introduction

Neutrons are an important, penetrating type of radiation, occurring in nature with a range of energies spanning many orders of magnitude. In nuclear research and development (from low-energy fission and inertial fusion to medium and high energy heavy-ion experiments), neutrons often constitute a major experimental signal. Increasingly, neutron irradiation and activation are utilized in many applications such as in material testing, transmutation of isotopes (radio pharmaceuticals, transactinides in spent nuclear fuel), thermal and fast neutron imaging (oil prospecting, detection of illicit materials like drugs and SNM). For example, modern techniques of direct interrogation of shipment contents involve measurements of flux, multiplicity and energy spectrum of transmitted or scattered primary neutrons, as well as detection of prompt and delayed secondary neutrons, γ-rays or other types of induced radiation. Adverse effects of harsh environments and high backgrond rates can be mitigated with "phase-sensitive" coincident or pulsed-scan methods involving specialized radiation detectors of the type introduced here.

The various "neutronics" applications of current interest require neutron monitors of different capabilities. However, universally desirable characteristics of neutron detectors are high detection efficiency with a low energy threshold, a fast and specific response to neutrons, a relatively energy independent response function as well as multi-hit resolving power. In practice, realizations of neutron detectors always invoke compromises in functionality. For example, due to the long mean free path of energetic neutrons in materials, highly efficient neutron detectors are voluminous. This fact has consequences for response time, ease of operation, and economics; it is often associated with environmental hazards.

Since neutrons do not ionize the detector medium directly, their detection proceeds via nuclear processes generating charged particles or γ-rays in n-induced scattering and reactions in the media of ionization counters and scintillation detectors. Examples of such induced radiation include recoil protons from elastic scattering on detector hydrogen content or charged particles produced in thermal-neutron capture in ^{3}He proportional counters. Discrimination between neutrons and coexisting background radiation can be accomplished utilizing the characteristic spectrum of the induced radiation or a characteristic time dependent detector response. For example, discrimination based on the latter in scintillation detectors exploits radiation specific differences in effective scintillation decay rates or relies on diffusion delayed

scintillation induced by neutrons.

Among the nuclear reactions often applied in neutron detection are processes induced by thermal neutron capture in separated ^{3}He, ^{6}Li, ^{10}B isotopes [1]. However, scarcity and cost of such separated isotopes have triggered wide-spread search for more economic alternatives. A major motivation for the present work has been to overcome this challenge by developing a new Gd capture gated plastic neutron detector.

Because of their interesting capabilities, ^{nat}Gd-loaded liquid scintillation detectors have been used in a number of nuclear and particle science experiments as neutron counters and multiplicity meters [2, 3, 4, 5]. Unfortunately, the organic solvents (benzene, trimethyl-benzene, xylene, etc.) typically employed in such detectors are highly flammable, toxic, and carcinogenic liquids, which impose significant environmental hazards. In these respects, non-volatile, inert scintillators, e.g., plastics, silicone rubber compounds or glasses are clearly preferable. Unfortunately, Gd additives to such scintillators cause opacity or at least significantly reduce the light attenuation length, making such scintillators viable only for small detectors [6, 7].

In this scenario, the NSTAR detector ("Neutron Sandwich Transmuter-Activation-γ Radiator") described in the present work represents an interesting alternative circumventing the problems described above by separating spatially scintillator from radiator components. Its operational principle is discussed in the following Section 2, along with optimization and simulation calculations that have resulted in the development of several prototype modules of the detector. Section 3 provides a description of prototype design criteria and component testing. Actual detector response to individual neutrons and neutron bursts, γ-rays and cosmic muons will be discussed in Section 4. Summary and conclusions are offered in Section 5.

2. The NSTAR Concept and Design

2.1. Principle of Operation

The NSTAR is a layered, two-component organic plastic scintillation detector. Its operational concept utilizes and extends to a broad dynamic range a well-known n_{th}-γ conversion reaction. The spatial separation of scintillator and converter avoids the opacity problem associated with direct scintillator doping. Fast neutrons are rapidly moderated down to thermal energies, depositing their kinetic energy essentially within the scintillator component of

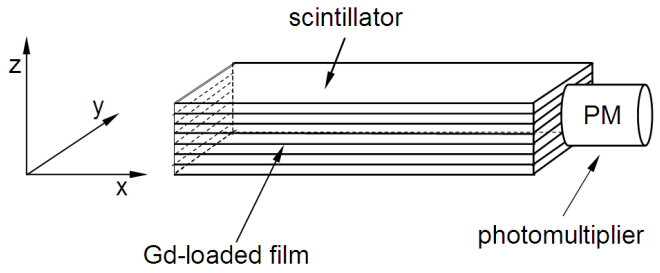

Figure 1: Schematic view of an NSTAR detector prototype module.

the detector, where they produce a "prompt" light output signal. Subsequently, the thermalized neutrons diffuse slowly through the detector until captured by nuclei in the second detector component, the n_{th}-γ converter or radiator, which gives rise to a delayed light output signal. Figure 1 provides the schematic drawing of a detector module made of a stack of planar scintillator slabs alternating with Gd-loaded converter films viewed by a photo multiplier.

In the present detector, Gd in natural abundance is used as active n_{th}-γ radiator component, since gadolinium has excellent absorption properties for thermal neutrons. This is true in particular for the isotopes ^{157}Gd (15.7 %) and ^{155}Gd (14.7 %), which have the highest thermal neutron capture cross-sections among all known nuclides, σ_{cap} = 254,000 b and σ_{cap} = 90,600 b, respectively. In its natural isotopic composition gadolinium still has a high mean thermal neutron capture cross section of $\sigma_{cap} = 4.9 \times 10^4$ b, making natural Gd useful as an efficient and economically attractive neutron converter material.

A cascade of 2-3 γ-rays following the neutron capture process is emitted with total energy corresponding to the neutron binding energies of 8.46 MeV (^{155}Gd) or 7.87 MeV (^{157}Gd). In the NSTAR these capture γ-rays are detected with the plastic scintillator component, where they undergo multiple Compton scattering on electrons and are absorbed with an efficiency increasing with active detector volume. With respect to the time of neutron injection, the capture related scintillation light is diffusion delayed on a several-γs long time scale. Obviously, the delayed light output intensity is independent of initial neutron energy. Total absorption of the capture γ-rays, achieved with sufficiently large scintillator volumes, signals each captured

neutron by one characteristic, full-energy light output flash corresponding to ∼8 MeV.

For moderately sized NSTAR modules, neutron-γ discrimination is still possible by monitoring the time dependent scintillation light output generated by fast ("prompt") ionization, which for incident neutrons is followed by delayed capture-γ emission. While the prompt light output flash provides a measure of the total energy deposited in an event, the delayed signal component occurring for neutrons has a light output spectrum characteristic of the detector. If in an event several neutrons are injected in the detector simultaneously, all contribute to the prompt summed light output intensity, while each of the neutrons has independently the chance to produce a delayed signal. The statistical separation in associated capture times renders the neutron multiplicity an event-by-event observable. The mean time to capture and its statistical spread can be tuned by choosing the total Gd concentration and its distribution throughout the layered detector geometry.

The above neutron identification method obviously requires an essentially complete moderation to thermal energies ("stopping") of incident fast neutrons. As demonstrated by simulation calculations described below (Sect. 2.2), this task is accomplished by multiple elastic scattering of neutrons predominantly off the protons in the organic scintillator, provided the scintillator volume is sufficiently large. For few-MeV neutrons, the moderation process requires plastic-scintillator thicknesses of the order of several cm and completes within the first (50-100) ns after injection into the detector. The subsequent diffusion of thermalized neutrons terminates with neutron capture, preferentially in the Gd radiator film. An efficient detector design minimizes competing capture events by protons in the scintillator producing a weaker (2.2-MeV$_{ee}$) signal.

2.2. Simulations Calculations

The many possible applications of plastic-scintillator neutron detectors like the NSTAR suggest modular constructions, such that size and geometry are flexible and easily modified. Furthermore, versatility and ease of construction favor a rectangular design for the prototype modules such as illustrated in Fig. 1. The overall dimensions of these modules should match the neutron spectra available for realistic test measurements, i.e., provide sizeable stopping efficiencies for neutrons of the order of (1-2) MeV of interest here. Finally, in order to be suited also for neutron time-of-flight and fast coincidence measurements, the scintillator should be relatively fast.

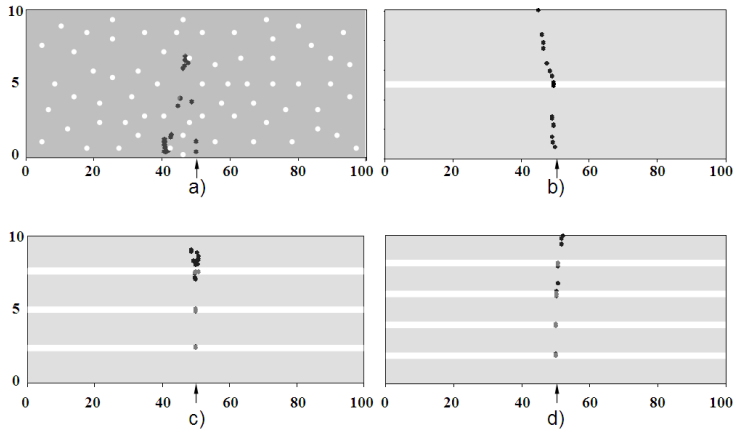

Figure 2: Cross-sections of the stack geometries a) - d) considered in simulations (not to scale). Abscissa and ordinate are given in units of cm. White dots and lines indicate Gd, shaded areas represent scintillator. Black dots outline trajectories of individual 1-MeV neutrons entering each stack vertically from below.

Following the above considerations, several important design tasks remain. For a given detector volume, the overall detection efficiency for identified neutrons, as well as the mean detector response time and multiplicity resolution, depend on the amount of Gd radiator component and its distribution throughout the detector volume. From other realizations of Gd-loaded detectors [2, 3, 4, 5], one already expects the average Gd/scintillator weight ratios of the order of a few times 10^{-2} to suffice. However, in order to derive an optimum solution to the multi-dimensional intercorrelated Gd concentration problem, quantitative numerical simulation studies have been conducted for a number of plausible NSTAR architectures. These simulation calculations have been performed with an expanded version (DENISE) of the existing Monte Carlo neutron-γ transport code DENIS [8, 9]. The modified code simulates neutron moderation, diffusion and capture, as well as the transport of γ-rays through the detector stack. On the other hand, losses in light output are not simulated in detail, i.e., the theoretical light collection efficiency was set to unity in all simulations.

In the following, results of simulation calculations are reported for several detector architectures: a) A uniform Gd distribution within a single 10-cm thick scintillator block, b) Two 5-cm thick scintillator slabs sandwiching one 0.1-cm thick Gd radiator film, c) Four 2.5-cm thick scintillator slabs

interspersed with three 0.1-cm thick Gd films, d) Five 2-cm thick scintillator slabs alternating with four 0.1-cm thick Gd films.

All simulations, each representing 10^5 events, assume a total scintillator volume of $10 \times 20 \times 100$ cm^3 and a total Gd/scintillator concentration of 0.5 % by weight. Case a) is an idealization chosen only for comparison. Here, the simulations ignore the fact that already small amounts of Gd doping render the scintillator opaque and thus dysfunctional. The different architectures are schematically illustrated in Fig. 2, along with sample trajectories for 1-MeV neutrons entering each detector stack vertically from below. The bunching of trajectory points observed in Fig. 2 a) or c) indicates that the respective neutron has entered the diffusion regime characterized by large directional changes but approximately constant thermal energy. In cases b) and d) trajectories of neutrons that escape from the detector are illustrated. As expected, the simulations demonstrate that the mean detector response time and efficiency with which neutrons are captured by Gd nuclei depend on the local Gd concentration encountered in the neutron diffusion regime. In the simulations, this domain begins at the "thermalization point", where the neutron energy has first dropped below $E_n = 50$ meV. The important quantity is then "capture distance", $\lambda = |\vec{r}_{th} - \vec{r}_{cap}|$, the distance between the neutron thermalization and the capture sites $\vec{r}_{th}$ and $\vec{r}_{cap}$ respectively, where the neutron is captured by a ^{155}Gd, ^{157}Gd, or ^{1}H nucleus.

The results of these calculations are illustrated in Figs. 3 and 4 for the above architectures a) - d). In Fig. 3 the probability is plotted on logarithmic scale vs. capture distance λ. The curves in this figure represent exponential (Gaussian) fits to the individual sets of data points. One observes from these data that, with increasing number of Gd films, i.e., decreasing thicknesses of the individual scintillator slabs, the capture distance distribution approaches that characteristic of a uniform gadolinium concentration. Essentially, a detector with five 2-cm scintillator slabs and four converter films approximates very well a hypothetical geometry of 10-cm thick scintillator block with uniform Gd doping.

A corresponding observation is made with respect to the neutron capture time distributions illustrated in Fig. 4. Here, the probability is plotted vs. the time elapsed between injection of a 1-MeV neutron into the scintillator and its capture. The curves in Fig. 4 have the shape expected from the superposition of two time-dependent stochastic processes, neutron scattering and diffusion. The capture probability dependence on detector architecture for the considered four detector stack geometries is illustrated in Fig. 4.

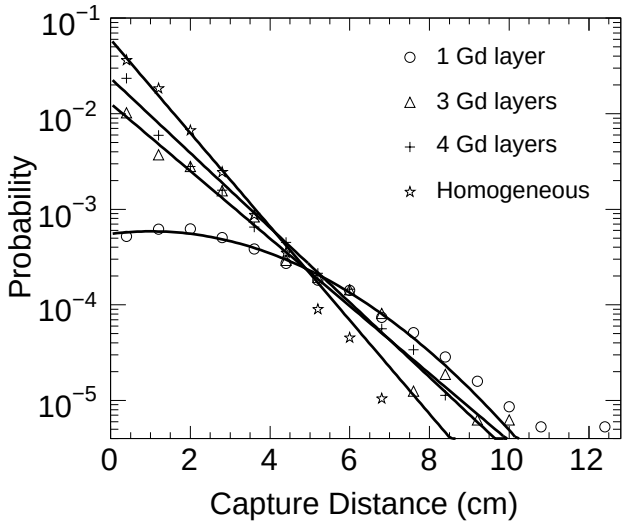

Figure 3: Capture distance distributions for the considered geometries of the NSTAR prototype. Stars illustrate the expectations for an idealized homogeneous Gd distribution through the detector. The solid lines represent fits to the distributions.

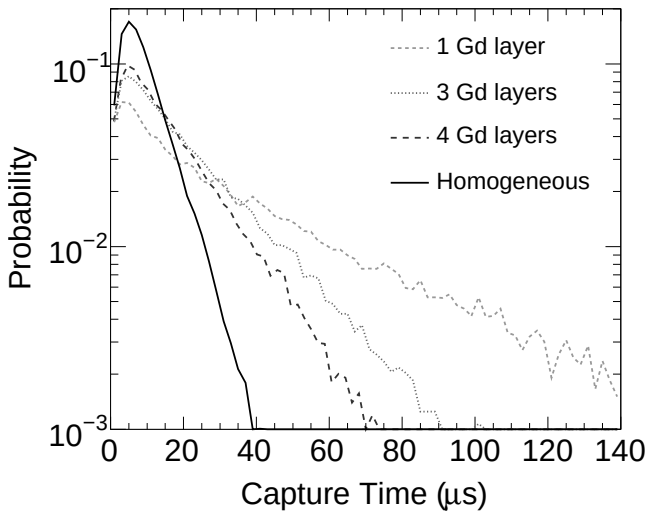

Figure 4: Neutron capture time distributions for the specified detector architectures.

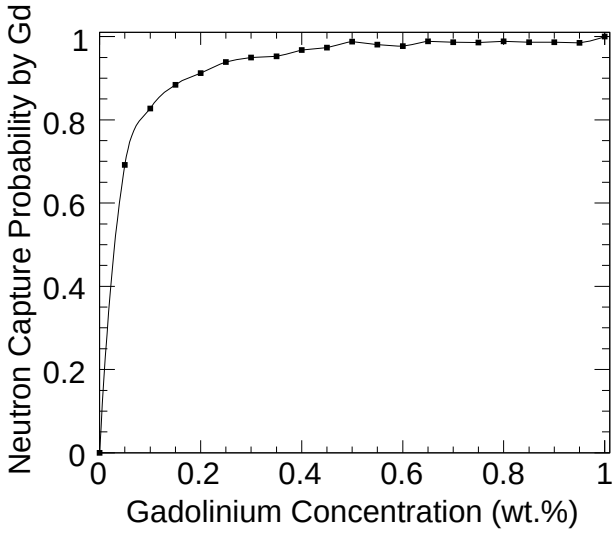

Figure 5: Neutron capture efficiency vs. total Gd concentration by weight normalized to the efficiency at 1 wt %.

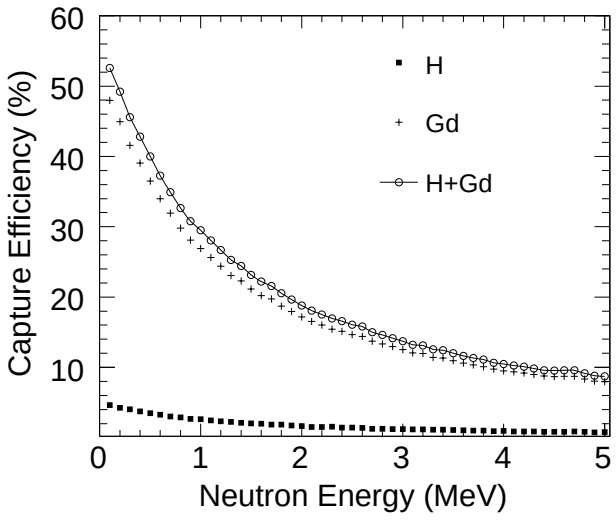

Figure 6: Neutron capture efficiency vs. energy for perpendicular incidence into largest face.

From that figure it is obvious that the mean capture time $\langle t_c \rangle$ decreases with increasing number of layers, i.e., decreasing scintillator slab thickness. Going from two, 5-cm thick scintillator slabs to five, 2-cm thick slabs, the mean capture time decreases from $\langle t_c \rangle = 47$ μs to $\langle t_c \rangle = 20$ μs, approaching $\langle t_c \rangle = 10$ μs for the uniform Gd distribution of an idealized detector. The data in Fig. 4 illustrate the dichotomy of the properties of a fast response of the detector to neutrons and an efficient average n-γ discrimination. A slow response is desirable because it makes the detector better applicable to high incident neutron count rates but more susceptible to accidental background. On the other hand, a faster detector response implies a shorter diffusion delay of neutron capture and therefore diminished n-γ discrimination efficiency and multiplicity ("multi-hit") resolution. As a compromise, the configuration of 2-cm thick scintillator slabs alternating with 1-mm thick Gd radiators was chosen for the NSTAR prototype modules. For this adopted NSTAR prototype architecture, additional simulation calculations were carried out, in order to determine the optimum total amount of Gd in the detector. Results of these calculations are presented in Fig. 5. Obviously, the capture probability increases first with the amount of Gd in the radiators, but this dependence saturates close to a maximum for concentrations above (0.4 - 0.5) wt %. Therefore, a Gd/scintillator weight ratio of 0.5 % represents a sufficient Gd concentration for the prototype.

Finally, the neutron capture efficiency predicted by simulation calculations is depicted in Fig. 6 vs. neutron energy for the above prototype architecture and a collimated beam of neutrons perpendicular to the detector stacking direction. Data are shown separately for capture in Gd and H, along with the total efficiency. Obviously, capture in Gd is the dominant mode of neutron capture. Since the scintillator is only 10 cm thick in the direction of neutron incidence, the capture probability and therefore the detection efficiency are strongly energy dependent. The efficiency reaches $\varepsilon = 0.5$ for $E_n < 200$ keV but decreases to less than $\varepsilon = 0.1$ for $E_n > 5$ MeV. For other directions of neutron incidence, the efficiency varies generally with the effective scintillator thickness in the neutron path.

3. Component Development and Optimization

The practical detector development focused on the fabrication of suitable Gd-loaded radiator films, the assembly of detector module stacks, complete

with light guides, photo multiplier and support structure, and the maximization of scintillator light collection.

3.1. Radiator Films

The basic function of the radiator films to be placed between any two of the scintillator slabs in an NSTAR module is to maintain uniform layers of a suitable compound of ^{nat}Gd, which is the active n_{th}-γ converter component. Among the desired properties of the film are admission of the selected Gd compound in its matrix as well as maintenance of chemical and thermal stability, preservation of shape under polymerization process, the flexibility and integrity of large pieces. Low mass density and absorbance for neutrons and γ-rays are additional requirements.

Thermo-plastic polymers present good choices for the medium holding the required Gd compound in the polymerization process. For example, poly-dimethyl-siloxane (PDMS) [10] has been used in similar applications and appears to satisfy the above requirements for the NSTAR radiator films. Polymerization of PDMS occurs upon combining the two-component base (dimethyl siloxane, dimethylvinyl-terminated and dimethyl, methylhydrogen siloxane) with the curing agent (proprietary Pt catalyst). Prior to the process, gadolinium (III) oxide (Gd_2O_3) was added to the base diluted with cyclohexane. The mixture was allowed to polymerize in a shallow planar mold, first for 12h at room temperature, followed by 36 hours at elevated temperatures under heat lamps. The resulting 0.1-cm thick film turned out to be uniformly loaded, flexible and easy to handle.

Thermal neutrons were used to determine gadolinium uniformity of the film in the absorption measurements by randomly selected sample film patches. A ^{252}Cf-fission/neutron source in a 12-cm thick paraffin moderator produced the thermal neutrons. Neutron fluxes with and without samples were measured with ^{3}He proportional counters. Fluctuations in the absorption of less than $\pm 1\%$ were observed for the set of film samples, and are in good agreement with DENISE simulation calculations.

Optical reflective properties of the radiator film were investigated by scanning randomly selected film patches with UV-Vis light. At wavelength of λ = 425 nm, corresponding to maximum light emission of fast scintillators, the reflectivity was found to fluctuate at low value for R = (41 $\pm$ 3) %. Due to relatively modest reflective properties of the radiator film additional reflective materials are required, and discussed in the next section.

3.2. Scintillator and Readout

In order to render the NSTAR suitable for neutron time-of-flight and fast coincidence measurements, a fast plastic was chosen as scintillator. For the present detector, the general purpose plastic scintillator BC408 (Saint Gobain) [11] was chosen as suitable and cost effective. The scintillator has a quoted decay time of $\tau = 2$ ns with a light emission maximum in the UV region at $\lambda = 425$ nm. The quoted light absorption length is L = 3.8 m. For the prototype construction, 2-cm thick scintillator slabs with polished edges were prepared for specified lengths (50 cm and 100 cm) and width (20 cm) used to construct 0.5-m and 1-m long prototype stacks, respectively.

Light attenuation and wrapping materials were tested with sample rods of BC-408 scintillator using cosmic-ray muons as minimum ionizing particles. Individual scintillator slabs were wrapped in diffusively reflecting nitrocellulose paper which proved superior to other commonly used materials such as aluminized Mylar.

The NSTAR prototype stacks were viewed by Philips XP2041, 10.2-cm diameter photomultipliers attached to one or both ends of the stack. Direct photo multiplier attachment or coupling to the stack via conical light guides both gave good light output collection. The signal processing was accomplished utilizing standard NIM and CAMAC electronic modules.

4. Performance of the NSTAR Prototypes

4.1. Calibration and Light Output Resolution

summed light output of the assembled scintillator stack of the long NSTAR prototype was calibrated in electron-equivalent energy units (eV_{ee}) using standard γ-ray sources and cosmic-ray muons. Equivalent light output calibration in terms of proton recoil energies is accomplished using standard conversion formulas [12]. Muon trajectories through the detector were defined using a "telescope" setup with additional two, 2-cm wide scintillation strip detectors placed above and below the stack, requiring a coincidence with the NSTAR. Light output resolution of $\Gamma_{FWHM} = (20\text{-}24)\%$ was typically achieved for a 24-MeV_{ee} muon signal detected by photo multipliers on both ends of a 1-m long NSTAR stack.

The difference in arrival times of light output signals at the photo multipliers on opposite ends of a 1-m long NSTAR stack has been used to determine one coordinate of the point of light generation within the scintillator. Relative time (position) distributions recorded with muons entering at different

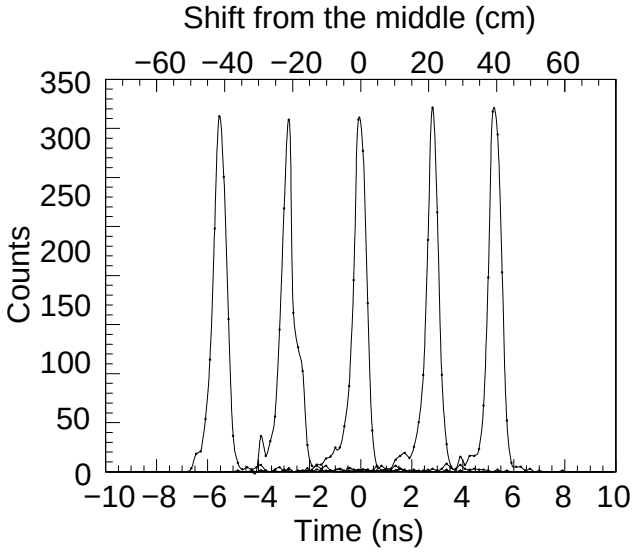

Figure 7: Difference in light output signal arrival times at opposite ends of a 1-m long stack for different injection points of cosmic muons.

positions along the NSTAR module are presented in Fig. 7, where position zero corresponds to the middle of the detector. The obtained time resolution of $\Gamma_{FWHM} = (0.55 \pm 0.02)$ ns corresponds to a position resolution of $\Gamma_{FWHM} = (4.2 \pm 0.2)$ cm. Given the spatial extents of interaction regions for incident neutrons or γ-rays, such a position resolution is adequate.

4.2. Response to ^{252}Cf neutrons

The response of a prototype NSTAR module to neutrons, specifically its particle identification capability, was tested with neutrons from a weak (0.189 μCi) ^{252}Cf source and neutrons produced in D(d,n)^{3}He reactions (DD-neutrons) by a generator with variable beam profiles.

The ^{252}Cf source emitted 860 neutrons per second in 4π and approximately a factor of 2-3 as many coincident prompt γ-rays. This allowed one to perform a γ-neutron time of flight (TOF) experiment, where the time-zero reference signal is provided by a 7.6 cm x 7.6 cm NaI detector triggering on γ-rays from the source. Signals from the NSTAR provided the stop signals for time-to-digital converter (TDC) generating the TOF spectrum of events.

Data collected at a TOF distance of 60 cm are displayed in Fig. 8. The distribution features a strong "prompt" gamma peak at t = 2 ns due to coin-

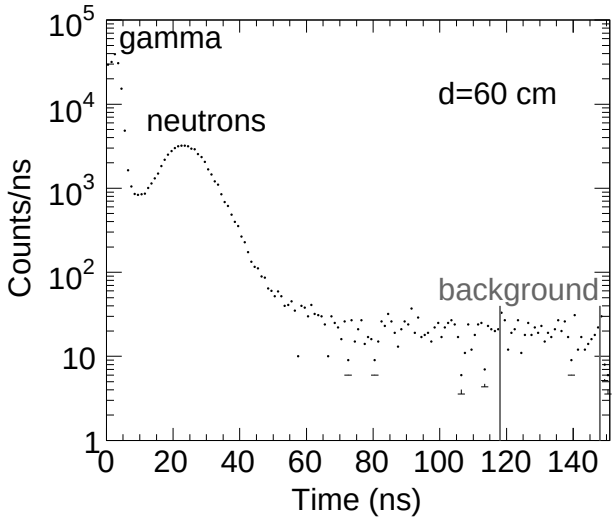

Figure 8: Time-of-flight spectrum for 252Cf γ-n coincidence events for a 60-cm flight path.

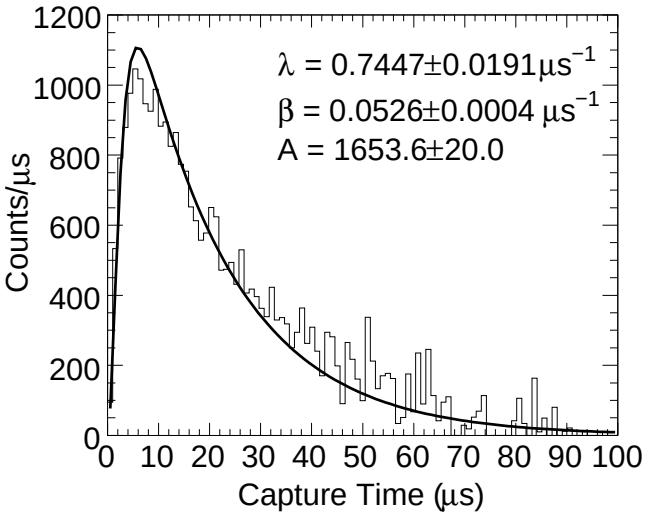

Figure 9: Capture time distribution of tagged neutrons. A, α and β are free parameters of the fit function represented by the curve, A is a normalization factor.

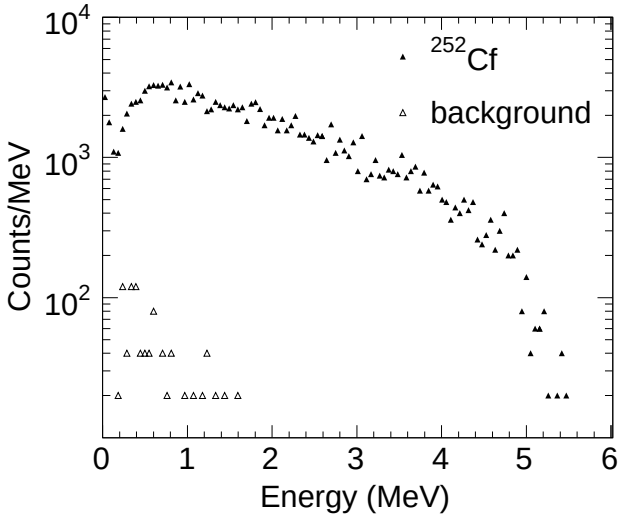

Figure 10: Light output spectrum of tagged neutron events with a capture time acceptance window 1-20 μs.

cident γ-rays in both NaI and neutron detectors. A broad bump between t = 10 ns and 70 ns corresponds to neutrons, as ascertained by test measurements at different TOF distances. The relatively flat region indicated at late TOF times has been used to estimate the magnitude of the random background. Selecting events in the TOF region where neutrons dominate background and prompt γ-rays essentially "tags" events detected by the NSTAR as neutrons.

The capture time distribution measured with the NSTAR for such tagged neutron events relative to the time-zero reference is depicted in Fig. 9. Here, the measured distribution of delayed NSTAR signals is plotted as a histogram against the time relative to the time-zero reference signal. The measured curve has the characteristic shape expected from simulations, with a most probable capture time of $t_{mp} = 7$ μs and a long tail to very long capture times. The solid curve drawn through the data represents a fit employing the function

$$\frac{dN(t)}{dt} = A[\exp^{-\lambda t}[t(\beta - \lambda) - 1] + \exp^{-\beta t}], \quad (1)$$

where α and β are the free parameters [13]. For the NSTAR, the experimental mean capture time was found to be $\langle t_c \rangle = \beta^{-1} + 2\lambda^{-1} = (21.7 \pm 0.2)$ μs, which is close to the value of $\langle t_c \rangle = 20$ μs predicted by DENISE simulation

calculations.

Since the capture time distribution is strongly peaked around t $\approx t_{mp}$ = 7 μs, restricting acceptance of events to a small time interval about the most probable time amplifies the neutron contribution relative to the random background. This behavior is demonstrated by the data from the above ^{252}Cf experiment shown in Fig. 10, where the light output spectrum for tagged neutrons captured within the 20-μs wide acceptance interval is compared to the background distribution. The light output spectrum for the neutron events (solid triangles) shows a Compton continuum reaching up to only $\sim 5 MeV_{ee}$, since the NSTAR is a "thin" detector for high-energy capture γ-rays. As seen in Fig. 10, with a signal-to-background ratio of S/B >(10^2 - 10^3), the background (open triangles) is negligible for most of the range of light output amplitudes characteristic of neutron capture events. Even without the above "gating" requirements on TOF and capture time spectra, neutron induced γ radiation in the range (2.5 - 4.5) MeV$_{ee}$ still dominates the measured light output amplitudes. However, the ungated signal-to-background ratio is only of the order of 2 - 4.

4.3. Efficiency Measurements with a Neutron Generator

The measurements with neutron-γ sources discussed above have demonstrated the functionality of the NSTAR and its capability to detect and identify neutrons, even under unfavorable background conditions. The measurements discussed in the following provide information about the (10cm x 20cm x 50cm) NSTAR neutron detection efficiency and multiplicity resolving power ("multi-hit" capability).

These latter experiments have been carried out with a small neutron generator (ThermoFisher Scientific, Model MP320). The MP320 is a portable generator producing neutrons in D(d,n)^{3}He reaction (DD-neutrons) by accelerating deuterium beam impinging on a deuterated Zr target.

Precise information about the actual spectrum of generator neutrons and their angular distribution was not available and required separate, dedicated calibration measurements. This latter generator calibration measurement was carried out using a neutron monitor detector with well-known response function, consisting of a 5.1-cm by 10.2-cm diameter BC-501A liquid-scintillator cell coupled to an XP2041 Philips photomultiplier. This monitor detector has excellent n-γ pulse shape discrimination capability for neutron energies E$_n$ > 0.5 MeV and was employed together with dedicated analog signal processing electronics (PD6, HMI Elektronik).

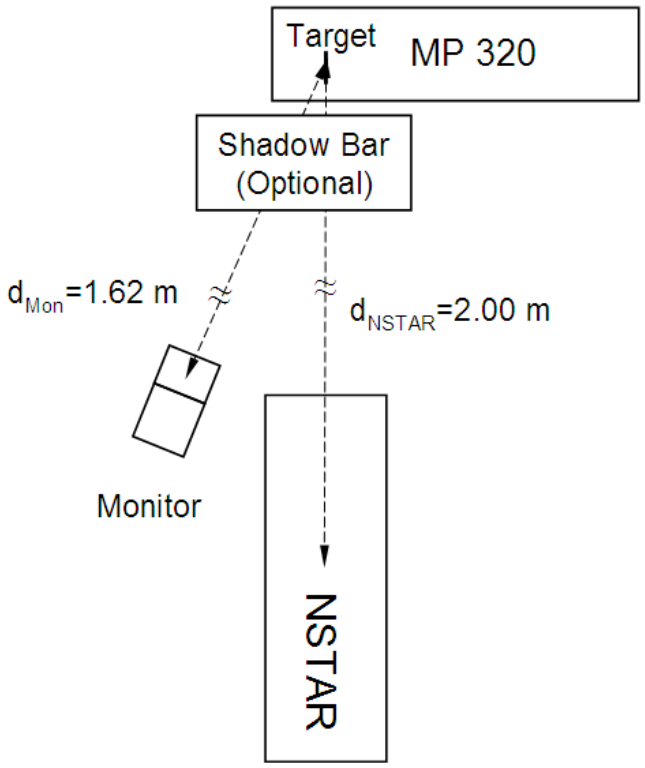

Figure 11: Setup of NSTAR and monitor detectors with the neutron generator ("Geometry 1"). During some of measurements an iron "shadow bar" interdicted the direct view of the target.

Energy dependent light output response and absolute efficiency of the monitor for neutrons were calculated using the program by Cecil [12]. The effective efficiency of the monitor detector to generator neutrons was calculated to be $\varepsilon_{Mon} = 0.34$ at a threshold of $E_{th} = 0.15$ MeV_{ee}. To deduce the actual laboratory energy spectrum of generator neutrons, the light output spectrum measured by the monitor was fitted with an asymmetric Gaussian trial spectrum shape folded with the calculated light output distributions. Results of the measurements indicated noticeable effects of the internal generator structure on the laboratory energy and angular distributions.

The schematics of a typical setup of the 0.5-m long NSTAR and monitor neutron detectors is depicted in Fig. 11, as used in the measurements employing the pulsed-beam neutron generator. Here, the NSTAR is arranged

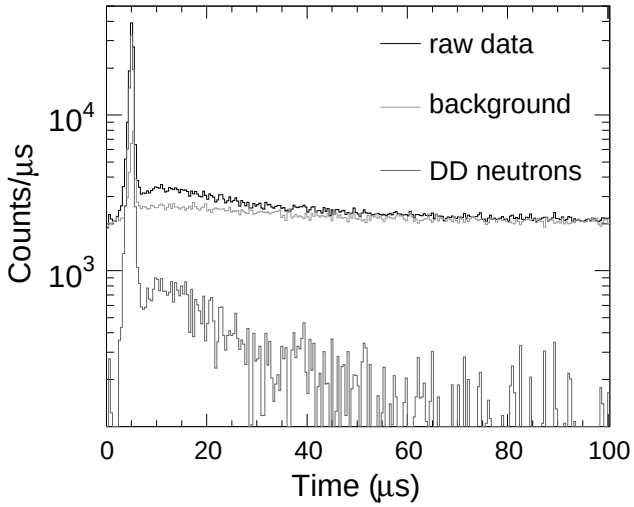

Figure 12: Low-resolution NSTAR time spectrum relative to a generator beam pulse. Full scale corresponds to 100 μs. The background distribution was measured with a shadow bar blocking the direct neutron beam.

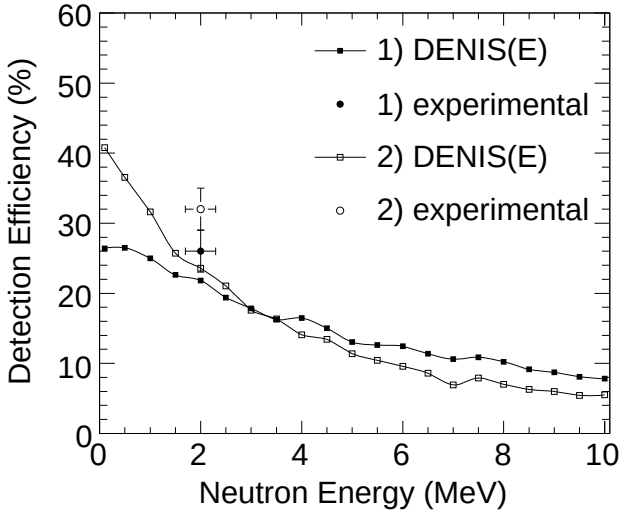

Figure 13: Theoretical and experimental NSTAR neutron detection efficiencies for two NSTAR orientations. Open and solid symbols represent Geometry 1 and 2, respectively. Data points at 2 MeV have beam measured relative to BC-501A neutron monitor detector.

perpendicular to the generator axis facing the generator target with its yz area (cf. Fig. 1) defined as a "Geometry 1". Measurements were also performed using a corresponding arrangement with the NSTAR placed parallel to the generator exposing its xz side to the neutron flux, defined as a "Geometry 2". For the determination of the background of neutrons scattered into the NSTAR, in some of the runs a massive, 60-cm long iron bar was inserted into the direct line of view of the target from both detectors. In addition, the detectors were placed on boron-loaded polyethylene sheet underneath which paraffin blocks and water containers were located to shield the detectors from neutrons backscattered from concrete floor and walls. The measured background contributions were of the order of a few percent of the primary neutron intensity. Measured neutron fluxes were corrected for this background of scattered neutrons.

An example of an NSTAR event time distribution measured relative to generator pulse signals is presented in Fig. 12. For these measurements the generator was tuned to low neutron intensities corresponding to dN/dΩdt $\approx 3.7 \times 10^4$ $\mathrm{sr}^{-1}s^{-1}$. The background spectrum was measured with a shadow bar which is also shown in Fig. 11. As seen from this figure, the net, background-subtracted NSTAR time distribution is dominated by an intense prompt peak in the time range (2 - 7) μs attributed to X rays and γ-rays produced within the generator. At later times events characteristic to neutron capture γ-rays time distribution already familiar from the data shown in Fig. 9 are illustrated. Integrating the net capture time distribution provides the number NSTAR of neutrons detected. Comparing it to the corresponding number of counts, NMon, for the monitor detector, one obtains the NSTAR detection efficiency from the expression

$$\varepsilon = \frac{N_{NSTAR}/\Omega_{NSTAR}}{N_{Mon}/\Omega_{Mon}}\varepsilon_{Mon}, \tag{2}$$

where the quantities Ω_{NSTAR} and Ω_{Mon} denote the solid angles subtended by the two detectors, respectively. In applying the procedure indicated in Eqn. 2, correction due to the anisotropic neutron angular distribution has been accounted for.

The detection efficiencies of the NSTAR detector module determined for the effective generator neutron energy spectrum ($\langle E_n \rangle = (2 \pm 0.3)$ MeV) for an electronic threshold of $\mathrm{E}_{th} = 0.2$ MeV_{ee} in Geometries 1 and 2 are $\varepsilon_1 = (0.26 \pm 0.03)$ and $\varepsilon_2 = (0.32 \pm 0.04)$, respectively. Values for the experimentally determined NSTAR detection efficiency are compared in Fig.

13 with predictions by DENISE simulation calculations carried out for a range of neutron energies up to $E_n = 10$ MeV.

As can be expected, the detection efficiency depends on the orientation of the NSTAR module relative to the incident neutron flux but generally decreases with increasing neutron energy. Experimental efficiencies are in approximate agreement with the predictions which however somewhat tend to underestimate the measurements.

4.4. Neutron Multiplicity Measurements

The NSTAR operational principle for neutron detection and identification relies on the diffusion delayed capture of previously thermalized neutrons by Gd nuclei in the radiator films. The significant statistical spread in capture times can be assessed from the data shown in Figs. 9 and 12. As a consequence of the statistical nature of the diffusion process, the capture events of individual members of an ensemble of multiple neutrons, injected into the NSTAR within a short burst, are dispersed in time. This feature allows one to measure event-by-event the neutron multiplicity of neutron bursts (the number of neutrons in a burst) subject to losses due to the finite detection efficiency and counting dead-time.

To demonstrate the NSTAR neutron multiplicity resolving power ("multi-hit capability") the number of detected neutrons was counted for individual generator pulses as a function of average neutron flux. For these measurements, the NSTAR module was placed as closely as possible and parallel to the generator axis. This geometry largely reduced sensitivity to scattered neutrons and room background. The neutron generator was operated at 10 kHz pulse repetition rate, and instantaneous neutron multiplicities per pulse were varied by a factor of three. Electronic generator signals were used to trigger the NSTAR data acquisition system synchronously with the beam pulses. For each beam pulse, the number of NSTAR responses and their times were recorded individually over an interval of 90 μs with a time resolution of $\Delta t = 100$ ns by a CAMAC counter.

The time distribution of NSTAR responses for trains of four successive neutron generator beam pulses is exhibited in Fig. 14. As is seen in this figure, the pulse produces a prompt NSTAR response due to X rays, γ-rays and neutrons, and at later times a capture time distribution characteristic for the prototype detector. The number of counts in a capture time interval from 7 to 97 μs after the reference time signal represents a "raw" total multiplicity

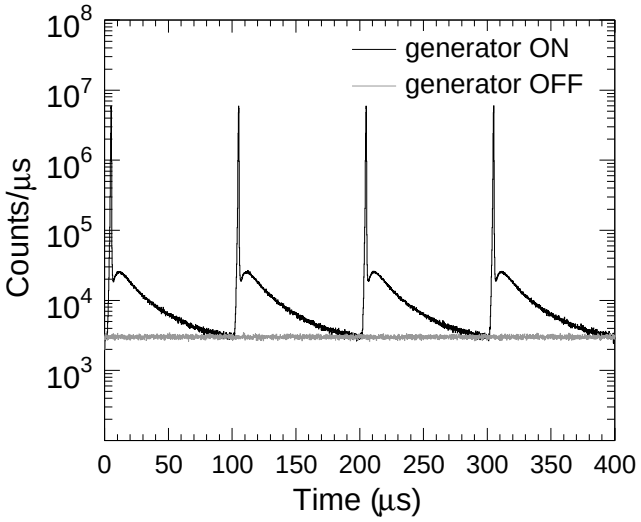

Figure 14: NSTAR time response distribution for a train of four neutron generator beam pulses. The horizontal line represents the measured random background.

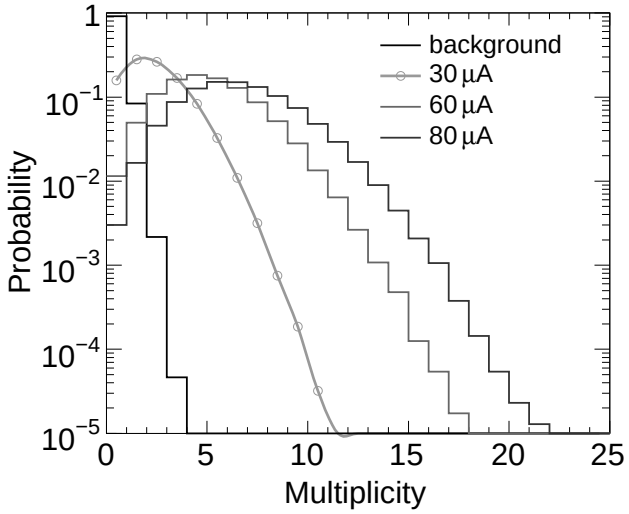

Figure 15: Multiplicity distributions measured with the NSTAR for various generator settings and the room background distribution.

mtot of the event, a sum of background (m_b) and apparent neutron multiplicity (m'). In the following, the associated multiplicity distributions P(m) are characterized by mean and variance, their first and second moments, $\langle m \rangle$ and σ_m^2, respectively. In Fig. 15 experimental multiplicity distributions for three different generator current settings are shown. In addition, the multiplicity distribution of room background events is shown. Here, the probability P is plotted on a logarithmic scale vs. multiplicity. One observes a very narrow, exponentially decreasing background multiplicity distribution and the distributions associated with neutrons from the generator. Both, mean values and variances increase with generator beam current. The variance-to-mean ratios of the multiplicity distributions are consistent with a Poisson process.

In order to derive the true neutron multiplicities m, the first and second moments of the measured total neutron multiplicity distributions have to be corrected for the finite dead-time, background associated with the generator operating at a particular beam current and the NSTAR neutron detection efficiency ε for single neutrons.

Dead-time corrections calculated for the measured pulse pair resolution of 100 ns indicate minor decrease in detector live-times from 99.8 % to 99.3 % for generator beam current increasing from 30 to 80 μA. Background contributions to the total multiplicity distributions at various beam currents were estimated from the intensity of the corresponding capture time distributions at late times (95 - 97) μs. Subtracting the first and second moments of the background distributions from the corresponding moments of the measured total multiplicity distributions already corrected for dead-time, one obtains the moments of the distribution of apparent neutron multiplicities, m'.

Mean values and variances of the true neutron multiplicity distributions are derived from the corresponding measured, apparent quantities according to

$$\langle m \rangle = \langle m' \rangle / \varepsilon, \tag{3}$$

$$\sigma_m^2 / \langle m \rangle = \sigma_{m'}^2 / (\varepsilon \langle m' \rangle) - (1 - \varepsilon)/\varepsilon. \tag{4}$$

Applying the above corrections, the data indicate that the NSTAR detector, subtending a solid angle of $\Omega_{NSTAR} = 5 \times 10^{-3}$ of 4π, was exposed to an average flux of $\langle m_{30} \rangle = (3.4 \pm 0.46)$, $\langle m_{60} \rangle = (9.5 \pm 1.21)$ and $\langle m_{80} \rangle = (13.69 \pm 1.70)$ neutrons per burst at beam currents of 30, 60 and 80 μA, respectively. The corresponding variance to mean ratios derived for the

measured moments of the true distributions of neutrons per burst increase from $R_{30} = \sigma_m^2/\langle m \rangle = (1.3 \pm 0.7)$, $R_{60} = \sigma_m^2/\langle m \rangle = (1.3 \pm 0.7)$, to $R_{80} = \sigma_m^2/\langle m \rangle = (1.6 \pm 0.7)$, which is consistent with a Poisson process. Therefore, the widths of the apparent multiplicity distributions are significantly influenced by the statistical uncertainties associated with the NSTAR counting process.

The above mean neutron rates measured with the NSTAR correspond to total rates ranging from 80 to 300 neutrons emitted by the generator per burst. These results agree with other independent rate measurements, including vendor provided specifications. The high live-time values mentioned previously suggest that the NSTAR detector can be operated without significant losses at mean rates up to $\langle \dot{N} \rangle \approx 7 \times 10^{-4} s^{-1}$. However, the multi-hit capability of the NSTAR provides data containing additional information on the emission process, which is utilized in basic science applications to characterize nuclear reactions. In the present application, moment ratios of the multiplicity distributions (cf. Eqns. 3 and 4) consistent with a Poisson process are expected for stable generator operations.

5. Conclusions

Prototype modules of NSTAR, a new type of ^{nat}Gd loaded, capture gated plastic-scintillator neutron detector have been designed, built and tested successfully with radioactive sources and neutrons from a pulsed-beam neutron generator. The detector is economical, made of environmentally friendly components, is scalable and has high neutron efficiency at a low energy threshold for neutrons. A simulation computer code (DENISE) is able to model quantitatively the actual NSTAR performance.

Similar to other fast scintillator detectors, the NSTAR can be utilized in time-of-flight and correlation experiments. Good position sensitivity has been obtained in measurements of differences in times of arrival light output signals at opposite detector ends.

The NSTAR neutron-γ discrimination method is most effective in applications where either a prompt light output signal is generated within the scintillator or where an external reference is available, such as in measurements with pulsed or tagged beams. In the absence of such reference signals, neutron identification is still possible, based on the high energies of Gd capture γ-rays, albeit at reduced efficiency. Measurements with intense neutron beams have demonstrated the "multi-hit" capability of NSTAR prototypes

and its capability to measure event by event multiplicities of neutrons injected in short bursts. Although the NSTAR concept has been proven in a particular realization, obvious extensions and modifications have potential in scientific and technical applications.

6. Acknowledgments

The authors would like to thank David Vieira for lending ^{3}He proportional counters. This work has been supported by U.S. Department of Energy Grant No. DE-FG02-88ER40414.

References

[1] G. Knoll, Radiation Detection and Measurements, third ed., Wiley, New York, 1999.

[2] U. Jahnke, G. Ingold, H. Homeyer, M. Brgel, Ch. E Egelhaaf, H. Fuchs, and D. Hilscher, Phys. Rev. Lett. 50, (1983) 1246.

[3] U. Jahnke, G. Ingold, D. Hilscher, M. Lehmann, E. Schwinn, and P. Zank, Phys. Rev. Lett.57, (1986) 190.

[4] http://nuchem.chem.rochester.edu/OnlineReports/SuperBall/SB-pp1-50.pdf, September 2010.

[5] B. Djerroud, at al., Phys. Rev. C, 64, (2001) 34603.

[6] Z. W. Bell, M.A. Miller, L. Maya, G.M. Brown, F.V. Sloop, Jr., IEEE Transact. Nucl. Sci. 51, (2004) 1773.

[7] L. Ovechkina, K. Riley,S. Miller, Z. Bell, V. Nagarkar, Physics Procedia, 2, (2009) 161.

[8] J. Poitou, C. Signarbieux, Nucl. Inst. Meth, 114, (1974) 113.

[9] Y. Perier at al., Nucl. Instr. Meth. A 413, (1998) 312.

[10] http://www3.dowcorning.com/DataFiles/090007b28117a63f.pdf, September 2010.

[11] http://www.detectors.saint-gobain.com/uploadedFiles/SGdetectors/Documents/Product_Data_Sheets/BC400-404-408-412-416-Data-Sheet.pdf, September 2010.

[12] R. A. Cecil et. al., Nucl. Instr. Meth. 161, (1979) 439.

[13] K. Banerjee at al., Nucl. Instr. Meth. A 580, (2007) 1383.

Inertial Fission of Rotating Projectile-like Fragments in Ca+Sn Reactions at E = 45 AMeV

M.J. Quinlan,[1] J. Tõke,[1] I. Pawełczak,[1] H. Singh,[1] W.U. Schröder,[1] F. Amorini,[2] A. Anzalone,[2] L. Auditore,[3] G. Cardella,[4] S. Cavallaro,[5] M.B. Chatterjee,[6] E. De Filippo,[4] E. Geraci,[5] A. Grzeszczuk,[7] P. Guazzoni,[8] E. La Guidara,[9] G. Lanzalone,[10] S. Lo Nigro,[5] D. Loria,[3] C. Maiolino,[2] A. Pagano,[4] M. Papa,[4] S. Pirrone,[4] G. Politi,[5] F. Porto,[11] F. Rizzo,[11] P. Russotto,[11] A. Trifiró,[3] M. Trimarchí,[3] G. Verde,[4] M. Vigilante,[12] and L. Zetta[8]

[1]*Departments of Chemistry and Physics University of Rochester, Rochester NY*
[2]*INFN Laboratori Nazionali del Sud, Catania, Italy*
[3]*INFN gruppo coll. Di Messina & Dipartimento di Fisica Universitá di Messina*
[4]*INFN Sezione di Catania*
[5]*INFN Sezione di Catania & Dipartimento di Fisica e Astronomia Universitıa di Catania*
[6]*Saha Institute for Nuclear Physics, Kolkata, India*
[7]*Institut of Physics, University of Silesia, Katowice, Poland*
[8]*INFN Sezione di Milano & Dipartimento di Fisica Universitá di Milano*
[9]*INFN Sezione di Catania & CSFNSM, Catania, Italy*
[10]*INFN Laboratori Nazionali del Sud, Catania, Italy & Universitá KORE Enna, Italy*
[11]*INFN Laboratori Nazionali del Sud, Catania, Italy & Dipartimento di Fisica e Astronomia Universitıa di Catania*
[12]*INFN Sezione di Napoli & Dipartimento di Fisica Universitá Federico II di Napoli*

A class of events representing binary fragmentation of calcium-like primary reaction products from Ca+Sn reactions at 45 AMeV has been identified based on characteristic kinematical correlations between the reaction products. The subsequent analysis has shown that the fragmenting projectile-like complex rotates with a sense of rotation consistent with its negative scattering angle. The break-up is seen to be dynamical and fast, caused largely by inertial collective motion arising from the lack of velocity equilibration within this complex. The inertial collective motion is manifested through relative fragment velocities significantly higher than those expected from Coulomb driven decay. The lifetime of the complex is inferred from the reconstructed rotation angle and found to be comparable to the thermal relaxation time of nuclear matter.

PACS numbers: 25.70.Pq,25.70.Mn

Over the last quarter century, systematic studies of heavy-ion reactions at low and intermediate bombarding energies (E < 100 AMeV) have lead to the conclusion that the experimental observations are to a large extent consistent with a two-step reaction scenario[1]. The first step involves a dynamical projectile-target interaction that produces two excited "primary" products, which subsequently undergo quasi-statistical decay in a second step. The dynamical interaction stage is usually depicted as a dissipative collision wherein the projectile nucleus scatters (orbits) off-of (partially around) the target. The interaction is modeled using either classical trajectory and transport models[2, 3] or more detailed models such as, e.g., BUU[4] or QMD[5]. The second, quasi-statistical decay stage, is modeled with statistical equilibrium codes such as, e.g., PACE[6] and GEMINI[7] using the predictions of the first step as input parameters.

In a refinement to the above two-step scenario, one routinely observes "non-equilibrium" emission of particles in the collision stage, including the intriguing emission of intermediate-mass fragments (IMF) with atomic numbers $3 \leq Z \leq 10$. The latter has been ascribed to the disintegration of the temporary interface domain bridging the interacting projectile and target[8–10]. This process is occasionally dubbed "neck emission" or "multiple neck rupture". Recently reported evidence complementing the above scheme of events suggests that the massive primary projectile-like (PLF) and target-like (TLF) fragments, after leaving the interaction site, may still undergo binary division before reaching equilibrium and contributing significantly to IMF production. This process is occasionally dubbed "dynamical fission" because the division has been reported to occur on time scales so short as to indicate a dynamical process[11–14].

The present work focuses on the phenomenology of such a post-interaction, non-equilibrium fragmentation (fission) of projectile-like fragments from Ca+Sn reactions at E=45 AMeV. The properties and kinematic correlations of the dynamically formed fission fragments are analyzed within a novel framework. The correlations between fission fragments are found to retain a memory of the short lived PLF, which undergoes a fast binary division arising from an internal velocity gradient acquired when the neck ruptures first near the target. While this PLF is highly unstable to binary "inertial" fission it lives long enough to rotate, which facilitates a unique study of the reaction mechanism. The limited aim of the present work considers the orientation of the angular momentum of the PLF and in turn the sign of the scattering angle (Θ). The sign is not directly observable experimentally, but it has been indirectly assessed through studies of the polarization of gamma- (and the anisotropy of

beta-) rays emitted from excited nuclei formed in other damped reactions[15–17].

The experiment was performed at the Laboratori Nazionali del Sud (LNS) in Catania, Italy, using the advanced detector array CHIMERA[18]. In the experiment, a beam of 45 AMeV ^{48}Ca ions from the superconducting K800 cyclotron was focused on a self supporting 689-μg/cm^2 ^{124}Sn target placed at the operational center of the CHIMERA array. It is the 4π geometry of the array's 1192 detector telescopes, the resulting high granularity at forward angles, the high atomic number resolution $\Delta Z = 1$ for charged particles ($1 \leq Z \leq 21$), and the reasonably good time resolution (TOF) that allow one to obtain a robust characterization of reaction events in terms of product multiplicities, identities, energies, and emission angles. These characteristics also make the CHIMERA array uniquely suited for studies of kinematical correlations between multiple fragments in general, and of PLF fragmentation in particular.

The rationale behind the present analysis scheme can be understood in terms of classical dynamics. Figure 1 depicts two possible PLF trajectories, both leading to the same experimental scattering angle. Physically, however, these trajectories differ in the sign of their scattering angle and, importantly, also in the orientations of both the angular momentum of the system as a whole and that of the PLF and TLF individually. The latter are understood to acquire their spins (with an associated sense of rotation indicated by the arrows at points R_+ and R_-) through stochastic nucleon exchange[19]. The angular momentum of the PLF in either case will be aligned perpendicular to the reaction plane. Therefore, if the PLF is subsequently to undergo fission, it will do so dominantly in the plane. If additionally the fission is to be dynamical, and result from the disintegration of the neck connecting the PLF and TLF as they separate, then the angular distribution of the fission fragments in the PLF rest frame is expected to be anisotropic and peaked in the direction of the PLF-TLF separation axis. Because the PLF rotates with a nearly constant angular velocity, the fragmentation probability expressed in terms of the fission fragment angular distribution $\left(\frac{d\sigma}{d\alpha}\right)$ is related to the lifetime of the PLF, where the orientation of the fission axis (α) is taken as a measure of time.

Dynamical fission of a PLF could be driven by either (i) the initial geometry of the unstable nucleus being at or past the fragmentation saddle, or (ii) an under-damped collective motion towards the saddle, or (iii) both (i) and (ii) playing some non-negligible role. In case (ii) the under-damped collective motion could naturally arise from a mismatch in average velocities of the "bulk" PLF matter and the substantive residue of the non-adiabatic interaction-domain matter or neck. In Fig. 1, the neck residue is indicated schematically as a shaded area. If inertial motion, arising from such a velocity mismatch, dominates the fission dynamics, then it might leave a clear experimental signature in the form of an excess relative velocity of between PLF fission fragments (compared to what is expected from Coulomb driven decay).

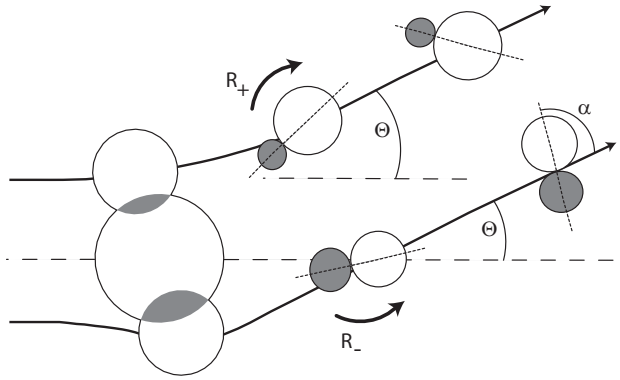

FIG. 1: Schematic depiction of positive (top) and negative (bottom) PLF scattering angles and their associated sense of rotation (R_+ and R_-) within the inertial fission scenario.

Consistent with its limited aim, the present study focuses on a relatively small subset of all events, namely on those which bear the kinematical signatures of binary inertial fission of the PLF. Specifically, the study focuses on events with PLF scattering angles larger than the grazing angle, which in the given scenario are understood to correspond to partial orbiting trajectories, significant projectile-target overlaps, and counter-clockwise senses of rotation. This is important because large laboratory scattering angles provide an experimental link with a singular sense of rotation of the PLF.

The kinematics of the presumed binary PLF fission events were reconstructed based on the measured velocity vectors of two detected fission fragments. A distinction is made between the heavier (index H) and lighter (index L) fragments to define the orientation of the PLF fission axis. An event was presumed to be a PLF fission event when two fragments (the presumed fission fragments) with atomic numbers $Z \geq 3$ were detected in a forward cone of the CHIMERA array here defined as an opening angle of 36^o, i.e. $|\Theta_H|$ and $|\Theta_L| < 18^o$. Subsequent analysis has shown that the majority of the initial charge of the projectile is contained in the two fission fragments and the light charged particles detected within this opening angle. In the reconstruction, mass numbers of the heavier A_H and lighter A_L fission fragments were determined based on their measured atomic numbers Z_H and Z_L respectively, and the evaporation "attractor line" [20]. It was also assumed that the measured secondary or post-evaporation velocities coincide with the primary ones. The velocity vector $\bar{\mathbf{v}}_{\rm PLF}$ of the PLF and the relative velocity vector $\bar{\mathbf{v}}_{\rm Rel}$ of the fragments were then calculated from the measured velocity vectors $\bar{\mathbf{v}}_{\rm H}$ and $\bar{\mathbf{v}}_{\rm L}$ of the two fragments as

$$\bar{\mathbf{v}}_{\rm PLF} = \frac{{\rm A_H}\bar{\mathbf{v}}_{\rm H} + {\rm A_L}\bar{\mathbf{v}}_{\rm L}}{{\rm A_H} + {\rm A_L}} \quad \text{and} \tag{1}$$

$$\bar{\mathbf{v}}_{\rm Rel} = \bar{\mathbf{v}}_{\rm H} - \bar{\mathbf{v}}_{\rm L}. \tag{2}$$

Subsequently, the reaction plane was determined using the beam and PLF velocity vectors, $\bar{\mathbf{v}}_{\rm Beam}$ and $\bar{\mathbf{v}}_{\rm PLF}$, respectively. The unit vector normal to the plane $\hat{\mathbf{n}}_{\rm Plane}$ is defined via,

$$\hat{\mathbf{n}}_{\rm Plane} = \frac{[\bar{\mathbf{v}}_{\rm Beam} \times \bar{\mathbf{v}}_{\rm PLF}]}{|[\bar{\mathbf{v}}_{\rm Beam} \times \bar{\mathbf{v}}_{\rm PLF}]|}. \tag{3}$$

Furthermore, the unit vector $\hat{\mathbf{a}}_{\rm Rel}$ of the projection of the fragment relative velocity vector $\bar{\mathbf{v}}_{\rm Rel}$ onto the reaction plane was calculated as

$$\hat{\mathbf{a}}_{\rm Rel} = \frac{[[\hat{\mathbf{n}}_{\rm Plane} \times \bar{\mathbf{v}}_{\rm Rel}] \times \hat{\mathbf{n}}_{\rm Plane}]}{|[[\hat{\mathbf{n}}_{\rm Plane} \times \bar{\mathbf{v}}_{\rm Rel}] \times \hat{\mathbf{n}}_{\rm Plane}]|}. \tag{4}$$

The in-plane orientation angle α of the PLF fission axis with respect to the unit PLF velocity vector $\hat{\mathbf{v}}_{\rm PLF}$ was then inferred from its computed $cos(\alpha)$ and $sin(\alpha)$ values

$$cos(\alpha) = (\hat{\mathbf{a}}_{\rm Rel} \bullet \hat{\mathbf{v}}_{\rm PLF}) \quad \text{and} \tag{5}$$

$$sin(\alpha) = (\hat{\mathbf{n}}_{\rm Plane} \bullet [\hat{\mathbf{v}}_{\rm PLF} \times \hat{\mathbf{a}}_{\rm Rel}]). \tag{6}$$

The periodic angle α customarily spans the range $[-180^o, 180^o]$. However to facilitate the interpretation of the data, $+360^o$ was added to angles of $\alpha < 80^o$ (see Fig. 2). The (*tilting*) angle Θ_{Tilt} between the reaction plane and the fission axis was calculated via

$$cos(\Theta_{Tilt}) = \frac{(\hat{\mathbf{a}}_{\rm Rel} \bullet \bar{\mathbf{v}}_{\rm Rel})}{|\bar{\mathbf{v}}_{\rm Rel}|}. \tag{7}$$

In the subsequent analysis, events were selected subject to a coplanarity condition of $cos(\Theta_{Tilt}) > 0.8$. In some cases additional conditions were set on the reconstructed PLF deflection angle Θ_{PLF} and on the PLF fragment mass asymmetry η defined via

$$\Theta_{PLF} = acos\left(\frac{\bar{\mathbf{v}}_{\rm PLF} \bullet \bar{\mathbf{v}}_{\rm Beam}}{|\bar{\mathbf{v}}_{\rm PLF}||\bar{\mathbf{v}}_{\rm Beam}|}\right) \tag{8}$$

$$\eta = \frac{A_H - A_L}{A_H + A_L} \tag{9}$$

The results of the present analysis are shown Fig. 2. The inclusive distribution of the in-plane orientation angles α subject to only the coplanarity condition is presented in Fig. 2(a) as a solid line. The experimental

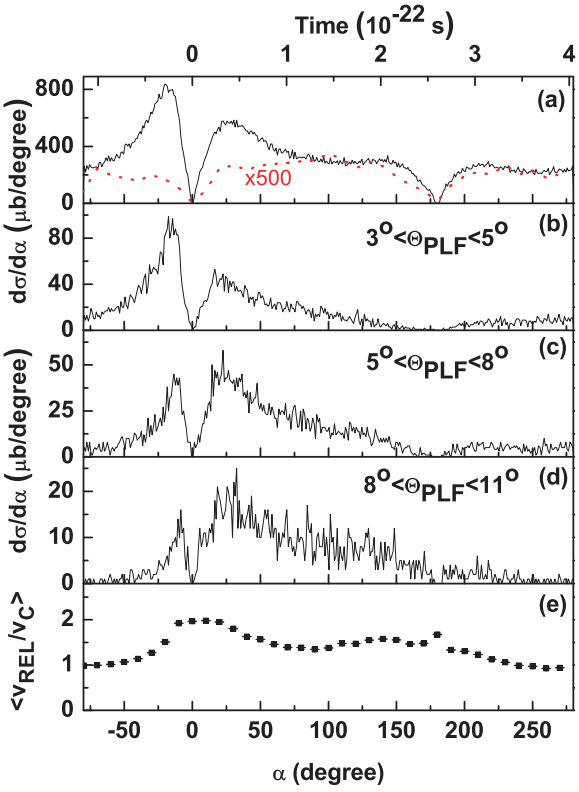

FIG. 2: (a) In-plane angular distributions of PLF fission fragments subject to the coplanarity condition (solid line). For comparison, also shown is the angular distribution assuming an isotropic (statistical) distribution which has been corrected for experimental, geometrical and electronic acceptances (dashed line). (b)-(d) Conditional in-plane angular distributions (see text). (e) Average fission fragment relative velocity divided by that expected for Coulomb fragmentation versus the in-plane angle. The data are sorted using the conditions $\Theta_{PLF} > 5^o$, $\eta > 0.5$, and the coplanarity condition. The upper abscissa denotes the estimated rotational timescale.

distribution is peaked at small angles in contrast to predictions of a "two-step" (dashed line) adiabatic binary reaction model[2, 7]. However, the marked depressions observed around $\alpha = 0^o$ and $\alpha = 180^o$ are approximated by this model, which also includes a realistic account of the limited geometric and electronic acceptances of the CHIMERA array. From the ordering of vectors in the various cross-products presented in Eqs. 3-6, an in-plane angle of $\alpha = 0^o$ corresponds to a situation where the heavier fragment moves in the direction of the PLF, while increasing values correspond to a counter-clockwise rotation. The distinctly asymmetric distribution in Fig. 2(a) can therefore be interpreted in terms of a predominantly counter-clockwise sense of rotation of the PLF in the selected events.

The distributions presented in Figs. 2(b)-(d) result from the selection of events with reconstructed PLF de-

flection angles noted in the labels, mass asymmetries $\eta > 0.5$, and the previously mentioned coplanarity condition. The selection of asymmetric fission events removes those events in which the direction of the relative velocity vector $\bar{\mathbf{v}}_{\rm Rel}$ is poorly defined due to small differences in the observed fragments' atomic number. The resulting distributions differ from the "inclusive" selection mainly in a reduction of the component consistent with isotropic "statistical" fission and a relative increase in the contribution of counter-clockwise rotating PLFs. The latter effect is consistent with the "exclusive" selection of orbiting trajectories (R_- in Fig. 1), given that the grazing angle for the studied reaction is $\Theta_{Grazing} \approx 3^o$. The shift towards longer lifetimes most noticeable in the comparison of panels (c) and (d) could result from a difference in spin of the selected PLFs, the mechanics of the PLF fragmentation (to be addressed below), or some combination of the two.

The mechanics of the PLF fragmentation can be understood from Fig.2(e) illustrating the PLF fission fragment relative velocities as a function of the rotation angle α. As seen in this figure, for small rotation angles consistent with fragmentation before significant rotation of the exotic PLF complex, this velocity is significantly higher than that expected from a Coulomb driven split of an equilibrated PLF. The relative velocity expected from Coulomb driven fission (V_c) has been approximated assuming a touching spheres scission configuration of the two reaction products. Such an excess velocity can be explained only by assuming that the nucleon velocities within the nascent PLF were not fully equilibrated and that the lighter fragment retained a memory of the neck joining the projectile and target nuclei. Importantly, Fig. 2(e) also illustrates that, as the PLF rotates away from its original orientation, it fragments with generally decreasing relative fragment velocity. Plausibly, the velocity field within the PLF equilibrates with time (measured by the angle α), leaving less and less macroscopic relative velocity between the fragment-candidates. Eventually, the excess velocity drops below the value needed to effect fragmentation in a time comparable to the rotational period of the PLF. This is seen to occur around rotation angles of $\alpha \approx 200^o$ in Fig. 2(d). The rotational period of a ^{48}Ca nucleus with an angular momentum consistent with predictions of the nucleon exchange model[21] has been estimated. This timescale is shown along the upper axis of Fig. 2. The estimated value is comparable to the "thermal" equilibration time of nuclear matter which tentatively supports the conclusion that increased equilibration (with increasing rotation angle) of the PLF leads to the observed decrease in fragmentation probability.

In summary, fast dynamical fission of relatively light projectile-like fragments was observed in a class of events from the Ca+Sn reaction at E/A = 45MeV. The in-plane angular distributions of fission fragments reveal that the PLF rotates with a sense of rotation expected for negative-angle dissipative orbiting. The trends in the observed relative velocities of the PLF fission fragments suggest that inertial collective motion resulting from an imbalance of the velocity field within the nascent PLF is responsible for the fission. The imbalance results from the mismatch between the velocity of the residue of the non-adiabatic interface domain and the average velocity of the remaining PLF matter. As this velocity field relaxes, the imbalance decreases and eventually reaches a point where it no longer can effect a fast "inertial" fission. The above imaging of a very fast fragmentation process is made possible by the availability of a sufficiently fast experimental clock - the rotation of the PLF.

The authors wish to acknowledge inspiring discussions with Dr. Romualdo DeSouza. This work was supported by the US Department of Energy Grant No. DE-FG02-88ER40414.

[1] W. U. Schröder and J. R. Huizenga, *Treatise on Heavy-Ion Science*, vol. 2 (Plenum, New York, 1984).
[2] W. U. Schröder et al., Nucl. Sci. Res. Conf. Ser. **11**, 255 (1987).
[3] H. Feldmeier, Prog. Phys. **50**, 915 (1987).
[4] W. Bauer, Phys. Rev. Lett. **61**, 2534 (1988).
[5] J. Aichelin et al., Phys. Rev. C **37**, 2451 (1988).
[6] A. Gavron, Phys. Rev. C **21**, 230 (1980).
[7] R. Charity, URL `www.chemistry.wustl.edu/~rc/`.
[8] C. P. Montoya et al., Phys. Rev. Lett. **73**, 3070 (1994).
[9] B. Lott et al. (World Scientific, Singapore, 1993), p. 195.
[10] J. Tõke et al., Phys. Rev. Lett. **75**, 2920 (1995).
[11] P. Glässel et al., Phys. Rev. Lett. **48**, 1089 (1982).
[12] S. Hudan et al., Phys. Rev. C **71**, 054604 (2005).
[13] E. De Filippo et al., Phys. Rev. C **71**, 044602 (2005).
[14] E. De Filippo et al., Phys. Rev. C **71**, 064604 (2005).
[15] K. Sugimoto et al., Phys. Rev. Lett. **39**, 323 (1977).
[16] W. Trautmann et al., Phys. Rev. Lett. **46**, 1188 (1981).
[17] R. C. Lemmon et al., Phys. Lett. **B446**, 197 (1999).
[18] A. Pagano et al., Nucl. Phys. **A681**, 331 (2001).
[19] R. Vandenbosch, Phys. Rev. C **20**, 171 (1979).
[20] R. J. Charity, Phys. Rev. C **58**, 1073 (1998).
[21] J. Randrup, Nucl. Phys. **A307**, 319 (1978), ibid., **A327** (1979) 490: ibid., **A383** (1982) 468.

Isoscaling as a probe of density dependence of the symmetry energy in the harmonic-interaction Fermi gas model

W. Ye,[1,2] J. Tõke,[1] and W. U. Schröder[1]

[1]*Department of Chemistry and Physics,*
University of Rochester, Rochester, New York 14627, USA
[2]*Department of Physics, Southeast University,*
Nanjing 210096, People's Republic of China

Abstract

Using a harmonic-interaction Fermi gas model (HIFG) that accounts for the nuclear expansion, we study isoscaling as a measure of the density dependence of the symmetry energy. The parameterized form of the density dependence obtained is $E_{sym}(\rho) \approx 31.0(\rho/\rho_0)^{0.73}$, which is in quantitative agreement with many very recent results derived through the comparison between theoretical simulations and experimental observables. The HIFG model is thus a useful tool to explore the behavior of the symmetry energy at subsaturation density.

PACS numbers: 25.70.Pq, 24.10.Pa, 21.65.+f, 21.60.Ev

I. INTRODUCTION

Isospin dependent nuclear reaction and decay phenomena have attracted considerable interest in recent years since they provide experimental access to the neutron-proton asymmetry term of the effective nuclear equation of state (EOS) [1, 2]. This term, the nuclear "symmetry energy," has a quantal origin in the Pauli Exclusion Principle for nucleons. At reduced nucleonic phase space densities, where the Exclusion Principle loses effectiveness, the symmetry energy is expected to diminish also. Conversely, the symmetry term should become large for high phase space densities. To deduce or constrain the symmetry energy, specifically its dependencies on excitation energy and matter density, is important for understanding heavy ion reactions [1–4], the structure of nuclei far off stability [5] and for many interesting astrophysical problems [6].

In principle, it is not feasible to measure separately the above dependencies of the symmetry energy on excitation energy and matter density. The difficulty arises from the fact that the effect is a superposition of influences associated with the nucleonic momentum and the configuration space densities. Fortunately, at excitation energies of interest the effective contributions of the two components have very different strengths. While nuclei remain essentially degenerate Fermi gases even at nuclear temperatures of the order of the binding energy per nucleon, the nuclear volume expansion associated with high excitations is expected to lead to highly diluted spatial matter densities. Therefore, the latter density effect should have a more noticeable influence on the symmetry energy than that associated with a thermal softening of the surface of the Fermi momentum sphere. This has also been suggested elsewhere [7, 8]. Supporting evidence for such an excitation energy dependence has been reported based on experimental observations [9–11]. Even so, the symmetry term remains a key unknown in the effective nuclear EOS, except for the normal saturation density of cold nuclei close to the β stable valley.

To provide a level of confidence in any extrapolation of the symmetry energy term to interesting, but not directly accessible nuclear matter densities, experimental data are needed both for sub-normal and supra-normal matter densities. To some extent these density domains can be studied in heavy-ion collisions at intermediate and relativistic bombarding energies, respectively. However, to derive information about the symmetry energy for mat-

ter densities much higher than normal is complicated significantly by hadronic degrees of freedom appearing at bombarding energies above the effective pion threshold of $E/A \approx 50MeV$. In contrast, the low-density domain accessible in intermediate-energy nuclear reactions is not afflicted by directly interfering extra-nucleonic degrees of freedom.

These latter reactions can lead to highly excited compound-like nuclei which undergo significant spatial expansion prior to their subsequent decay [12–15]. Unfortunately, the identities of the primary reaction products are often difficult to ascertain with high precision and their decay patterns can be quite complex. However, by comparing isotopic particle yields measured for compound nuclei produced in different reactions with very different overall neutron/proton ratios ("isoscaling"), an interpretation of the decay patterns in terms of the symmetry energy may remain possible [16]. These opportunities to explore the nuclear symmetry energy have already led to a flurry of new experimental [9–11, 16–18] and theoretical [16, 19–28] activities. On the other hand, it is not obvious how to separate equilibrium nuclear symmetry properties from the isospin dependent dynamics of non-equilibrium nuclear transport studied in recent work [17, 29, 30] with similar goals.

In view of its importance for structure and reaction studies at the new rare-ion accelerator facilities, the question as to what extent and how the associated changes in symmetry energy are reflected in characteristic nuclear transmutation and decay patterns [1, 2] deserves a more definitive answer than available to date. The aim of the present paper is to illustrate the relation between experimental observables and the nuclear symmetry energy expected from the decay of highly excited compound systems at subnormal matter densities. The following Sec. II of this paper describes these hot, expanded nuclei in terms of a realistic interacting Fermi gas model in harmonic approximation (HIFG). The highly successful model [13–15] represents a natural extension of the traditional compound nucleus picture. Numerical results predicted for the isoscaling properties of particle yields from sample nuclear systems are presented in Sec. III, followed by a summary and conclusions in Sec. IV.

II. THEORETICAL FORMULISM

The present study assumes that an excited nuclear system expands in a self-similar fashion so as to reach a state of approximate thermodynamic equilibrium, where the entropy S is

maximal for the given total excitation energy E^*_{tot}, i.e.,

$$\frac{\partial S(E^*_{tot},\rho)}{\partial \rho} \mid_{E^*_{tot}} = 0. \tag{1}$$

The functional dependence of the entropy on E^*_{tot} and bulk nuclear matter density ρ is evaluated using the Fermi-gas model relationship

$$S = 2\sqrt{aE^*_{th}} = 2\sqrt{a(E^*_{tot} - E_{compr})}, \tag{2}$$

where a is the level density parameter, E^*_{th} is the thermal excitation energy, and E_{compr} is the collective compressional energy. It has been pointed out [14] that the presence of a surface contribution to the level density parameter is of crucial importance as it describes that part S_S of the entropy S of the system, which is associated with the diffuse surface domain. One has

$$S = S_V + S_S, \tag{3}$$

where S_V is the entropy of the bulk matter. Because of this reason, the level density parameter a_0 at ground-state matter density ρ_0 includes volume and surface terms [31]

$$a_0 = a_V + a_S = \alpha_V A + \alpha_S A^{2/3} F_2, \tag{4}$$

where A is the atomic number, F_2 is the surface area relative to a spherical shape. The dependence of the level density parameter on the nuclear matter density for finite nuclear matter is given by the Fermi-gas model:

$$a(\rho) = a_0 (\frac{\rho}{\rho_0})^{-2/3}, \tag{5}$$

The term "self-similar expansion" is used here to describe a type of expansion in which any change in the matter density profile is reducible to a simple rescaling of the radial coordinate, such that

$$f_\rho(r) = c^3 f_0(cr), \tag{6}$$

where $f_0(r)$ is the ground-state density profile function and c is a scaling constant.

The compressional energy in Eq. (2) is approximately in the present study following prescription proposed in the expanding emitting model [12], i.e.,

$$E_{compr} = E_b (1 - \frac{\rho}{\rho_0})^2, \tag{7}$$

where E_{compr} and E_b are the compressional and the ground-state binding energies, respectively.

Equations (1)−(3) and (7) allow one to obtain an analytical expression for the equilibrium density ρ_{eq}/ρ_0 of nuclear matter as a function of the excitation energy:

$$\frac{\rho_{eq}}{\rho_0} = \frac{1}{4}(1 + \sqrt{9 - 8\frac{E^*_{tot}}{E_b}}). \tag{8}$$

It has been shown [14] that the curve ρ_{eq}/ρ_0 obtained from the single-parameter function in Eq.(8) essentially coincides with a similar curve from finite-temperature Hartree-Fock calculation, as reported in [32].

The probability p of emitting a fragment from an equilibrated compound nucleus (CN) is evaluated using the Weisskopf formalism [33]:

$$p \propto e^{\Delta S} = e^{S_{saddle} - S_{eq}}, \tag{9}$$

where S_{eq} and S_{saddle} are the entropies for the equilibrated CN and the saddle-point configuration of touching, respectively. Within the Fermi gas model, the entropy for the two configurations can be calculated as

$$S_{eq} = 2\sqrt{a_A[E^*_{tot} - E_b(1 - \frac{\rho_{eq}}{\rho_0})^2]}, \tag{10}$$

and

$$S_{saddle} = S_{res} + S_{frag} = 2\sqrt{(a_{res} + a_{frag})E^{*th}_{saddle}}. \tag{11}$$

In Eqs. (10) and (11), a_A, a_{res} and a_{frag} are the level density parameters of the CN system at equilibrium, of the residue, and of the fragment, respectively. E^{*th}_{saddle} in Eq.(11) is the thermal excitation energy of the system in the saddle-point configuration. The latter quantity is calculated as

$$E^{*th}_{saddle} = E^*_{tot} - E_b(1 - \frac{\rho_{eq}}{\rho_0})^2 - V_{saddle}, \tag{12}$$

where V_{saddle} is the collective saddle-point energy.

In the statistical model of nuclear decay, the decay widths can be expressed as

$$\Gamma(E^*) \propto exp\{-Q/T\} \propto exp\{S\}, \tag{13}$$

where T is nuclear temperature of the CN from the excitation energy prior to its decay. S is entropy. Since the Q value for a decay is determined by the difference in binding energies

$B(N,Z)$ of parent and daughter nuclei, the Q value can be expressed as

$$-Q(N,Z) \approx (\frac{\partial B}{\partial N})_{CN} \cdot [N - N_{CN}] + (\frac{\partial B}{\partial Z})_{CN} \cdot [Z - Z_{CN}] \approx Q_0 + \alpha \cdot N + \beta \cdot Z. \quad (14)$$

For a CN decay via evaporation of simple light particles with no internal structure the Q value depends mainly on the difference between the neutron and proton numbers of daughter and parent nucleus, i.e., those ($(N,Z)_P$) of the emitted particle P. In this fashion, one expects yields of different isotopes, i and j, emitted from the same CN to scale approximately like

$$\frac{\Gamma_i(E^*)}{\Gamma_j(E^*)} \propto exp\{\frac{Q_j - Q_i}{T}\} \propto exp\{\frac{\alpha}{T}(N_i - N_j) + \frac{\beta}{T}(Z_i - Z_j)\}$$

$$\frac{\Gamma_i(E^*)}{\Gamma_j(E^*)} \propto exp\{\frac{\alpha}{T}\Delta N + \frac{\beta}{T}\Delta Z\} \quad (15)$$

As long as a linearization of the Q value remains valid, such " iso-scaling" behavior translates obviously into a corresponding scaling behavior for the yield ratios of the same given particle species from two different compound nuclei i and j of the same temperature T. Experimental isotopic yield ratios of the latter type have recently received much attention [4, 16, 22] and have been interpreted in terms of the overall nuclear symmetry energy, see below.

From the origin of Eq.(15) one can see the exponential dependence of the double ratio arises from any statistical model realization by expanding the entropy in terms of N and Z. Similar systematics have been made a number of times [2, 34, 35].

For the level density parameter a, the parametrization of Tõke and Swiatecki [31] was employed with $\alpha_V = 1/14.6$ MeV^{-1} and $\alpha_S = 4/14.6$ MeV^{-1}. In the calculations, assuming the saddle-point shape is represented by two touching spheres. V_{saddle} is the difference of deformation energy between the saddle-point shape and equilibrium-state shape, which is composed of the differences of Coulomb energy, volume energy, and surface energy between these two shape configurations. The nuclear temperature can be obtained from the commonly used Fermi-gas model relationship between the temperature T and the thermal excitation energy of the system E^*_{th}:

$$T = \sqrt{\frac{E^*_{th}}{a(\rho)}} = (\frac{\rho_{eq}}{\rho_0})^{1/3} a_0^{-1/2} \sqrt{E^*_{tot} - E_b(1 - \frac{\rho_{eq}}{\rho_0})^2}. \quad (16)$$

III. RESULTS AND DISCUSSION

It has been shown that the ratio of the fragment isotopic yields in two different nuclear reactions, 1 and 2, $R_{21} = Y_2(N,Z)/Y_1(N,Z)$, obey an exponential dependence on the fragment neutron number N and the proton number Z of the isotopes, an observation known as isoscaling [16]. The dependence is characterized by three parameters α, β and C:

$$R_{21}(N,Z) = C \cdot exp(\alpha N + \beta Z), \tag{17}$$

where C is an overall normalization constant. It was indicated [16, 22] that the isoscaling parameters α and β are related to the symmetry energy through a relation

$$\alpha = \frac{4C_{sym}}{T}[(\frac{Z}{A})_1^2 - (\frac{Z}{A})_2^2] \tag{18}$$

and

$$\beta = \frac{4C_{sym}}{T}[(\frac{N}{A})_1^2 - (\frac{N}{A})_2^2]. \tag{19}$$

Here Z_1, N_1, A_1 and Z_2, N_2, A_2 are the charge, neutron and the mass numbers of the source 1 and 2, respectively. T is the temperature of the system in MeV, C_{sym} is the symmetry energy.

In this work four equilibrated sources with proton number $Z_s = 76$ and mass numbers A_s = 165, 175, 185, and 195, are chosen at several initial excitation energies E^*_{tot}/A. Because sequential decay effects on the symmetry energy extracted from experimental data are still debated [9, 16, 27, 36–38], we focus on the primary fragments here.

Nuclear expansion plays two roles in our HIFG model calculations. On one hand, it reduces the energy available for fragment emission. On the other hand, it provides an estimation for the magnitude of the equilibrium density ρ_{eq} at which fragments with different isospins are emitted [i.e. Eq.(8)]. The influence of expansion on Coulomb energy is estimated through radius parameter $r_{coul} = r_0(\rho_{eq}/\rho_0)^{-1/3}$ [14] with r_0 being 1.16 fm [39].

Presently there is no a known formula that can describe the change of the symmetry energy with excitation energy very accurately, thus we adopt the following formulae, i.e. Eqs.(20) and (21), to model the evolution of the volume energy and the surface energy with system isospin I (defined as $(N-Z)/A$)), equilibrium density ρ_{eq}/ρ_0, and temperature T.

$$E_v(\rho_{eq}) = (-W_0 + \frac{K}{18}(1-\rho_{eq}/\rho_0)^2)(1-\kappa_v I^2)A, \tag{20}$$

and

$$E_s(T) = (\alpha_s(T) - T\frac{d\alpha_s(T)}{dT})(1-\kappa_s I^2)A^{2/3}. \quad (21)$$

where $W_0 = 16$ MeV and $K = 260$ MeV is the nuclear compressibility modulus [40]. $\alpha_s(T) = \alpha_s(\frac{T_c^2-T^2}{T_c^2+T^2})^{5/4}$ with $\alpha_s = 18$ and $T_c = 18$ MeV [22, 27]. We note the formula describing $\alpha_s(T)$ has been used by many authors (e.g., those in Refs.[27, 41]).

As is seen, Eqs.(20) and (21) are composed of two parts: (i) Terms $(1-\kappa_v I^2)$ and $(1-\kappa_s I^2)$, suggested in the liquid drop model (e.g., [42]), represent an isospin-dependent correction factor for the volume and surface energies, respectively. The constants κ_s and κ_v are taken as 2.3 and 1.927 [39]. (ii) Regarding the first term on the right side of Eq.(20) and Eq.(21), it describes a variation of the volume energy coefficient with the equilibrium density [40] and the effects of temperature on the surface energy coefficient, respectively. The latter can be derived with the free energy formula suggested in [22].

While Eqs.(20) and (21) have been demonstrated in previous studies [22, 39, 40] to provide a good description for the changes of $E_v(\rho_{eq})$ and $E_s(T)$ with excitation energy, when they are applied to the finite nuclei, it is still necessary to examine their validity in simulating the responses of the volume energy and the surface energy to a lowering in excitation energy due to thermal expansion.

Nuclear expansion leads to a lower density. As an example, we display in Fig.1 the results calculated at $E^*_{tot}/\mathrm{A} = 5$ MeV/nucleon where the ground-state density ρ_0 is reduced to $0.747\rho_0$. Solid points are theoretical values, solid lines are the linear fits to the data points. It is seen that these fitting lines are nearly parallel to each other and have almost equivalent distances between two successive elements for $Z = 5$ to 9 and $N = 5$ to 9 isotones. The observation indicates that isoscaling law is insensitive to the change of the density. That is to say, it does not depend on the nuclear expansion. A similar conclusion was also reached by others who employed different models [16, 27].

In recent work [28] we calculated isoscaling parameters α and β for several excitation energies (E^*) at the normal nuclear density, and showed that the magnitude of the symmetry energy extracted is unrelated to E^* (see Fig.5 and Fig.6 in Ref.[28]). Relative to the previous work, we also calculate α and β as a function of E^* here. The only difference with the former is that density is not the value of the saturation density but a function of E^*. A changing density (with E^*) is due to thermal expansion. Thus, the present calculations will test the density dependence of the symmetry energy.

The observables α and β can be constructed from the yield ratios of isotope fragments and isotone fragments, and extracted by reproducing the data points shown in Fig.1. The ratios have been calculated for four pair sources (A_2 = 175, A_1 = 165), (A_2 = 185, A_1 = 165), A_2 = 195, A_1 = 175) and (A_2 = 195, A_1 = 185). As an illustration, results corresponding to the former two pair sources are displayed in Fig.2 where the values of α and β extracted come from the evaluation for $Z = 6$ isotopes and $N = 6$ isotones at different excitation energies. The pronounced feature is that α is a decreasing function of excitation energy. It indicates that a decreasing α with increasing excitation energy observed recently in experiments [10, 11] appears naturally in the HIFG model. In addition, the changing trend of $|\beta|$ with excitation is predicted to be analogous to that of α, which is also in accordance with experimental observation [43].

Figure 3 depicts the symmetry energy extracted from α and β (which are evaluated for $Z = 6$ isotopes and $N = 6$ isotones) at various densities computed for four source pairs (A_2 = 175, A_1 = 165), (A_2 = 185, A_1 = 165), (A_2 = 195, A_1 = 185) and (A_2 = 195, A_1 = 175). In Fig.3 symbols without '$\times$' stand for the symmetry energy extracted with α [Eq.(18)] and those with '$\times$' with β [Eq.(19)]. Considering the generally used form for density-dependent symmetry energy, namely

$$E_{sym}(\rho) = C_0(\rho/\rho_0)^{\gamma}. \tag{22}$$

We use Eq.(22) to fit $E_{sym}(\rho)$ *vs.* ρ/ρ_0 as demonstrated in Fig.3. The line in the Fig.3 is the fit. It gives $C_0 \approx 31.0$, $\gamma \approx 0.73$. It is worth comparing the symmetry energy obtained in the present work with other independent studies in which different models and experimental observables were utilized to derive the $E_{sym}(\rho)$. They include expanding emitting source model and isotopic distributions [16], measurements of isospin diffusion [17], isospin dependent Boltzmann-Uehling-Uhlenbeck (IBUU) model and the isospin diffusion data [29], relativistic mean field interactions and the giant monopole resonance [44], statistical multifragmentation model and isotopic distributions [41], variational calculations and neutron stars [45], measurements of the neutron-proton emission ratio [46], and a constraint on binding energy, neutron skin thickness, isospin analog states using the mass formula of [47]. Such a comparison is plotted in Fig.4. It is easy to see the function form of the $E_{sym}(\rho)$ predicted in the HIFG model resembles that given in [41, 44–47] not only in the shape of the $E_{sym}(\rho)$ but also in its magnitude. It is also similar to that in [30] where the density dependence of the symmetry energy is suggested to be $31.6(\rho/\rho_0)^{0.69}$ based on a comparison of IBUU

calculations incorporating the isospin dependence of the in-medium nucleon-nucleon cross sections and isospin diffusion data. Particularly in [41], a symmetry energy of $E_{sym}(\rho) = 31.6(\rho/\rho_0)^{0.69}$ was reported via an isoscaling analysis of isotopes ratios for the Fe + Fe and Ni + Ni pair of reaction, and the Fe + Ni and Ni + Ni pair of reaction at 30, 40 and 47 MeV/nucleon, which is in good agreement with the present study. It is interesting to point out that the behavior of $E_{sym}(\rho)$ at subnormal density given in the present work is essentially consistent with the symmetry energy $E_{sym}(\rho) = 12.5(\rho/\rho_0)^{2/3} + 17.6(\rho/\rho_0)^{\gamma_i}$ with $\gamma_i = 0.4 - 1.05$ (denoted by two red lines in Fig.4), extracted very recently from simultaneous reproducing the the isospin diffusion data and the double neutron/proton ratio using an improved quantum molecular dynamics model [48].

The $E_{sym}(\rho)$ obtained here is based on several main assumptions: (i) A type of expansion called "self-similar expansion" is assumed in order to calculate the magnitude of the equilibrium density ρ_{eq} [i.e. Eq.(8)]; (ii) Fragment emission probability p comes from Weisskopf method and Toke's formalism for level density parameter [i.e. Eq.(4) and Eqs.(9)-(11)], and (iii) A form of Eqs.(20) and (21) is adopted to describe the changes of the volume and surface energies with excitation energy.

Our HIFG model calculations demonstrate clearly that a combination of these assumptions predicts a $E_{sym}(\rho)$ that is consistent with other theoretical approaches. The consistency appears to imply that these assumptions mentioned above, to a large extent, are reasonable.

However, it is important to improve our approach further in order to enhance its predicative power that will better guide the future experimental exploration. As one knows that the transition from normal to dilute nuclear density depends upon the stiffness of the nuclear matter as a function of excitation energy. The present method applied to deal with the thermal expansion as a type of self-similar fashion [12] is a first step towards a more realistic description of nuclear expansion. It does not consider the expansion to follow a manner that satisfies an isospin-dependent EOS. That will have an effect on the scaling as well. This is because expansion is directly responsible for the magnitude of the equilibrium density, which is one key parameter in model simulations and plays a critical role in deducing the density dependence of the symmetry energy. Another concern is on the validity of the formula suggested to describe the temperature dependence of the surface energy coefficient, $\alpha_s(T)$ [see Eq.(21)]. While the formula has some justification in infinite nuclear matter, whether its current form still holds in the case of finite nuclei demands a closer examination. For

example, the critical temperature $T_c = 18$ MeV assumed in $\alpha_s(T)$ and used in many work (e.g., Refs.[27, 41, 49]), including the present one, could be higher than that of finite nuclei. Thus, it would be extremely useful if we could have a formula more adapted to the finite nuclei case. To this end, we will employ other expressions for $\alpha_s(T)$ to access the symmetry energy via isoscaling techniques. In this sense we think the HIFG approach can provide a ground testing the validity of the various descriptions of $\alpha_s(T)$ proposed in the literature.

We note that the procedure that Shetty *et al.* [41] obtained the $E_{sym}(\rho)$ is as follows. First, experimental information on isoscaling parameters α at different excitation energies is extracted by fitting the measured isotopic yields data for several reaction systems. Then experimental isoscaling parameter was compared with the predictions of the statistical model calculations. The break-up density at which fragments are produced was varied in the calculation and taken to be multiplicity-dependent. It differs for different excitation energies. Finally, the symmetry energy in the calculation was adjusted until a reasonable agreement between the calculated and the measured α was obtained. After a series of the formal steps, $E_{sym}(\rho)$ was deduced. In contrast, our approach of obtaining the $E_{sym}(\rho)$ is based on the HIFG model alone, and it does not depend on particular experimental data. This illustrates that our approach is of a strong predictive power for various types of reaction systems and observables.

IV. SUMMARY AND CONCLUSIONS

In summary, using the HIFG model that considers nuclear expansion, we have obtained the following results: (i) No discernable influence of the nuclear expansion on the isoscaling law is found; (ii) A drop of the experimental observed isoscaling parameter α at high excitation energy is theoretically predicted, and (iii) A symmetry energy of $E_{sym}(\rho)$ $\approx 31.0(\rho/\rho_0)^{0.73}$ is derived. Therefore, we conclude that the HIFG model is a useful tool to probe the density dependence of the nuclear symmetry energy.

While contrasting predictions have been made on the effect of sequential decay on the isoscaling parameters (e.g., [19, 41, 50, 51]), it is clear that the issue should be investigated in the framework of the HIFG model.

Because the observable that is actually measured in experiment is the fragment yield

distributions, confronting the output of a theoretical model with experimental isotopic distributions is more direct than double ratios which have to be reinterpreted. The systematic isotopic distributions were noticed in the past [2, 34, 35]. There, the isotopic distributions were shown to basically reflect the underlying potential energy surfaces (PES) (e.g. liquid-drop model PES), if they result from statistical decay. As demonstrated above, the HIFG model predicts a reasonable $E_{sym}(\rho)$. On the basis of the result, we believe the HIFG model can calculate the isotopic distributions of fragments well. By fitting the distributions, the variance of fragment distributions for a certain A (or Z) can be extracted. Considering the relationship between the variance and the curvature of the PES at the saddle point for dinuclear configurations in the vicinity of the minimum (see [2] for a review), information on the latter can be obtained accordingly. The work along this direction is underway.

ACKNOWLEDGMENTS

This work has been supported by the U.S. Department of Energy Grant No. DE-FG02-88ER40414. The work of W.Y has also partially been supported by the Scientific Research Foundation of the Ministry of Education of Chine for Returned Overseas Scholars (2009). W.Y is also grateful to Rochester University for support and hospitality extended to him.

[1] *Isospin Physics in Heavy-ion Collisions at Intermediate Energies*, edited by Bao-An Li and W. Udo. Schröder (Nova Science Publishers), Inc., New York, 2001.

[2] W. U. Schröder and J. R. Huizenga, *Damped Nuclear Reactions*, in *Treatise on Heavy-Ion Science* edited by D.A. Bromley (Plenum Press), New York and London, Vol. 2, 113 (1984) and references cited.

[3] V.Baran, M.Colonna, V.Greco, and M. Di Toro, Phys. Rep. **410**, 335 (2005).

[4] B.A.Li, L.W.Chen, and C.M.Ko, Phys. Rep. **464**, 113 (2008).

[5] B.A.Brown, Phys. Rev. Lett. **85**, 5296 (2000).

[6] J.M.Lattimer and M.Prakash, Phys. Rep. **333**, 121 (2000).

[7] B.A.Li and L.W.Chen, Phys. Rev. C **74**, 034610 (2006).

[8] D.V.Shetty et al., J. Phys. G **36**, 075103 (2009) [arXiv: nucl-ex/0802.0664].

[9] D.V.Shetty et al., Phys. Rev. C **70**, 011601(R) (2004).

[10] A.Le.Fevre et al., Phys. Rev. Lett. **94**, 162701 (2005).

[11] J.Iglio et al., Phys. Rev. C **74**, 024605 (2006).

[12] W.A.Friedman, Phys. Rev. Lett. **60**, 2125 (1988); Phys. Rev. C **42**, 667 (1990).

[13] J.Tõke and W.U.Schröder, Phys. Rev. Lett. **82**, 5008 (1999).

[14] J.Tõke, J.Lu, and W.U.Schröder, Phys. Rev. C **67**, 034609 (2003); C **67**, 044307 (2003); C **72**, 031601(R) (2005).

[15] J.Tõke and W.U.Schröder, Phys. Rev. C **79**, 064622 (2009).

[16] M.B.Tsang et al., Phys. Rev. Lett. **86**, 5023 (2001); Phys. Rev. C **64**, 054615 (2001) .

[17] M.B.Tsang et al., Phys. Rev. Lett. **92**, 062701 (2004).

[18] D.V.Shetty, G.A.Souliotis, S.Galanopoulos, and S.J.Yennello, Phys. Rev. C **79**, 034603 (2009).

[19] A.Ono et al., Phys. Rev. C **68**, 051601(R) (2003).

[20] J.Y.Liu et al., Nucl. Phys. A **811**, 223 (2008).

[21] G.Lehaut, F.Gulminelli, and O.Lopez, Phys. Rev. Lett. **102**, 142503 (2009); C.B.Das and S.Das Gupta, Nucl. Phys. **A812**, 149 (2008); Y.G.Ma et al., Phys. Rev. C **69**, 064610 (2004).

[22] A.S.Botvina et al., Phys. Rev. C **65**, 044610 (2002).

[23] E.Geraci et al., Nucl. Phys. **A732**, 173 (2004).

[24] M.Veselsky et al., Phys. Rev. C **69**, 044607 (2004).

[25] Ad.R.Raduta and F.Gulminelli, Phys. Rev. C **75**, 024605 (2007).

[26] W.D.Tian et al., Phys. Rev. C **76**, 024607 (2007).

[27] S.R.Souza et al., Phys. Rev. C **78**, 014605 (2008); C **80**, 041602(R)(2009).

[28] W.Ye, J.Tõke, and W.U.Schröder, Phys. Lett. B **676**, 193 (2009) [arXiv: nucl-th/0808.1917].

[29] L.W.Chen, C.M.Ko, and B.A.Li, Phys. Rev. Lett. **94**, 032701 (2005).

[30] B.A.Li and L.W.Chen, Phys. Rev. C **72**, 064611 (2005).

[31] J.Tõke and W.J.Swiatecki, Nucl. Phys. **A372**, 141 (1981).

[32] J.B.Natowitz et al., Phys. Rev. C **66**, 031601(R) (2002).

[33] V.F.Weisskopf, Phys. Rev. **52**, 295 (1937).

[34] V.V.Volkov, Phys. Rep. **44**, 93 (1978).

[35] C.K.Gelbke et al., Phys. Rep. **42**, 311 (1978).

[36] A.Ono et al., axXiv: nucl-ex/0507018.

[37] M.B.Tsang et al., Eur. Phys. J. A **30**, 129 (2006).

[38] D.V.Shettey, S.J.Yennello, et al., axXiv: nucl-ex/0603016.

[39] P.Möller and J.R.Nix, Nucl. Phys. **A361**, 117 (1981).

[40] N.Buyukcizmeci, A.S.Botvina, I.N.Mishustin, and R.Ogul, Phys. Rev. C **77**, 034608 (2008).

[41] D.V.Shetty, S.J.Yennello, and G.A.Souliotis, Phys. Rev. C **76**, 024606 (2007).

[42] R.J.Charity, Nucl. Phys. A **483**, 371 (1988).

[43] J.Iglio et al., Phys. Rev. C **74**, 024605 (2006).

[44] J.Piekarewicz, *Proceedings of the International Conference on Current Problems in Nuclear Physics and Atomic Energy*, Kyiv, Ukraine, May 29-June 3, 2006.

[45] H.Heiselberg and M.Hjorth-Jensen, Phys. Rep. **328**, 237 (2000).

[46] M.A.Famiano et al., Phys. Rev. Lett. **97**, 052701 (2006).

[47] P.Danielewicz, arXiv: nucl-th/0411115.

[48] M.B.Tsang, Y.X.Zhang, P.Danielewicz, M.Famiano, Z.X.Li, W.G.Lynch, and A.W.Steiner, Phys. Rev. Lett. **102**, 122701 (2009) [arXiv:nucl-ex/0811.3107].

[49] G.Chauhuri, F.Gulminelli, and S. Das Gupta, Phys. Rev. C **80**, 054606 (2009).

[50] W.D.Tian et al., arXiv: nucl-th/0601079.

[51] M.Huang, Z.Chen, S.Kowalaski, Y.G.Ma, R.Wada, T.Keutgen, K.Hagel, J.Wang, L.Qiu, J.B.Natowitz, T.Materna, M.Barbui, C.Bottosso, M.R.D.Rodrigues, and A.Bonasera, [arXiv:

nucl-ex/1001.3621.

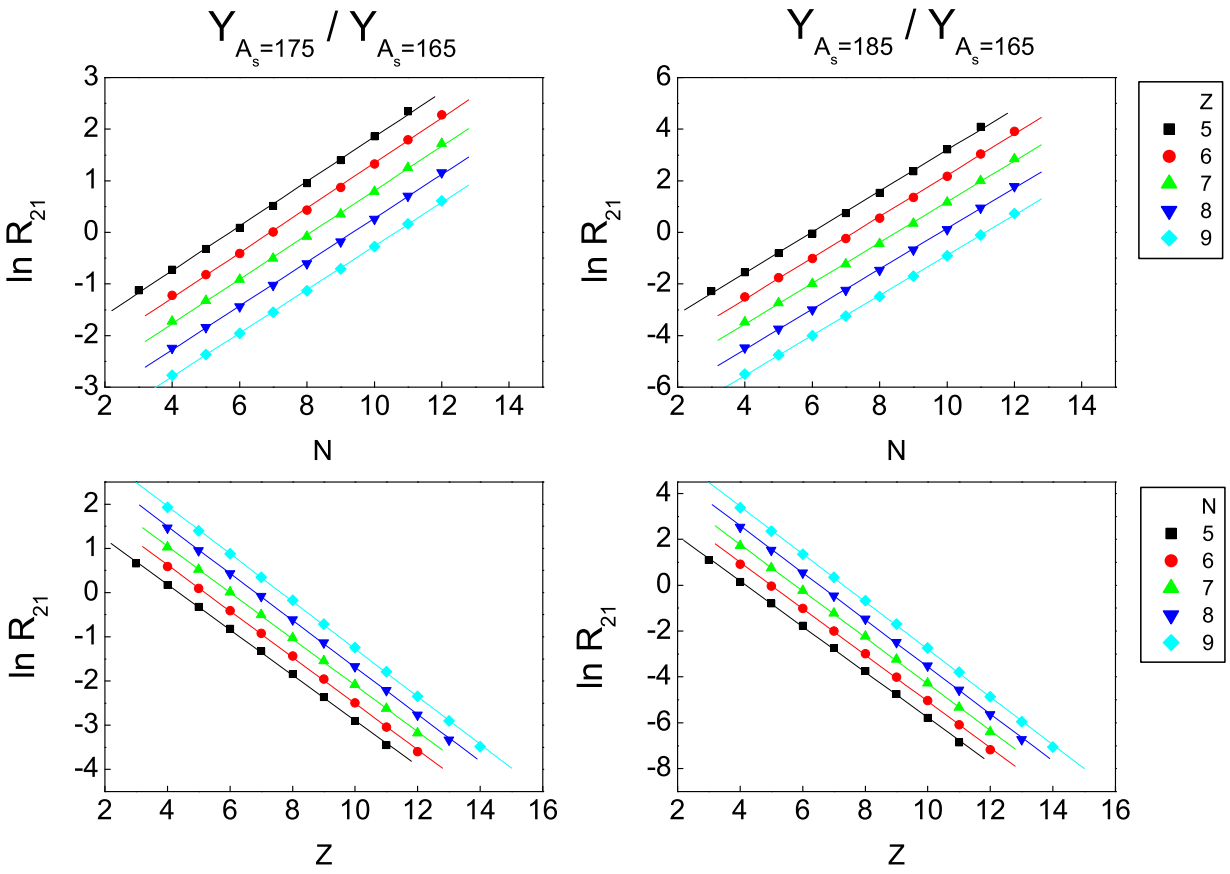

FIG. 1: (Color online) The logarithm of the ratio of elements $Z = 5-9$ isotope yields (top panel) and of $N = 5-9$ isotone yields (bottom panel) from source pairs $A_s = 175$ and $A_s = 165$ (left column) as well as from source pairs $A_s = 185$ and $A_s = 165$ (right column) at an excitation energy of $E^*_{tot}/A = 5$ MeV. Solid lines represent the linear fitting to the data points.

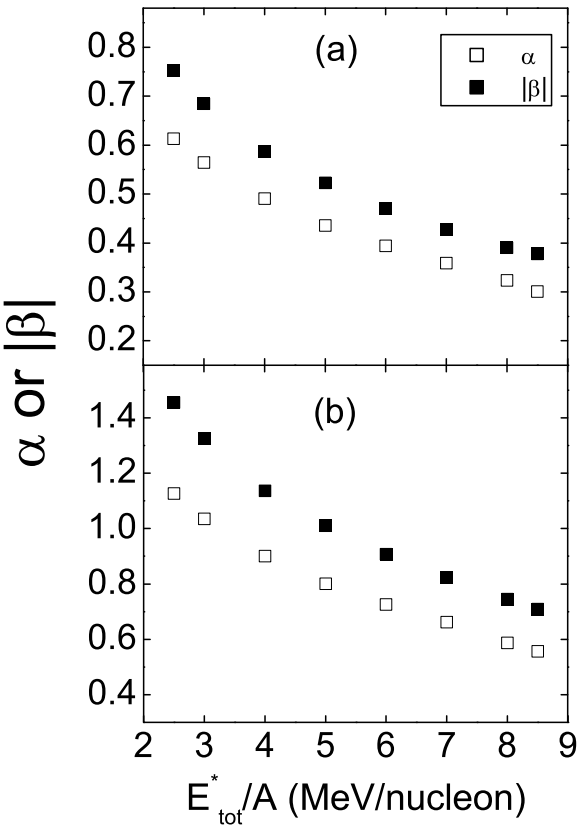

FIG. 2: Dependence of isoscaling parameters α and $|\beta|$ on excitation energy for (a) source pairs $A_s = 175$ and $A_s = 165$ as well as for (b) source pairs $A_s = 185$ and $A_s = 165$.

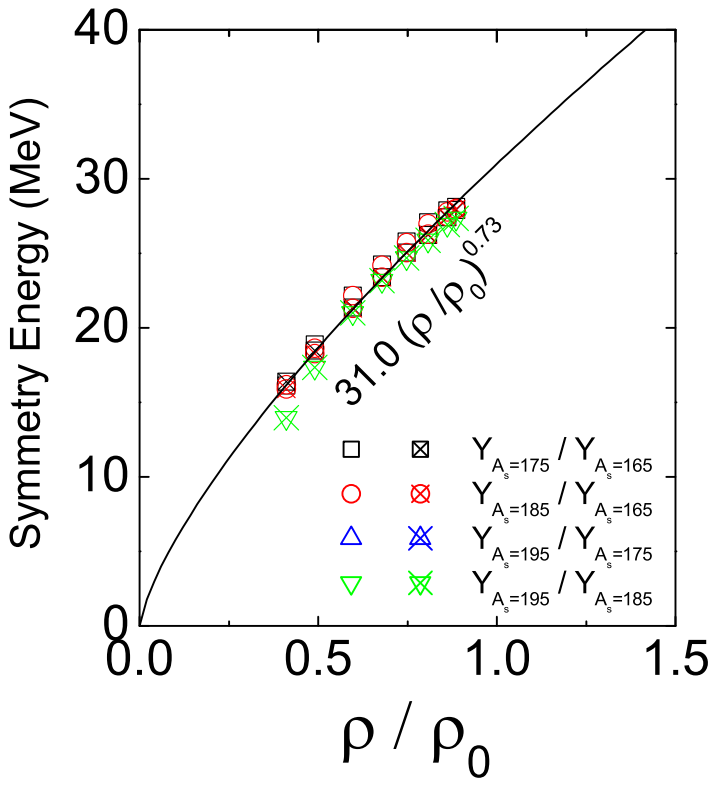

FIG. 3: (Color online) Symmetry energy at various densities extracted through α and β for four source pairs. The solid line represents the fit. See text for details.

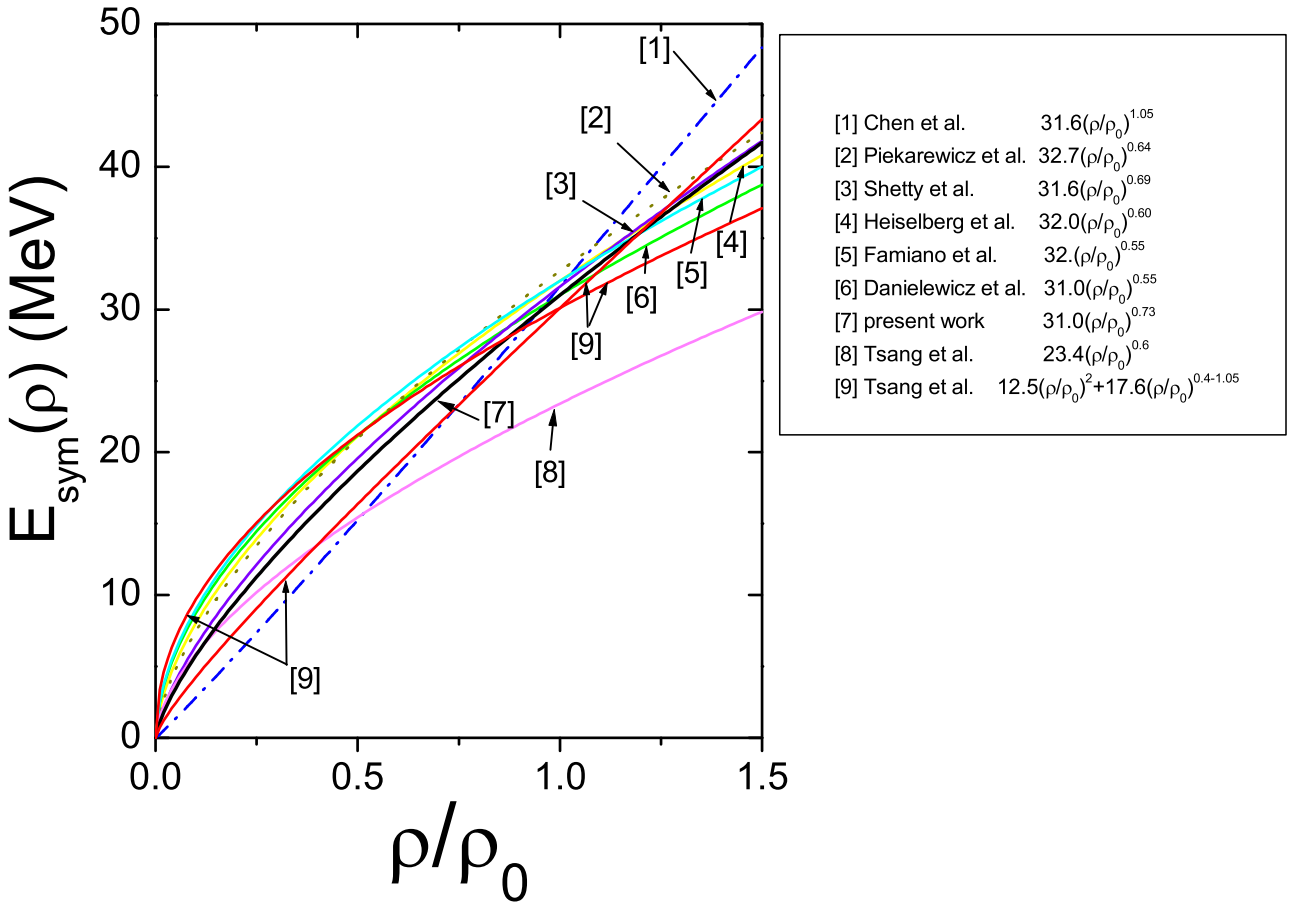

FIG. 4: (Color online) Comparison of the density dependence of the symmetry energy obtained in the present work and other independent works. Here symbols [1]-[6] denote the symmetry energy given in Ref.[29], Ref.[44], Ref.[41], Ref.[45], Ref.[46] and Ref.[47], respectively. Symbols [8] and [9] represent the $E_{sym}(\rho)$ reported in Ref.[16] and Ref.[48]. Symbol [7] is the HIFG model prediction.

Isoscaling in the decay of projectile-like fragments originating from identical ^{48}Ca projectiles reacting with isotopically different targets of ^{112}Sn and ^{124}Sn at 45 MeV/A

H. Singh[1], M.J. Quinlan[1], J. Tõke[1], I. Pawełczak[1], E. Henry[1], W.U. Schröder[1], F. Amorini[2], A. Anzalone[2], C. Maiolino[2], L. Auditore[3], D. Loria[3], A. Trifiró[3], M. Trimarchí[3], G. Cardella[4], E. De Filippo[4], A. Pagano[4], M.B. Chatterjee[5], S. Cavallaro[6], E. Geraci[6], M. Papa[4], S. Pirrone[4], G. Verde[4], A. Grzeszczuk[7], P. Guazzoni[8], L. Zetta[8], E. La Guidara[9], G. Lanzalone[10], S. Lo Nigro[6], G. Politi[6], D. Loria[11], F. Porto[12], F. Rizzo[12], P. Russotto[12], M. Vigilante[13][1, 2, 3, 4, 5, 6, 7, 8, 9, 10, 11, 12, 13]

[11] *Departments of Chemistry and Physics University of Rochester, Rochester NY*

[22] *INFN Laboratori Nazionali del Sud, Catania, Italy*

[33] *INFN gruppo coll. Di Messina & Dipartimento di Fisica Universitá di Messina*

[44] *INFN Sezione di Catania*

[55] *Saha Institute for Nuclear Physics, Kolkata, India*

[66] *INFN Sezione di Catania & Dipartimento di Fisica e Astronomia Universitıa di Catania*

[77] *Institut of Physics, University of Silesia, Katowice, Poland*

[88] *INFN Sezione di Milano & Dipartimento di Fisica Universitá di Milano*

[99] *INFN Sezione di Catania & CSFNSM, Catania, Italy*

[1010] *INFN Laboratori Nazionali del Sud,*

Catania, Italy & Universitá KORE Enna, Italy

[1111] *INFN gruppo coll. Di Messina & Dipartimento di Fisica Universitá di Messina*

[1212] *INFN Laboratori Nazionali del Sud, Catania,*

Italy & Dipartimento di Fisica e Astronomia Universitıa di Catania

[1313] *INFN Sezione di Napoli & Dipartimento di Fisica Universitá Federico II di Napoli*

Abstract

The yield of intermediate mass fragments (IMFs) Z=3-7, emitted from excited primary projectile like fragments (PLFs) in damped ^{48}Ca + ^{112,124}Sn reactions at 45 MeV/A, is used to study isoscaling. The measured yield ratios of these fragments are found to obey the exponential law of isoscaling. Inclusive yield of IMFs was subjected to an angle restriction on the out of plane data ($\cos(\phi) \leq 0.4$), which is assumed to contain, primarily statistical component of fragment yields. The observed isoscaling behaviour does not show any significant sensitivity to the angle cut in the present study. Another constraint on the normalized relative velocity between IMFs and projectile remnants ($1.0 \leq v_{rel}/v_c \leq 2.0$), which ensures the origin of two fragments to be fast moving projectile like fragment only, also do not show any significant change in the isoscaling parameters. Finally, assuming similar temperatures (T) in the two reactions, ratios were scaled with saddle point energies for the decay of excited PLFs into IMFs and heavy fragments, using the expression $\exp(\Delta B/T)$, where, ΔB is the binding energy difference for the emission of an IMF from two different sources. Such scaling behaviour may be used to estimate the size and temperature of the decaying system in the two cases.

PACS numbers: 25.70.Pq,25.70.Mn

I. INTRODUCTION

The study of intermediate mass fragments (IMFs) produced in multifragmentation reactions has been widely used as a tool to understand the nuclear reaction mechanisms [**?** **?** **?**]. In the last decade, such studies have been extended to explore the isoscaling phenomenon in those reactions [**?** **?** **?** **?** **?**]. Isoscaling is considered as a vital tool to calculate the symmetry energy term in the nuclear equation of state, which along with exploring the reaction dynamics has relevance in astrophysical applications.

In general, isoscaling is observed by comparing the relative isotopic yields of fragments from reactions having isotopically different projectiles and/or targets at similar temperature. The ratio R_{21}(N, Z), of yields of a given fragment type produced from two different sources has an exponential dependence on neutron (N) and proton (Z) numbers of the fragment and the relation is described as,

$$R_{21}(N,Z) = Y_2(N,Z)/Y_1(N,Z) = Cexp(\alpha N + \beta Z), \tag{1}$$

where three parameters, C, α & β describe the overall isoscaling behaviour [**?**]. The index 2 corresponds to neutron rich source and 1 to neutron poor.

Isoscaling has been observed in a variety of nuclear reactions, for e.g, multifragmentation, evaporation and damped collisions [**?** **?** **?** **?**] etc., where fragment (IMFs or heavy fragments) yield ratios are compared either from the projectile fragmentation or target fragmentation or the fragments arising from a central collision. For the break-up of an equilibrated multifragmenting system, Ono et al. [**?**] derive an approximate grandcanonical expression relating the symmetry energy coefficient C_{sym}, and the observed isotopic composition of fragments originating from the break-up of two sources with similar sizes and temperatures. This relationship is reproduced in Eq. 2 below.

$$\alpha T = 4C_{sym}\left[\left(\frac{Z}{A}\right)_1^2 - \left(\frac{Z}{A}\right)_2^2\right] = 4C_{sym}\Delta(Z,A), \tag{2}$$

$$\beta T = 4C_{sym}\left[\left(\frac{N}{A}\right)_1^2 - \left(\frac{N}{A}\right)_2^2\right] = 4C_{sym}\Delta(N,A). \tag{3}$$

In the above equation, Z, N and A are the protons, neutrons and mass numbers of the decaying systems in the two reactions. The parameter $\Delta(Z,A)$ or $\Delta(N,A)$ represents the isospin difference between the two sources.

The common signature of isoscaling studies is to use two different reactions, one having neutron rich projectile and target as compared to the other of a given element. Two important assumptions in achieving isoscaling are; non-statistical emission of particles is negligible or cancels out in the ratios, and the decaying systems in different reactions have similar temperatures. It is possible to check the validity of such assumptions by looking at isoscaling for out-of-plane reaction events. Since dynamical emission lies essentially in the reaction plane [**?**], out-of-plane events are expected to have relatively very low contribution from dynamical emission and the data may be assumed to contain events originating from the statistical split only. Out-of-plane is defined by the normal to reaction plane (n) and the break-up axis of the projectile like fragment (PLF) while reaction plane is defined by the beam axis and the direction of PLF [**?**]. The out-of-plane angle ϕ specifies the deflection of the break-up axis with respect to the normal direction. Values of 0^0 and 180^0 for ϕ implies that one of the fragment is emitted either in the direction of n or in a direction completely opposite to n, while $\phi = 90^0$ indicates that break-up axis lies in the reaction plane. As discussed before, one of the main goal of such studies is to calculate the symmetry energy coefficient using experimental values of slope parameters and isotopic compositions of the two decaying systems, it is practically impossible to know the exact source of IMF emission without complete reconstruction, which is possible only in case of non-central collissions.

A study of isoscaling from projectile residues Z=10-36 from ^{86}Kr arising from different reactions at 25 MeV/A was reported by Souliotis et al. [**?**], but there are no further investigations of isoscaling in intermediate energy region, using the yields of IMFs from the decay of similar & excited PLFs, originating after the interaction of a incident heavy ion beam with different targets having different N/Z ratios.

Present study reports the experimental investigation of isoscaling from the splitting of PLFs in two reactions, ^{48}Ca + ^{124}Sn & ^{48}Ca + ^{112}Sn at 45 MeV/A of lab energy. We have studied isoscaling subjected to out-of-plane angle and relative velocity constraints on inclusive data, which would help us in verifying some of main assumptions of the said phenomenon. A novel method of scaling of yield ratios with the expression exp(ΔB/T), shows that isoscaling is followed from the mass differences of the decaying primary fragments. Such measurements offer a new dimension to study the isoscaling phenomenon as they can be used to estimate the isospin difference (Δ) as well as temperature (assuming similar) of the decaying systems; both are the necessary ingredient for calculating C_{sym}.

II. EXPERIMENTAL DETAILS

The experiment was carried out using the K800 cyclotron at Laboratori Nazionali del Sud (LNS), Catania, Italy. Isotopically enriched, self supporting targets of ^{124}Sn and ^{112}Sn having thicknesses of 689 μg/cm^2 and 627 μg/cm^2 respectively, placed inside the Charged Heavy Ion Mass and Energy Resolving Array (CHIMERA), were bombarded with ^{48}Ca beam of 45 AMeV energy. The pulsed beam had a repetition rate of 120 ns. The CHIMERA array, arranged in 4π geometry, consists of 1192 ΔE-E (Si-CsI(Tl)) telescopes, which covers $\simeq$94% of the total solid angle. Each telescope consists of a 300-μm thick silicon detector, while CsI(Tl) detectors have different thicknesses as a function of polar angle. More details about the array can be found in Refs. [**? ? ?**].

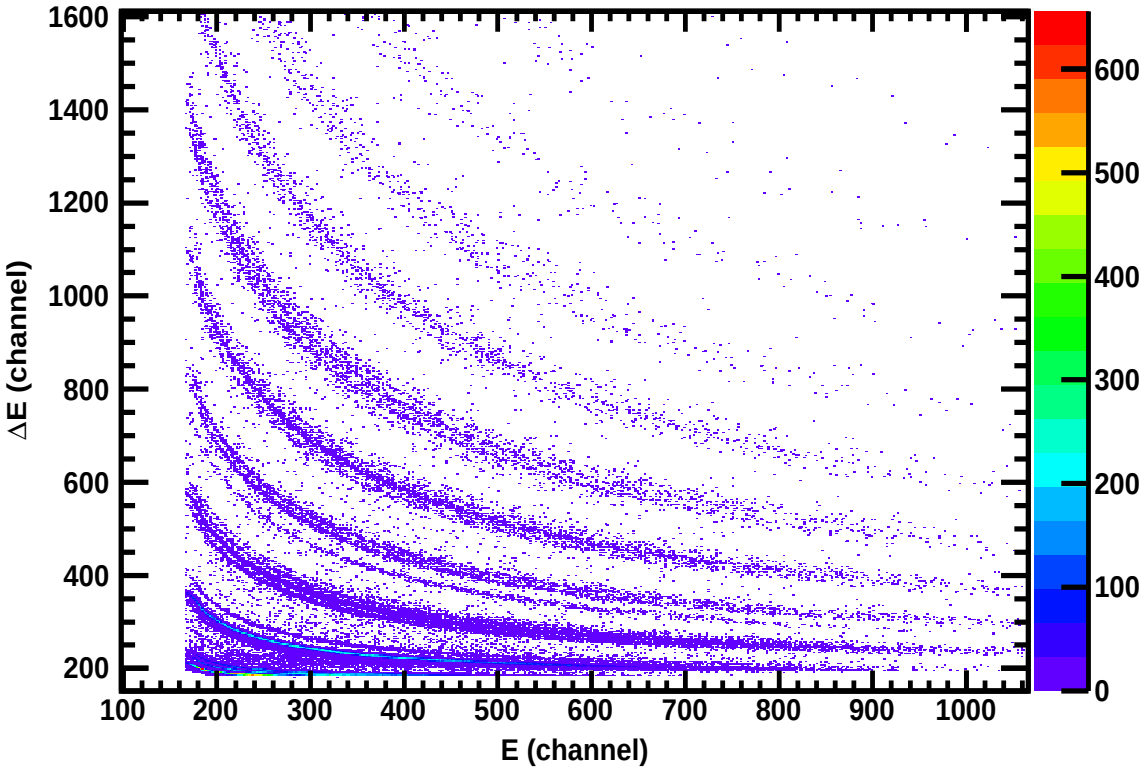

FIG. 1: Correlation contours for different elements taken from ^{48}Ca + ^{124}Sn reaction at laboratory angle $\theta = 19^0$.

Energy calibration for silicon detectors was carried out using various beams like ^{12}C,

^{16}O from MP Tandem accelerator at different energies. Data acquisition was set to trigger on minimum bias condition of $\geq$2. This hardware condition combined with various other restrictions applied in offline analysis helps in eliminating any possible ambiguity related to the source of two body events in the data. Reaction products were characterized in charge (Z), mass (A) and energy using the time of flight (TOF), energy and light output information obtained from ΔE-E telescopes. Data collected in the forward region ($6.0 \leq \theta \leq 20.0$) were used in the present study. A 2-dimensional correlation plot of the raw data, showing a very good isotopic separation for different elements from Z = 1-9 is shown in Fig. 1. The missing spectra for the first $\approx$160 channels on the x-axis is explained by the energy threshold required to trigger the electronics.

In order to get the yield of different isotopes from the two reactions, the two dimensional ΔE-E distributions were linearized using a calculation of the distance between the data point of a spline fit to the most abundant isotope of each element and the closest chosen lines [**?**]. Fig. 2 shows a linearized plot for the Li-isotopes obtained from ^{48}Ca + ^{124}Sn reaction. Red line is a summed Gaussian fit to different isotopes. A good isotopic resolution of the detection system is clearly visible in this figure. It also shows the production probability to be maximum for the β-stable isotope, which is ^{7}Li in the present case.

III. RESULTS AND DISCUSSION

The yield of isotopes of different elements (Z=3-7) was integrated over the entire set of data from the two reactions. Mass of each particle was assigned based on its distance from the β-stable isotope. However, Monte Carlo method was used to assign the mass in the overlapping region (cf. Fig. 2). An angular range in the forward region $6.0 \leq \theta \leq 20.0$ was considered for enhanced statistics. Shown in Fig. 3 are the yields of Li isotopes from the two reactions. Yields were normalized to the number of elastic events before plotting in this figure. The observed difference in yields of different isotopes in the two reactions increases with the size of the isotope, which eventually becomes the source of isoscaling.

Experimentally obtained yields of various IMFs were fitted with Eq. (1) as a function of neutron number of the isotopes. Fig. 4 shows the isoscaling behaviour for different isotopes. The value of isoscaling parameter α was found to be independent of fragment Z, which if found otherwise, could be considered as a signature of strong surface dependence of the

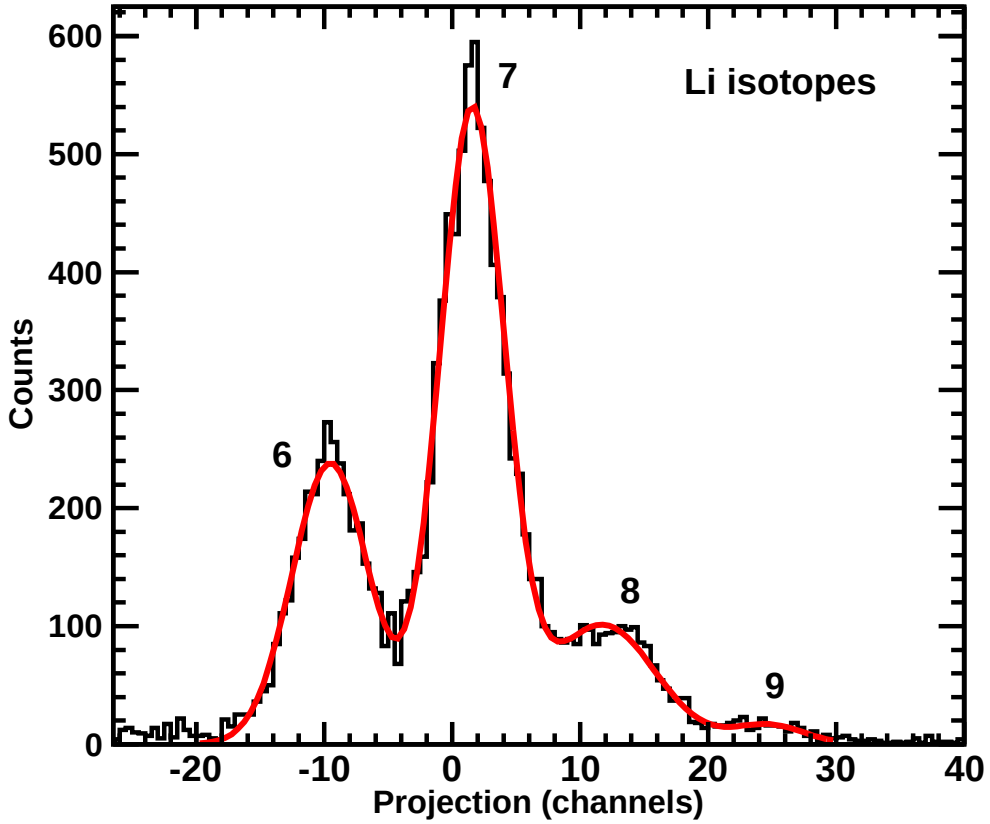

FIG. 2: A projected histogram of Li-isotopes taken from ^{48}Ca + ^{124}Sn reaction

symmetry energy [**?**]. A straight line trend of global scaling of yield ratios, which is defined as,

$$S(N) = R_{21}(N, Z)exp(-Z\beta) = Cexp(\alpha N), \tag{4}$$

is considered as a test of goodness of the isoscaling behaviour. A semilog plot of such trend for the present data is shown in Fig. 5. Clearly, all isotopes of different IMFs follow a straight line trend.

Global scaling of yield ratios shows a good agreement with a single value of α (0.230) and β (-0.122). The α values extracted from isoscaling fits to different elements are shown in Fig. 6.

It is clear from eq. (2) that beside excitation energy, magnitude of α also depends on difference in composition (N/Z) of the two decaying systems. As discussed in the introduc-

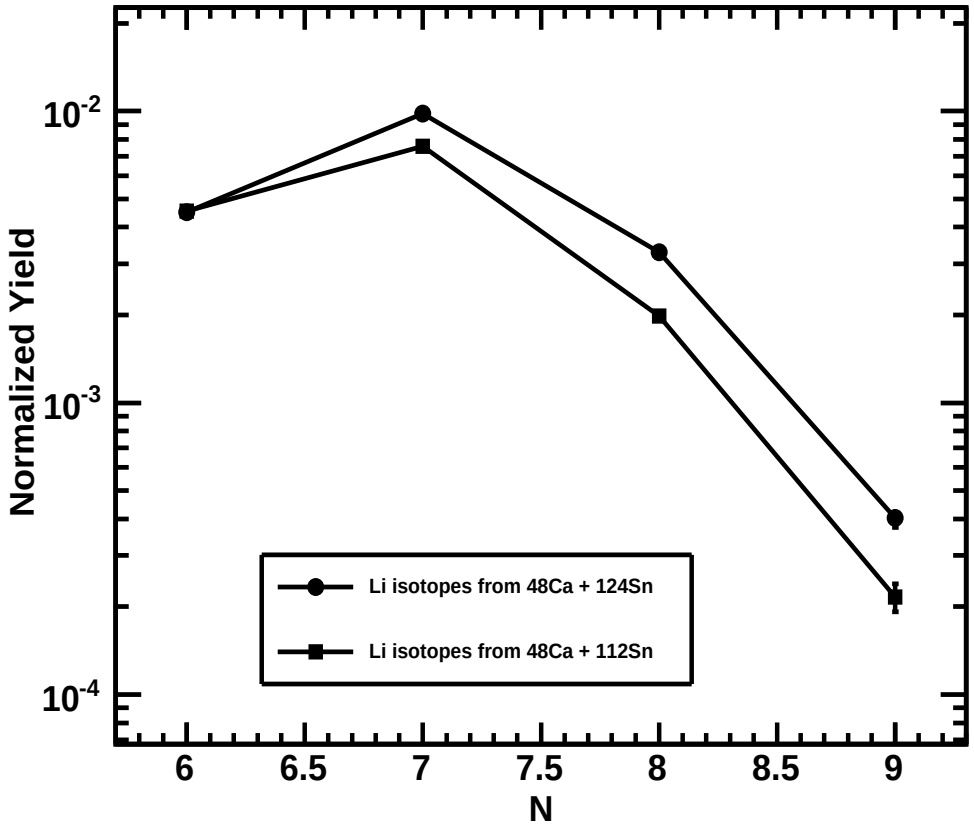

FIG. 3: Normalized to elastic yields of Li-isotopes. Lines are drawn to guide the eye. Except for ^{9}Li isotopes in the two reactions, error bars are smaller than the symbol size.

tion, isoscaling in the present study is observed from the decay of similar PLFs, after the interaction of ^{48}Ca beam with different targets. This may be the reason for smaller value of α as compared to the existing works [**? ? ?**].

As a next step, a cut on the relative velocity between the IMF and projectile remnant, normalized to the velocity (v_c) calculated based on purely Coulomb split ($1.0 \leq v_{rel}/v_c \leq 2.0$) was applied to study the isoscaling. Importance of such cut lies in eliminating the contamination from target, if any, as those events are expected to have a large relative velocity. A slight increase in the values of isoscaling parameters, α (0.250) & β (-0.129) was observed using such a cut, which indicate the possiblity of events admixture in the inclusive data.

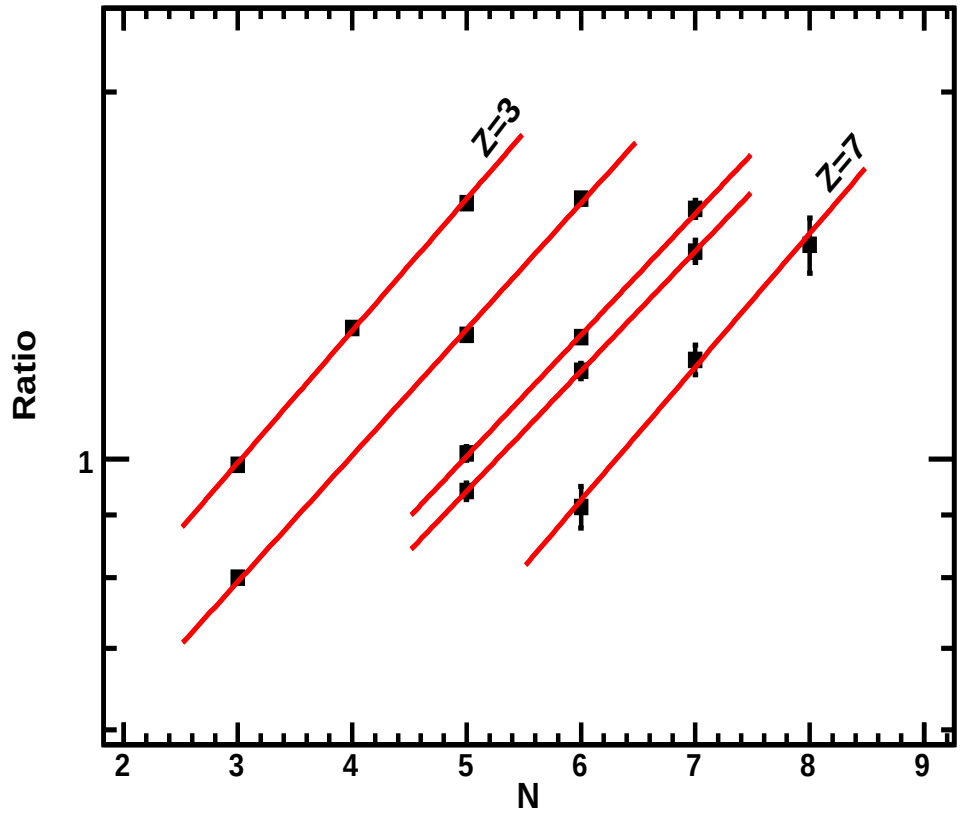

FIG. 4: Isoscaling from projectile fragmentation from ^{48}Ca + ^{124}Sn & ^{48}Ca + ^{112}Sn reactions.

Isoscaling was also studied for out of plane events. An out of plane angle cut ($\cos(\phi) \leq 0.4$), was used to study the isoscaling. As discussed already, importance of such gating lies in eliminating any possible contamination of the data by non-statistical component. Such tests are useful in verifying one of the main assumption of isoscaling analysis that dynamical effects cancels out in ratios & isoscaling is the result of events arising from the statistical split only. Parameters found were very similar to what we got from the relative velocity cut and their values extracted from the fits are α (0.247) & β (-0.127).

Assuming the Weisskopf formalism [**?**] of particle emission probability (Γ) to be valid for IMFs emission from an excited PLF,

$$\Gamma \propto e^{\Delta S}, \tag{5}$$

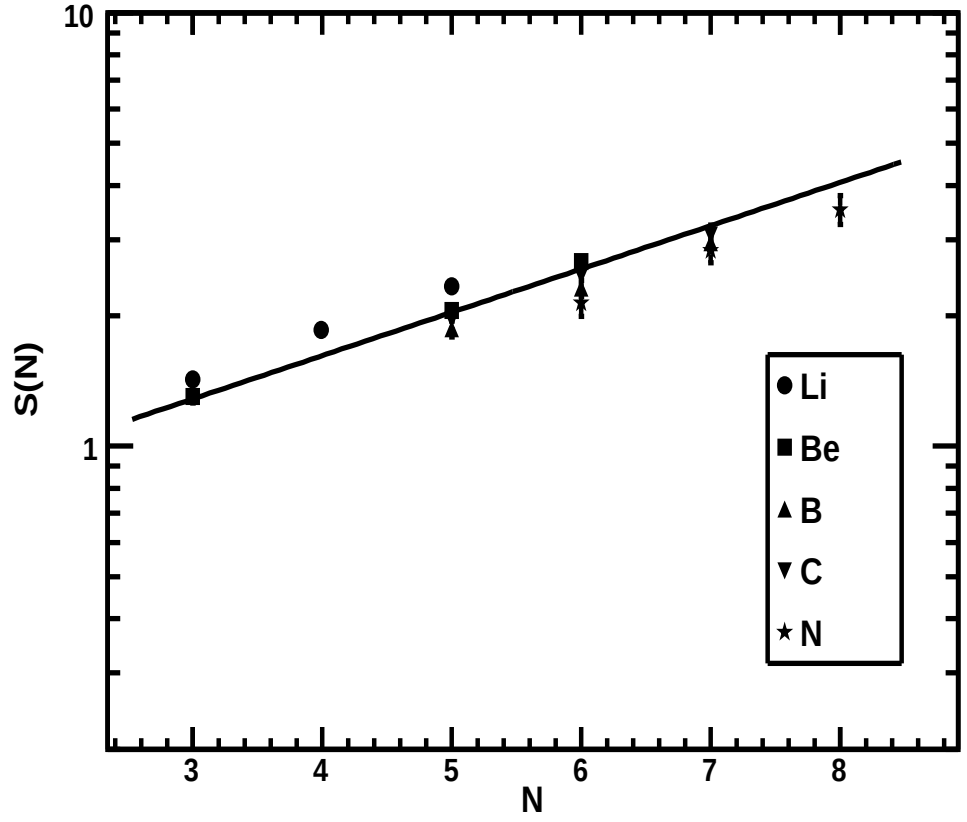

FIG. 5: Global scaling as a function of the neutron number using the best fit value of β obtained from fitting various IMFs.

where ΔS, change in entropy is calculated as,

$$\Delta S = S_{saddle} - S_{eq}. \tag{6}$$

S_{saddle} represents entropy at saddle point corresponding to the configuration of touching spheres and S_{eq} is the entropy at equilibrium configuration of the PLF. This change in entropy can be approximated in terms of reaction Q-value and Coulomb barrier for a given split of PLF as,

$$\Delta S = \simeq -(Q + V_c)/T. \tag{7}$$

Using the above expression for ΔS in Eq.(5),

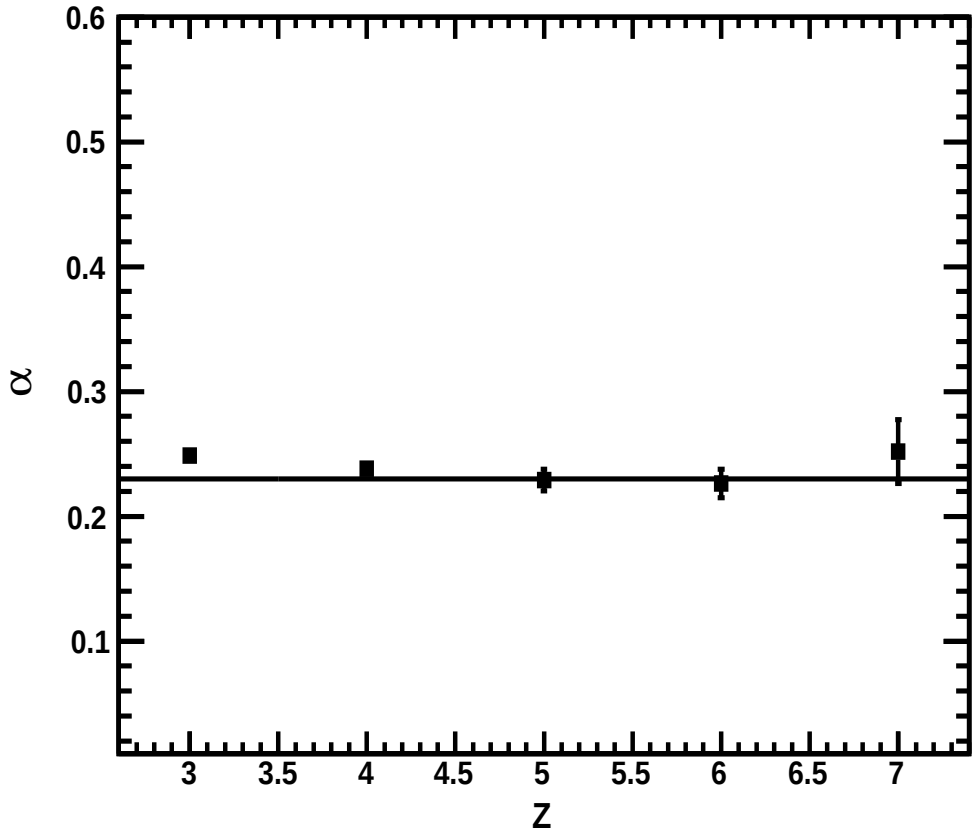

FIG. 6: Variation of α with fragment Z. Global value used is shown by straight line.

$$\Gamma \propto exp[-(Q + V_c)/T] = exp[(B - V_c)/T], \tag{8}$$

For the yield of IMFs originating from neutron rich(2) and neutron poor systems(1) can be written as,

$$\Gamma_2 = exp[(B_2 - V_{c2})/T_2], \tag{9}$$

$$\Gamma_1 = exp[(B_1 - V_{c1})/T_1]. \tag{10}$$

Assuming similar temperature for the two quasiprojectiles ($T_1 \simeq T_2 = T$) originating from ^{48}Ca + ^{124}Sn and ^{48}Ca + ^{112}Sn reactions, yield ratios would become a function of binding energy difference corrected for Coulomb of the two decaying systems as,

$$R_{21} = \Gamma_2/\Gamma_1 \simeq exp[(B_2 - V_{c2} - B_1 + V_{c1})/T] = exp[(\Delta B - \Delta V_c)/T]. \tag{11}$$

Where, ΔB represents difference in binding energies of IMFs from primary neutron rich and neutron poor system, respectively. The Coulomb correction, though expected to be negligible due to the very similar sizes of two PLFs, was applied to above expression and a search was made for the Z & A of the two possible nuclei, whose binding energy difference for break-up into different IMFs would follow the experimental yield ratios. The possible candidates found are $Z_1 = 26$, $A_1 = 69$, $Z_2 = 23$ & $A_2 = 59$. Values of fit parameters, a1 (0.866), a2 (0.341), where a1 is a constant and a2 is the inverse of temperature. Using the sizes and temperature calculated from the fit, C_{sym} was found to be 19.08 MeV. Smaller value of symmetry energy coefficient as compared to standard value of ≈25 MeV, could be interpreted as a sign of dilute matter at freeze-out. A semi-log plot of scaling of experimental ratios with Eq.(11) for these two nuclei is shown in Fig. 7. Though there is Coulomb term in the analysis but the plot is shown as a function of ΔB only.

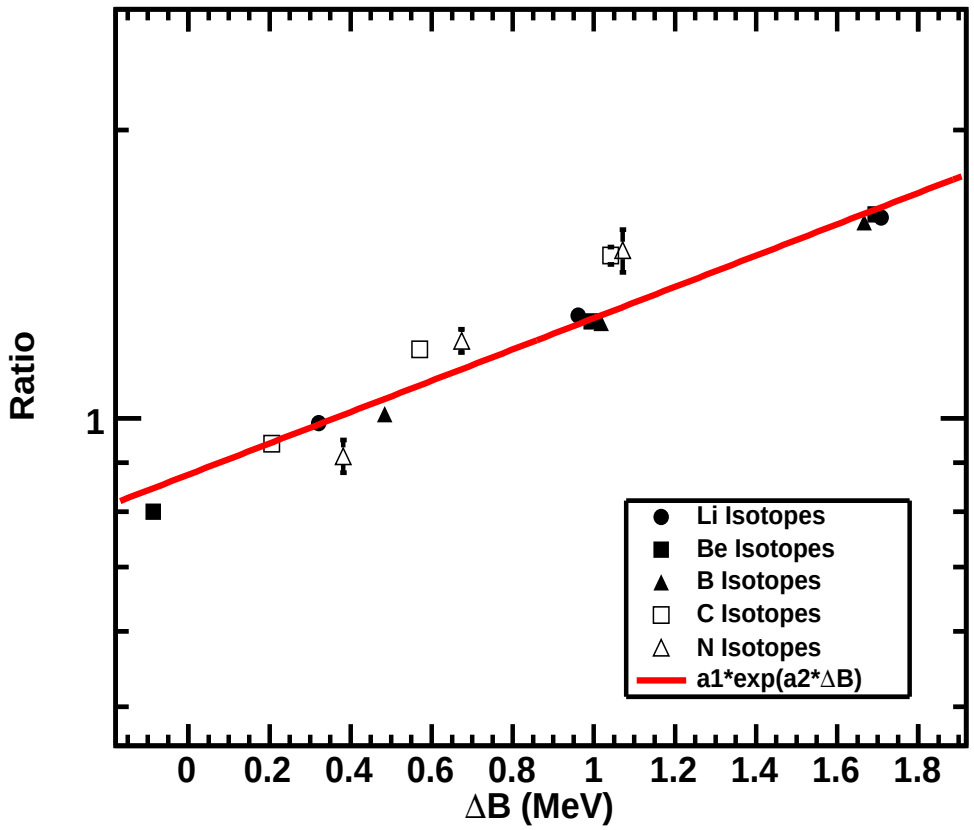

FIG. 7: Binding energy difference scaling of experimental yield ratios.

IV. SUMMARY AND CONCLUSION

We have measured the isoscaling from the projectile fragmentation of ^{48}Ca arising out of ^{48}Ca + ^{124}Sn & ^{48}Ca + ^{112}Sn reactions at 45 AMeV. Yield ratios of various isotopes ($3 \leq Z \leq 7$) were found to obey the exponential law of isoscaling. Data were subjected to the relative velocity cut, so as to ensure the origin of the events to be projectile only. The parameters of the fit α & β do not show any significant dependence on the velocity cut. No appreciable change in the parameters was observed for the fit to out of plane data, which either proves the validity of the assumption of cancellation of dynamical effects in ratios or it may also lead to an interpretation that isoscaling is not so sensitive to such effects at all. The method of scaling of yield ratios with binding energy difference was tried assuming same temperature for both the systems. The extracted values of Z & A of two nuclei shows a sizeable exchange/transfer of nucleons/cluster between the projectile and target. Even though in no way these numbers are absolute, but they still offer a unique opportunity to look at reaction dynamics in a new perspective. Clearly, before moving to correlate the isoscaling parameters to symmetry energy term and equation of state (EOS), we need to answer the basic question of the exact source and temperature of the decaying system and present study is first step toward those answers.

Evidence for An Impact Parameter Dependence of Dynamical Intermediate-Mass Fragment Formation in Reactions of Ca+Sn at 45 AMeV

M.J. Quinlan,[1] I. Pawełczak,[1] H. Singh,[1] J. Tõke,[1] W.U. Schröder,[1] F. Amorini,[2] A. Anzalone,[2] L. Auditore,[3] G. Cardella,[4] S. Cavallaro,[5] M.B. Chatterjee,[6] E. De Filippo,[4] E. Geraci,[5] A. Grzeszczuk,[7] P. Guazzoni,[8] E. La Guidara,[9] G. Lanzalone,[10] S. Lo Nigro,[5] D. Loria,[3] C. Maiolino,[2] A. Pagano,[4] M. Papa,[4] S. Pirrone,[4] G. Politi,[5] F. Porto,[11] F. Rizzo,[11] P. Russotto,[11] A. Trifiró,[3] M. Trimarchí,[3] G. Verde,[4] M. Vigilante,[12] and L. Zetta[8]

[1]*Departments of Chemistry and Physics University of Rochester, Rochester NY*

[2]*INFN Laboratori Nazionali del Sud, Catania, Italy*

[3]*INFN gruppo coll. Di Messina & Dipartimento di Fisica Universitá di Messina*

[4]*INFN Sezione di Catania*

[5]*INFN Sezione di Catania & Dipartimento di Fisica e Astronomia Universitıa di Catania*

[6]*Saha Institute for Nuclear Physics, Kolkata, India*

[7]*Institut of Physics, University of Silesia, Katowice, Poland*

[8]*INFN Sezione di Milano & Dipartimento di Fisica Universitá di Milano*

[9]*INFN Sezione di Catania & CSFNSM, Catania, Italy*

[10]*INFN Laboratori Nazionali del Sud, Catania,*
Italy & Universitá KORE Enna, Italy

[11]*INFN Laboratori Nazionali del Sud, Catania,*
Italy & Dipartimento di Fisica e Astronomia Universitıa di Catania

[12]*INFN Sezione di Napoli & Dipartimento di Fisica Universitá Federico II di Napoli*

Abstract

Charged products produced in the reaction of ^{48}Ca+^{124}Sn at 45 AMeV were measured in an exclusive study with the 4π multi-detector array CHIMERA. A number of products were found to originate from the split of the projectile-like primary reaction product (PLF). A significant fraction of these splits show characteristics inconsistent with the fission of an equilibrated PLF. An asymmetric angular distribution of PLF fission-like fragments is observed. The shape of this distribution indicates that the PLF "fission" axis is often aligned with the TLF-PLF separation axis. The relative velocity between the PLF daughters is higher than expected from Coulomb driven division of an isolated PLF. The fragment size and velocity hierarchy was also found to be sensitive to the total multiplicity of charged particles, a variable canonically associated with the impact parameter of a heavy-ion collision. Furthermore, a novel analysis scheme suggests that the data are well reproduced by a simple geometric reaction model which directly relates the asymmetry of the PLF split and the velocity hierarchy to the impact parameter of the collision.

PACS numbers: 25.70.Pq,25.70.Mn

INTRODUCTION

At medium bombarding energies (25-100 AMeV) collisions of heavy ions have been found to produce an unexpectedly high yield of fragments with atomic numbers $3 \leq Z \leq 10$, termed intermediate-mass fragments (IMFs). In peripheral collisions these IMFs join other reaction products, principally the residues of the excited projectile-like (PLF) and target-like (TLF) fragments; the fragments are so named for their genial relation to the original projectile and target nuclei. Neutrons and light-charged particles (LCP) make up the remainder of the reaction products.

The high probability of producing IMFs in medium energy heavy ion reactions has been difficult to explain using models originally developed for a lower bombarding energy range extending from near the Coulomb barrier up to 10 AMeV[1]. These models rely on the assumption that the primary nuclei, namely the projectile-like and target-like fragments, are internally equilibrated (meta-stable) and decay with little regard for their history of formation; rather the probability of decay is dependent, in a statistical fashion on the available phase space[2–5]. However, for such a model to be useful for understanding the IMF yield in higher energy collisions, the decaying nuclei must be equilibrated.

Deviations from equilibrium fission of PLFs have been reported in heavy-ion collisions already at bombarding energies as low as 7 AMeV[6]. At medium bombarding energies one might expect more substantial deviations, due to the decreased interaction time between the projectile and target, the possibility of more substantial deformation and compression of the nuclear matter, and the comparatively long time necessary for thermal relaxation. In addition the higher beam energies may open the available phase space to a number of direct break-up or other non-equilibrium particle or IMF emission mechanisms[7, 8].

Over the past few years a number of studies with 4π detector arrays have reported that the division of the PLF may occur before the short lived complex attains meta-stable equilibrium. In particular, studies of peripheral collisions have suggested that IMFs may be produced as early as 40-80 fm/c after the projectile-like and target-like fragments re-separate in a process thought to result from the disintegration of a quasi neck[9]. Intermediate-mass fragments produced on the order of 120 fm/c after the PLF and TLF separate are likely formed through a process similar to fission of these primary reaction products. However, a number of deviations from "equilibrium" systematics have been reported which has justified

the terminology "dynamical fission"[10]. In addition, a "hierarchy" relation, wherein the size of the products of the PLF split is related to their observed laboratory velocity has been reported[11]. Specifically the observations suggest that the smaller fragments formed in the asymmetric PLF split are slower than the larger fragments.

The present study demonstrates the validity of the above framework for a different set of projectile and target ions. In addition the data are compared to two well known reaction models: CLAT[12] and QMD[13]. The study then expands on this basis in an evolutionary way. The analysis identifies events in which the velocity and size hierarchy is that previously reported in the literature. These events are compared to those with the opposite ordering. It is demonstrated that the observed hierarchy is dependent on the impact parameter, or projectile-target collision centrality, using canonical relationships. In addition, a novel analysis scheme demonstrates that the relationship between asymmetry of the PLF split and the hierarchy agrees comparatively well with a simple geometric model. This model suggests that the hierarchy and asymmetry of the split is directly related to the impact parameter of the collision.

The following sections describe first the experimental details relevant to the present study. This is followed by a description of the reaction models whose predictions are compared to the data. The presentation of results begins with a discussion of the general reaction characteristics and the criterion for the selection of binary PLF splits. The impact parameter dependence of these splits is then demonstrated using kinematic correlations and independent observables within the novel analysis scheme.

ESSENTIALS OF THE EXPERIMENTAL SETUP

Heavy-ion beams of ^{48}Ca (45 AMeV) were provided by the superconducting K800 cyclotron of the Laboratori Nazionali del Sud (LNS), Catania. A beam current of 10^7 pps was bunched with a repetition rate of 120 ns. The projectiles impinged on a self supporting target of ^{124}Sn with thickness of 689 μg/cm^2. The target was placed at the operational center of the CHIMERA multi-detector array in the Ciclope scattering chamber.

The array consists of 1192 Si-CsI(Tl) detector telescopes. The silicon energy response, CsI(Tl) light output and particle time-of-flight were measured. The array has a high atomic number resolution $\Delta Z = 1$ for charged particles with energy as low as 5 AMeV. A represen-

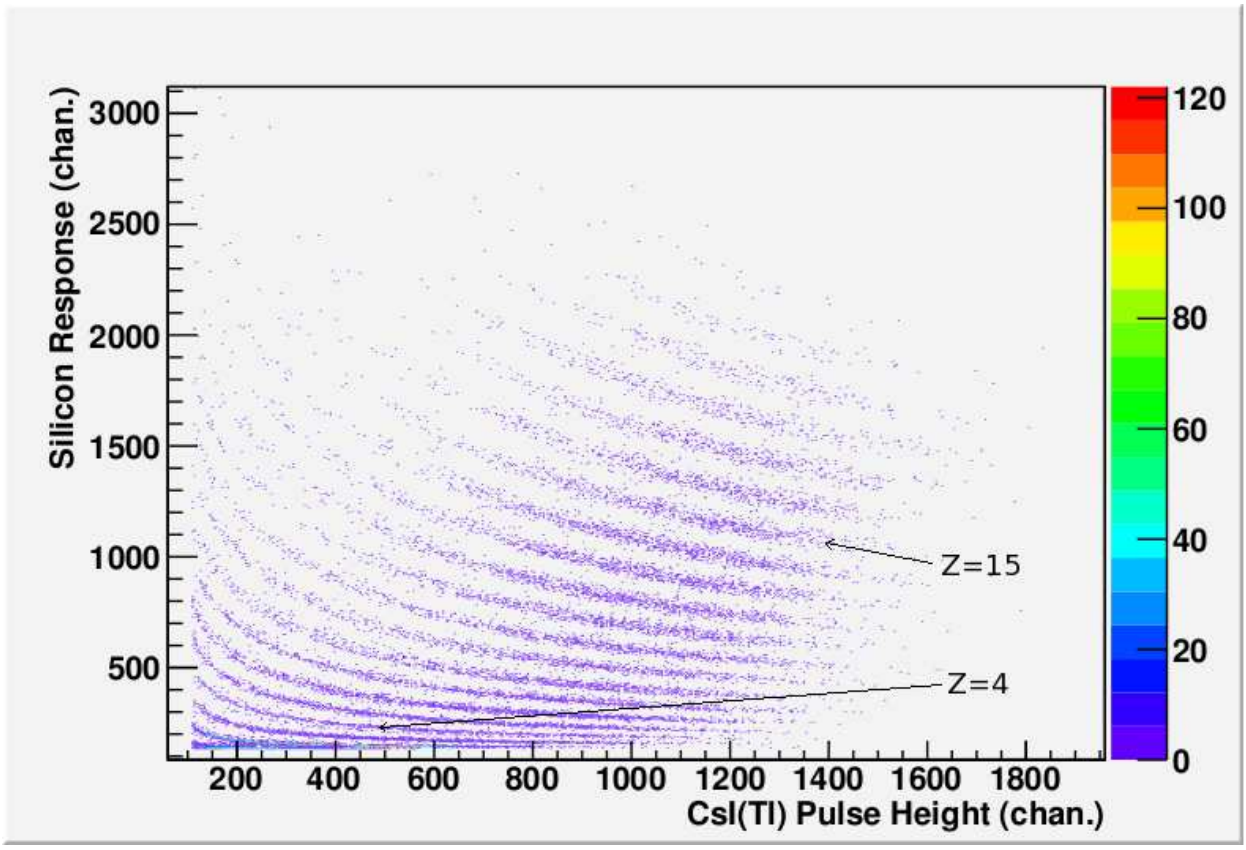

FIG. 1: (Color Online) Raw data for the ^{48}Ca+^{124}Sn reaction collected with a Si-CsI(Tl) detector-telescope placed at the laboratory angle $\Theta = 5.2°$. The two-dimensional, linear, color contours of the digitized silicon vs. CsI(Tl) response show well separated ridges for charged particles with atomic numbers ($1 \leq Z \leq 21$).

tative sample of the raw data demonstrating the atomic number resolution is shown in Fig. 1. The array provides 4π angular coverage with high granularity at forward laboratory angles ($\Theta < 30°$). This enables the detector to measure particle correlations with high efficiency.

The aim of the experiment was to perform an exclusive study of IMF production in a medium energy heavy-ion collision. Therefore, the CHIMERA array used a minimum bias trigger condition requiring the deposition of roughly 4 MeV in at least two silicon detectors within a coincidence time of 250ns. The implications of this choice are discussed in more detail later.

All analog detector signals were digitized with multi-channel charge-to-digital converters (QDC) which were enabled with a common (3 μs) gate signal. The time-of-flight of charged particles was also measured and digitally recorded using time-to-digital converters (TDC).

The maximum time-of-flight the system was configured to measure was roughly 500 ns. Given such a configuration of the electronics and the provided beam intensity, one may expect a small number of multiple reaction/elastic-scattering events to occur within the resolving time of the electronics. While generally rare, these events constitute the main component of the background for the experiment and are noted whenever visible in the data.

Identification of charged particle atomic and mass numbers was accomplished in the offline analysis. Regions corresponding to different elements (cf. Fig. 1) were identified and stored. Similar 2-dimensional correlations of CsI(Tl) detector signals allowed for atomic and mass number identification of LCPs[14]. The energy response of the silicon and CsI(Tl) detectors were calibrated using charged ions of known kinetic energy in dedicated experiments. The kinetic energy of ions with atomic number (Z>2) were inferred using the measured energy deposited in a silicon detector, the detector thickness and standard energy-loss tables[15–18]. Coupled with the measured total multiplicity (M_{tot}), the kinetic energy and atomic number information may be used to reconstruct a number of kinematic correlations among the reaction products. It should be pointed out that the detector array and acquisition electronics are also described in more detail elsewhere[19–21].

REACTION MODELS

Three reaction models of varying complexity are compared to the data. The three models all conceive a different approach to predicting the properties of the primary products of a heavy-ion reaction. In this section a brief description of each of the models is given. Included in this description are those elements of the models which are important to reproduce the results and evaluate the relevance of the basic physical process(es).

The semi-classical transport (CLAT) model was originally developed for low energy (<10 AMeV) peripheral heavy-ion collisions[12]. The simulation approximates the adiabatic response of the projectile and target along their classical trajectory. The trajectory resulting from the superposition of conservative forces is calculated using the Coulomb potential and proximity potential[22]. In the model the kinetic energy of relative motion is transferred to internal (thermal) degrees of freedom through the mechanism of nucleon exchange (NEM)[23–25]. The rate of kinetic energy dissipation is given by the one-body window and

wall formulas[26, 27]. The latter is parametrized in terms of the size of a neck connecting the projectile and target primary reaction products while they remain in physical contact. For geometrical reasons in the simulation, larger necks are formed in more central collisions allowing for more nucleon exchange. Thus for more central collisions the projectile and target experience stronger mutual nuclear attraction, and stronger dissipation of the relative kinetic energy. The simulations predict distributions for the properties of the binary (PLF,TLF) primary reaction products. These properties include the kinetic and excitation energies, the elemental and isotopic identities, as well as the mean asymptotic scattering angles and the internal angular momenta.

The quantum molecular dynamics (QMD) model was specifically developed to model higher energy heavy-ion collisions. The model calculates the phase space trajectories of the individual nucleons which make up the projectile and target. In the model the nucleons are represented by fixed width minimum wave packets. The initial configuration of the nucleons within the projectile and target nucleus are initialized by forced relaxation to a cold "ground state". Care is taken to ensure that the Pauli exclusion principle is followed, though the system is not necessarily anti-symmetric. The nucleons interact via an effective nucleon-nucleon interaction described later. Nucleus-nucleus collisions were simulated at a series of impact parameters for a total time of 1500 fm/c. At this time a search routine used the positions of the individual nucleons to determine if any complex particles existed. The mass number, atomic number, position, momentum, temperature and spin of these clusters were then determined using the position and momentum of the individual nucleons. Using these properties as input, another program predicted the asymptotic trajectories of the primary clusters and pre-equilibrium nucleons assuming a superposition of Coulomb forces. The QMD model is described in more detail elsewhere[13, 28], however a number of the parameters used to define the effective nucleon-nucleon potential used in this work are reported in Table I. The significance of the $\alpha, \beta,$ and γ parameters is described in the original publications. The significance of the latter four (a, b, D, D') are described in later publications[29, 30].

A third, simple geometric reaction model was developed. The model assumes that the PLF splits into two pieces immediately after interaction with the target. The size and longitudinal velocity of the fragments formed in the split is determined by the geometric overlap of the projectile and target nuclei as described below. To calculate the matter overlap, the

TABLE I: Parameters of the QMD nucleon-nucleon effective potential

α (MeV)	β (MeV)	γ	a (MeV fm^3)	b (MeV fm^5)	D (MeV fm^5)	D' (MeV fm^5)
-356	305.5	1.1667	450	-1560	320	158

Coulomb trajectory of the projectile at a fixed impact parameter (b) was used to estimate the distance of closest approach. The Coulomb potential for overlapping configurations was calculated assuming a uniform distribution of the nuclear charge throughout a sharp sphere of radius (R) given by the expression,

$$R = r_0 * A^{1/3} = 1.2 * A^{1/3} \tag{1}$$

In Eqn. 1, the parameter A represents the mass number of the nucleus. The fraction of the sharp sphere matter distribution of the projectile which resides within the radius of the target at the distance of closest approach was then calculated numerically. The fraction of the projectile which overlaps with the target is assumed to shear cleanly from that part of the projectile which does not overlap with the target. The overlapping matter is assumed to slow appreciably while the non-overlapping matter maintains its inertia. Thus the predictions of the geometric model are limited to the fragment sizes and the relative magnitude of their longitudinal velocity components. More advanced formulations of such a reaction model which, for example, make predictions concerning the internal excitation of the daughters of the PLF split have been proposed by others[31, 32]. The present implementation of the model neglects the effects of sequential de-excitation of the PLF daughter fragments.

The results of the dynamical interaction models CLAT and QMD were used as input for the statistical decay code GEMINI[2]. The latter code simulates the evaporation of light charged particles according to the Hauser-Feshbach formalism[33]. IMF formation is modeled in the statistical formalism by weighting with the density of states at the conditional asymmetric-fission saddle-point for each of the energetically open decay channels. The spin-dependent conditional asymmetric-fission barriers are those calculated by modifying the Sierk barriers[34] to allow an additional isotopic degree of freedom. Furthermore it assumes saddle shapes corresponding to a separation distance of d=2 fm between the centers of the nascent fragments[35]. In the model predictions presented here, the spins of the decaying nuclei were arbitrarily set to J=0.

Comparison of the model predictions to the data is facilitated by a software replica of the CHIMERA array (CSR). The CSR code corrects for the detection inefficiency resulting from missing or uncalibrated detectors. The code also requires a simulated event to have the proper characteristics required to theoretically activate the triggering electronics. Events which lack the proper characteristics are not considered for comparison to the data. In addition, the software replica also determines which individual reaction products predicted by the model(s) would be measured by the CHIMERA multi-detector, and which should be ignored. One reason for excluding an individual reaction product is that its kinetic energy is below the detection or identification threshold. The predictions of the geometric model are not checked using the CSR.

RESULTS

As a first step in the analysis, the general features of the reaction were examined. This was followed by analysis of those events found to be consistent with the division of the PLF into two relatively massive fragments. Much of the methodology for the latter analysis is based on an understanding of the general reaction characteristics. In particular kinematic regions most likely to be sampled by the fragments formed in the split of the PLF are determined and events outside these regions are not considered in the analysis.

General Reaction Characteristics

Observables sensitive to the general reaction characteristics include the charged particle multiplicity, the invariant cross sections and the PLF residue angular distributions. The absolute yields presented in this section are reported despite the fact that the precision of this measurement has not been determined. Except for the observable M_{tot} (introduced next) geometric corrections for the detection inefficiency resulting from missing or uncalibrated detectors have been made.

The normalized distribution of the total multiplicity (M_{tot}) is presented in Fig. 2. The multiplicity distribution shows a peak at small values ($M_{tot} \approx 2$), a depression at medium values, and a second, boader peak, at large values of the total multiplicity. This shape is characteristic of heavy ion reactions which span a broad range of impact parameters[6].

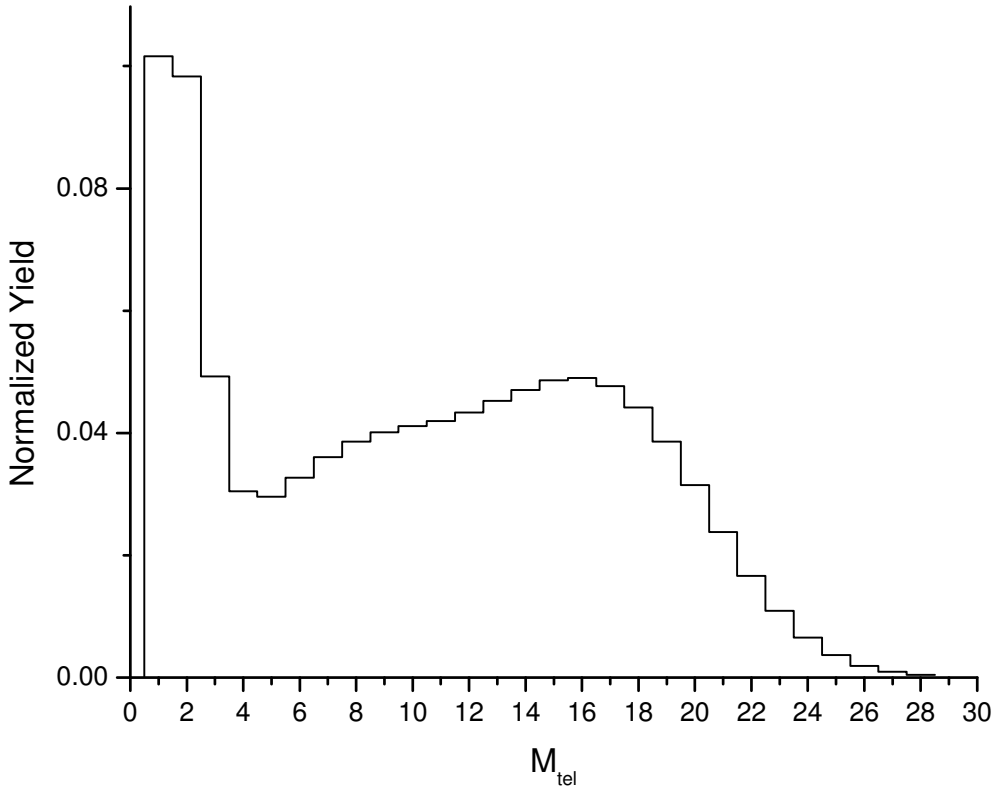

FIG. 2: Normalized total multiplicity distribution.

The measured distribution of atomic numbers of fast reaction products (products with energy sufficient to traverse the silicon detectors) is presented in Fig. 3. The yield is maximum for hydrogen, followed by a general decrease through the atomic number range $3 \leq Z \leq 10$. The yield then increases through the range $10 \leq Z \leq 19$. The sharp maximum for calcium is an experimental artifact due to elastic pile-up during the 3 μs QDC gate. The low but measurable probability of producing fragments with atomic number slightly greater than 20 reflects the fact that nucleon transfer (specifically proton transfer) occurs at the studied reaction energy. The absence of fragments with atomic number greater than $Z > 23$ reflects the fact that the slow TLF residues and fission fragments do not traverse the silicon detectors and are therefore below the Z-identification threshold.

The yield predicted by the geometric reaction model is denoted by the solid red line in Fig. 3. The model underestimates the yield of fragments with atomic numbers $Z < 10$. In

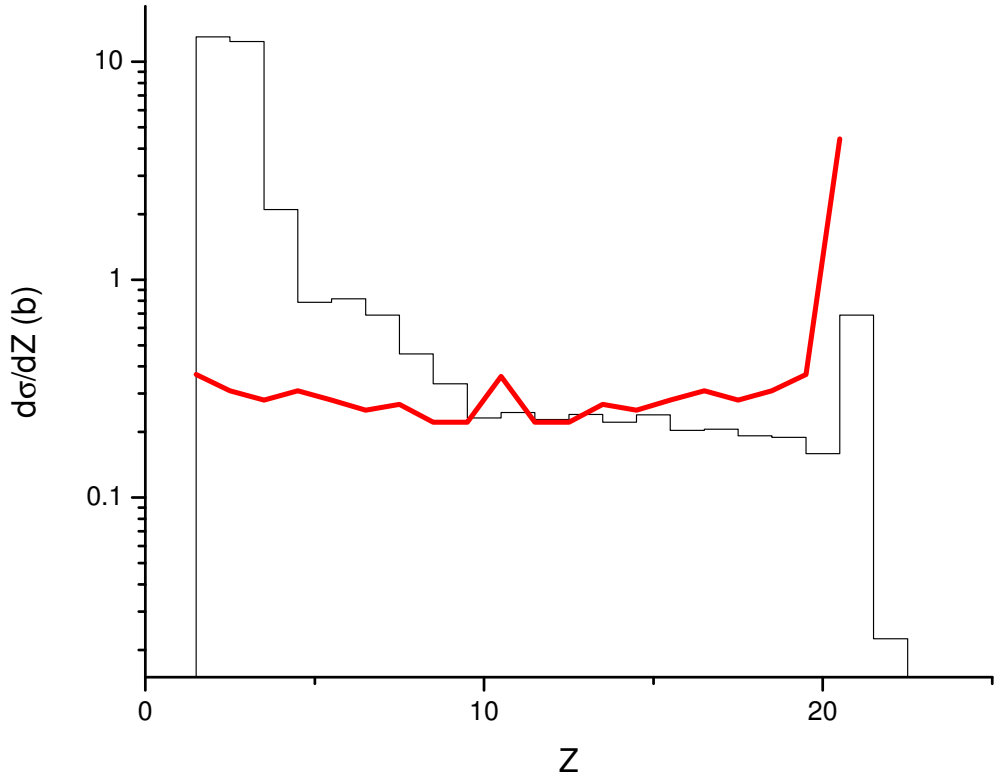

FIG. 3: The histogram represents the measured atomic number distribution $\left(\frac{d\sigma}{dZ}\right)$. The solid red line denotes the predictions of the direct production model.

the case of LCPs the underestimation is likely due to the complete neglect of sequential decay processes. However, given the simplicity of this model, the observed deviation is surprisingly small. The comparable to that found in a study of the ^{40}Ar+^{27}Al reaction at 44AMeV[36]. However, the present work uses a smaller nuclear radius parameter (r_0) and no correction for detector thresholds or particles passing through the beam exit has been made. The yield predicted for $Z = 20$ is considered arbitrary due to inclusion of some elastic scattering events in the calculation.

The invariant cross section for charged products is an observable widely used to investigate their origin. The upper panels (a)-(b) of Figs. 4-6 present the measured invariant cross section for a range of charged reaction products. Starting with products most similar to the projectile (Fig. 4(a) $18 \leq Z \leq 20$), the velocity components both parallel and perpendicular

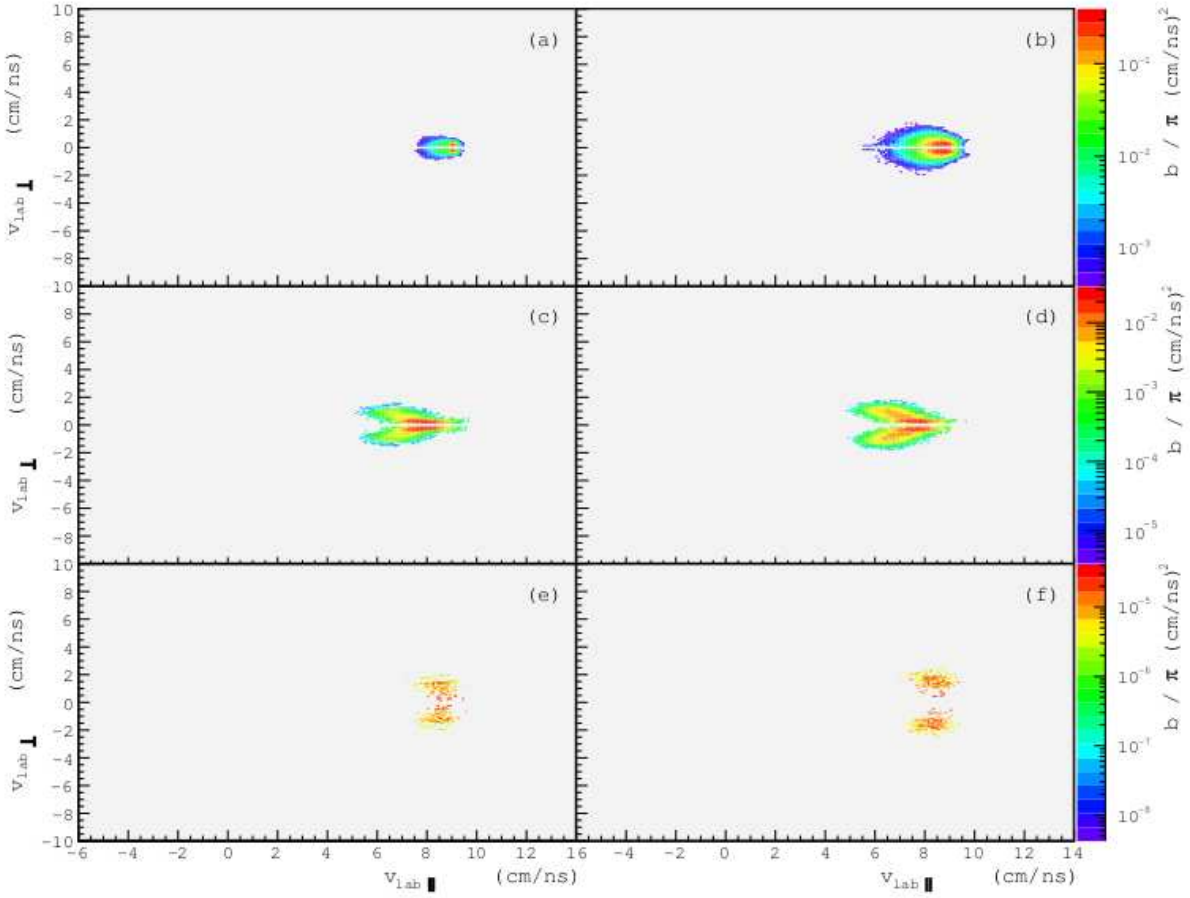

FIG. 4: Logarithmic contour plot of the invariant cross section $\left(\frac{d^2\sigma}{\pi v_\perp dv_\perp dv_\parallel}\right)$ measured for the reaction of ^{48}Ca+^{124}Sn and plotted in the laboratory frame. (a) Experimental data for charged particles with atomic numbers ($18 \leq Z \leq 20$) (b) Experimental data for charged particles with atomic numbers ($15 \leq Z \leq 17$) (c)-(d) Predictions of the CLAT+GEMINI+CSR simulations for comparison with the experimental data in the panels directly above. (e)-(f) Predictions of the QMD+GEMINI+CSR simulations for comparison with the experimental data in the same column.

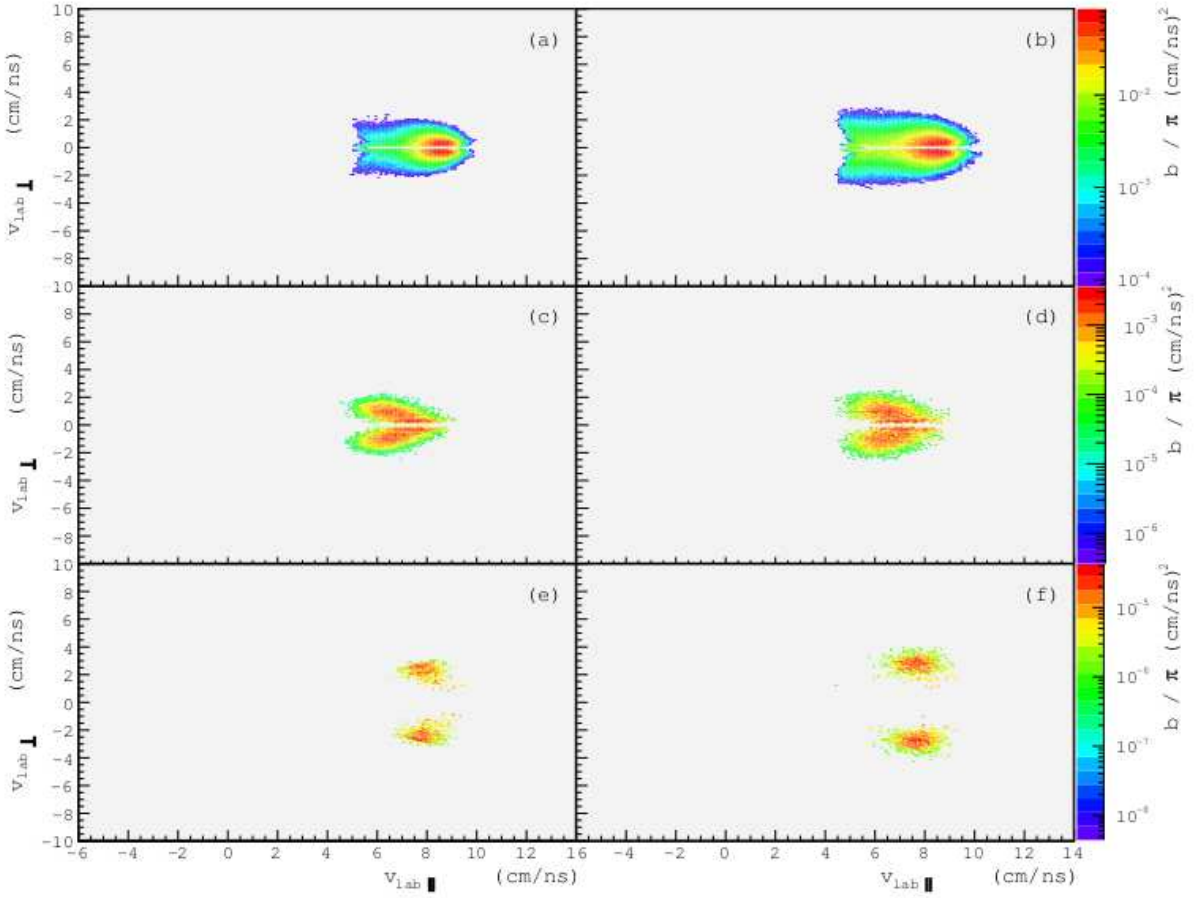

FIG. 5: Logarithmic contour plot of the invariant cross section $\left(\frac{d^2\sigma}{\pi v_\perp dv_\perp dv_\parallel}\right)$ measured for the reaction of ^{48}Ca+^{124}Sn and plotted in the laboratory frame. (a) Experimental data for charged particles with atomic numbers ($12 \leq Z \leq 14$) (b) Experimental data for charged particles with atomic numbers ($9 \leq Z \leq 11$) (c)-(d) Predictions of the CLAT+GEMINI+CSR simulations for comparison with the experimental data in the panels directly above. (e)-(f) Predictions of the QMD+GEMINI+CSR simulations for comparison with the experimental data in the same column.

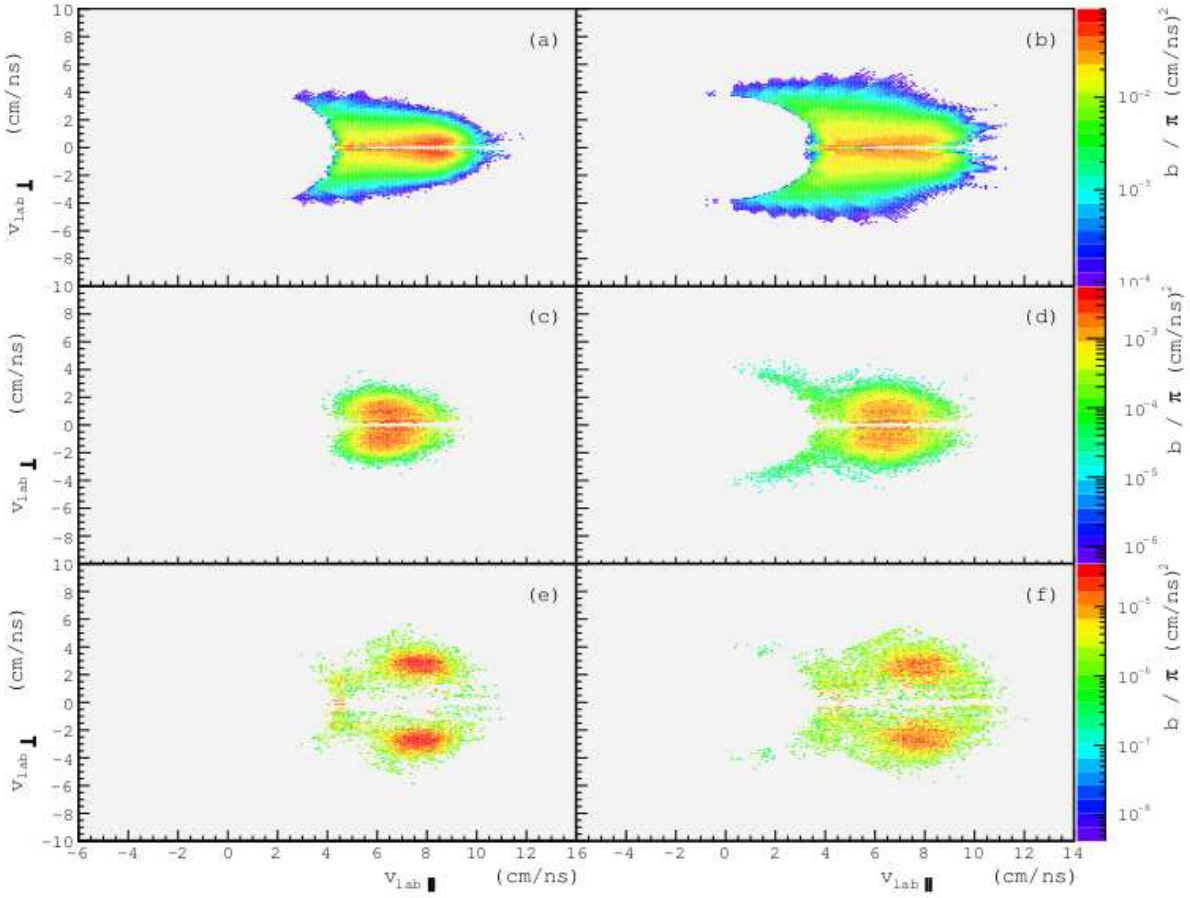

FIG. 6: Logarithmic contour plot of the invariant cross section $\left(\frac{d^2\sigma}{\pi v_\perp dv_\perp dv_\parallel}\right)$ measured for the reaction of ^{48}Ca+^{124}Sn and plotted in the laboratory frame. (a) Experimental data for charged particles with atomic numbers ($6 \leq Z \leq 8$) (b) Experimental data for charged particles with atomic numbers ($3 \leq Z \leq 5$) (c)-(d) Predictions of the CLAT+GEMINI+CSR simulations for comparison with the experimental data in the panels directly above. (e)-(f) Predictions of the QMD+GEMINI+CSR simulations for comparison with the experimental data in the same column.

to the beam axis show little deviation from the coordinates of the projectile before the reaction $(v_{\parallel}, v_{\perp}) = (9, 0)$. Fragments with smaller atomic number show larger deviations from the coordinates of the projectile. The largest change in parallel and perpendicular components produces a "comet tail" shape seen most clearly in Fig. 6 (a) and (b).

Turning to a comparison between the data and both the CLAT+GEMINI+CSR and QMD+GEMINI+CSR simulations, one immediately concludes that the models do not quantitatively agree with the data. Large portions of the observed velocity space are not sampled by the calculations and those which are sampled are not in quantitative agreement. However, some qualitative similarities are discernible. To begin the work and justify the subsequent analysis framework a comparison of the qualitative similarities will be discussed. The comparison assumes that regions of velocity space sampled by both the model and experiment indicate a common mechanism of production.

The non-circular shape visible in the experimental distributions which exhibit a "comet tail" differs from that predicted by the corresponding CLAT+GEMINI+CSR simulations presented in panels (c)-(d) of the same figures. This difference is most pronounced for fragments with atomic numbers in the range ($Z < 9$) and suggests that these fragments originate from sources not considered by the model. However, the distribution for fragments with larger atomic numbers exhibit elongated shapes (even though the internal structure is decidedly different) in both the data and the CLAT+GEMINI+CSR simulations. Therefore, the origin of the larger fragments may be similar to that predicted by the model. Fragments which lie along the semi-circular ridge with radius 2 cm/ns centered around $(v_{\parallel}, v_{\perp}) = (2, 0)$ visible in Fig. 6 (b) and (d) could share a common origin and be classified as TLF fission fragments. The sharp cut-off along the inner edge of this semi-circular ridge denotes the Z-identification threshold. It is quantitatively well reproduced by the CSR "filtering".

The predictions of the QMD+GEMINI+CSR simulations reproduce the velocity space position of the *peaks* of the experimental distributions in Figs. 4-5, but not those in Fig. 6. Instead, in the latter figure, especially panel (f), the *tails* of the experimental and model distributions have a similar shape. This suggests that the majority of the fragments with atomic numbers in the range ($Z \geq 9$) could share similar production mechanism(s). For fragments with lower atomic number, only a fraction of those predicted by the QMD+GEMINI+CSR model may share production characteristics. The shape and location of the *peak* of the distribution does not appear to depend on the range of fragment atomic numbers as predicted

by the QMD+GEMINI+CSR model. This may surprisingly suggest that the mechanism for producing fragments with atomic number $Z \approx 17$ is similar to that producing fragments $Z \approx 4$ in the model. It has been mentioned above that the same cannot be said for the data.

Binary heavy-ion reactions are known to produce two massive intermediate systems denoted the PLF and TLF for their similarity to the projectile and target respectively. We may therefore make the *ad hoc* assumption that in the ^{48}Ca+^{124}Sn reaction the residue of the PLF will have an atomic number $Z \geq 10$. Using this event selection the following figures examine characteristics of the PLF residues using well known relationships developed for the study of low energy binary dissipative collisions.

The relationship between the laboratory kinetic energy and the laboratory scattering angle of the PLF residue is known to have a characteristic dependence in binary dissipative collisions[37]. This relationship is presented as a logarithmic contour diagram in Fig. 7 (a) and (b). At small laboratory angles the data show two high intensity groupings at 2200 and 1200 MeV respectively. The first corresponds to elastic scattering events. These have already been characterized as an experimental artifact. However, consistent with expectation of elastic scattering angular distribution, the intensity of the band decreases with increasing scattering angle. The second, medium intensity band begins at small angles and approximately 1500 MeV and extends to larger angles accompanied by lower energies and lower intensities. The events contributing to this band are consistent with semi-peripheral collisions which experience some degree of "orbiting".

The data in Fig. 7(a) are compared to the mean predictions of the CLAT+GEMINI+CSR model. Open symbols represent mean predictions of the primary PLFs at different impact parameters. The lines interpolate between the points. Closed symbols represent the mean predictions of the PLF residues likely to be measured by the CHIMERA multi-detector for the same set of impact parameters. The agreement between the latter calculation and the second, medium intensity contour band is excellent. The CSR also predicts that the PLF residue will be measured after an apparent kinetic energy loss of approximately 200 MeV in reasonable agreement with the general lack of genuine $M_{trigger} \geq 2$ events with higher laboratory kinetic energies.

The data in Fig. 7(b) are compared to the mean predictions of the QMD+GEMINI+CSR model. Again, open symbols represent the predictions of the primary PLF and closed symbols represent predictions for the PLF residue kinetic energy and laboratory scattering

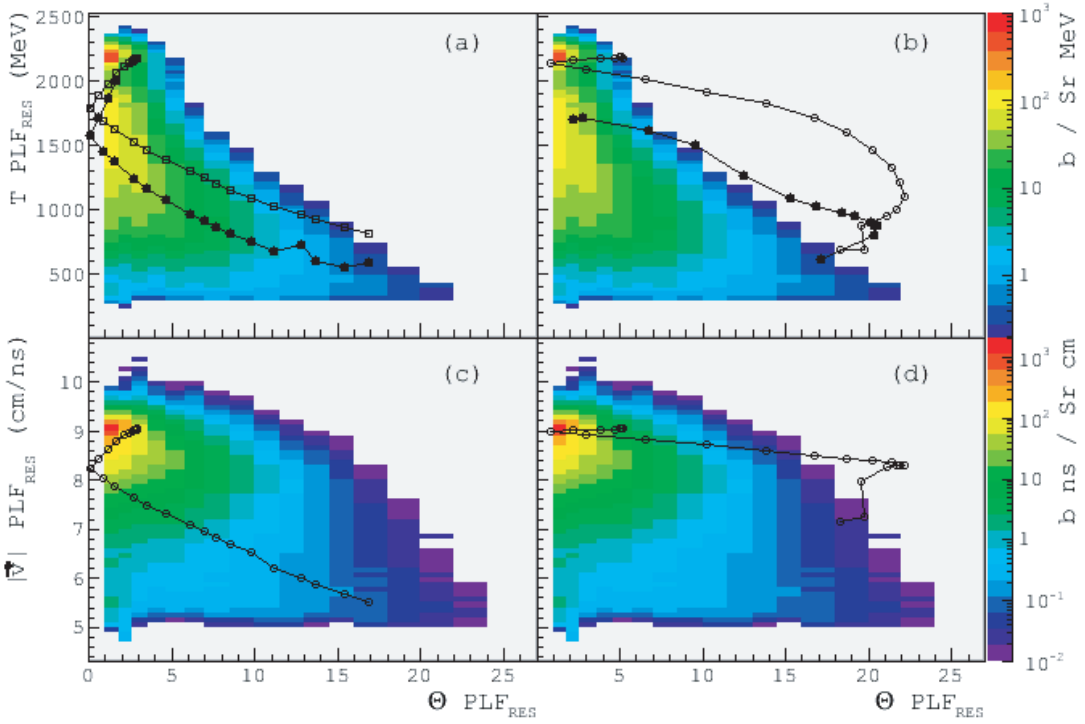

FIG. 7: Contour plots of the double-differential cross sections for PLF residues from the ^{48}Ca+^{124}Sn reaction. The top panels (a) and (b) illustrate the yield as a function of PLF residue kinetic energy and deflection angle, while the bottom panels (c) and (d) represent this yield as a function of PLF residue velocity and deflection angle. Symbols represent results of model calculations based on the code CLAT (left panels) and the QMD code (right panels) for primary (open symbols) and secondary (solid symbols) PLF reaction products. In the bottom panels predictions for primary and secondary fragments coincide. The lines are drawn to guide the eye.

angles at different impact parameters. However, the impact parameters are not the same as those representing the CLAT model predictions. The QMD model predicts kinetic energies of the PLF residue which are higher than observed experimentally.

The relationship between the PLF residue velocity and the laboratory scattering angle is also known to have a characteristic dependence similar to that for the PLF residue kinetic energy. In addition, this relationship is known to be independent of statistical decay processes. Therefore, the data are only compared to predictions of the primary reaction products in Fig. 7 (c) and (d). The data show a wide distribution of laboratory velocities and lack the branch structure visible in the kinetic energy, laboratory angle relationships. The inensity is peaked at small angles and laboratory velocities close to 9 cm/ns. The intensity decreases as the angle increases. The CLAT model predictions presented in Fig. 7(c) overestimate the change in velocity with angle. This suggests that the predictions for the kinetic energy and laboratory angle relationship may be accidental. The QMD model predictions presented in Fig. 7(d) underestimate the change in velocity with angle. This underestimate may explain the discrepancy discussed above regarding the kinetic energy loss.

The picture emerging from the data analysis is that a number of features of low energy damped reactions remain at 45 AMeV. However a number of important deviations have been observed. It is clear that large remnants of the projectile survive the collision even in semi-peripheral collisions. The next section will examine events in which the PLF apparently breaks into two pieces and produces an IMF.

Coincidence Event Data and PLF Binary Splits

The primary advantage of 4π detector arrays is their ability to measure the kinematic relationships between multiple reaction products produced in a single heavy-ion collision. A secondary benefit, is that the reaction products may be detected with high efficiency. Before turning to a discussion of events consistent with the binary split of the PLF, the coincidence data concerning the multiplicity of LCPs will be examined.

The average multiplicity of identified LCPs detected in coincidence with a PLF residue is plotted versus the laboratory scattering angle of the residue in Fig. 8. The y-axis scale increases from top to bottom to mimic the patern expected in the PLF residue energy and velocity dependence on the laboratory scattering angle. The multiplicity is observed to increase with increasing scattering angle of the PLF residue. The rate ($d\mathrm{M_{LCP}}/d\Theta\mathrm{PLF_{res}}$) of this increase is largest for PLF residue angles in the range $5 < \Theta < 15$. At larger angles the multiplicity does not increase as quickly, suggesting some degree of saturation

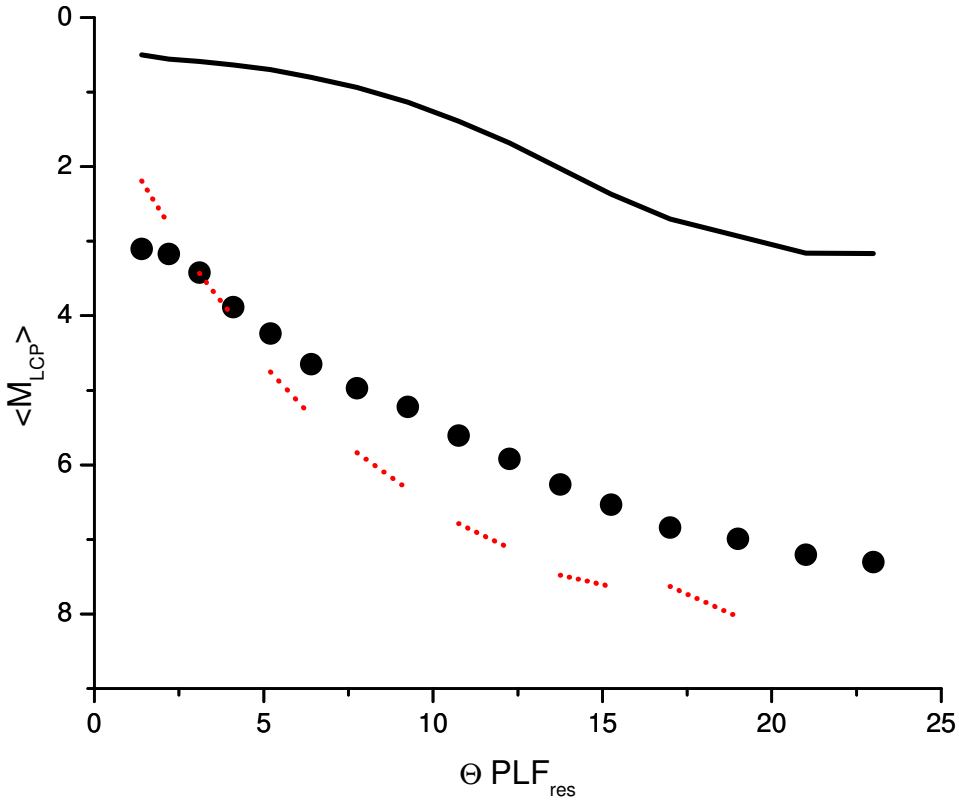

FIG. 8: The correlation between the average multiplicity of LCPs and the PLF residue scattering angle in the ^{48}Ca+^{124}Sn reaction. Experimental data are represented by solid dots while the model predictions are represented by solid (QMD-based) and dotted (CLAT-based) lines.

may occur. The data are compared to CLAT+GEMINI+CSR predictions (dashed line) and QMD+GEMINI+CSR predictions (solid line). Quantitatively, the former slightly overestimates the multiplicity dependence on the PLF residue angle while the later severely underestimates it. Both models reproduce the observed trend of increasing multiplicity with increasing PLF residue scattering angle.

Events in which two massive fragments ($Z > 2$) were detected in coincidence were examined. As stated above, the existence of a "hierarchy" relationship between the speed and size of the PLF fission fragments has been reported. Therefore in the following analysis, the two fragments were classified according to their size; wherein the fragment with larger atomic number was denoted Z_H for "heavy" and the fragment with the smaller atomic number was

denoted Z_L for "light".

The invariant cross section for these two fragments is displayed in Fig. 9 (a) and (b). The predictions of the CLAT+GEMINI+CSR model for comparable events are presented for comparison in Fig. 9 (c) and (d). The solid lines demarcate a cone of forward laboratory angles ($\Theta < 18°$). The significance of these lines will be explained next.

The fragments contributing to the semi-circular ridges visible in Fig. 9 (b) and (d) were previously associated with the progeny of the target. If this is true it would be inappropriate to consider these Z_L fragments in the analysis specifically designed to examine the kinematic relations between fragments formed in the split of an isolated PLF. Thus an *ad hoc* selection of events in which both the Z_H and Z_L fragments were detected within the forward $\Theta < 18°$ cone was assumed. The use of such an arbitrary selection must be carefully considered and merits further discussion. The forward 18° cone does appear to effectively separate contributions from the PLF and TLF as they are modeled by the CLAT+GEMINI+CSR simulations. One may therefore view the selection as a viable tool to study events which are consistent with asymmetric fission of equilibrated PLFs and those which deviate slightly from this idealization. Also, the results presented below are qualitatively insensitive to a 20% change in the value of the cut-off angle.

The result of this selection was also tested by determining the total atomic number detected on an event-by-event basis within this kinematic region. The distribution of total atomic number within the forward ($\Theta < 18°$) region is presented in Fig. 10. If all protons from the projectile were collected, one may expect a distribution centered close to the atomic number ($Z = 20$). The Gaussian shaped distribution is centered at a value of fifteen. The shift is likely due to stochastic processes such as incomplete collection of multiple PLF fragmentation products, a shift in the primary PLF atomic number distribution during the projectile-target interaction, or a combination of the two. Especially important to the subsequent analysis is the complete collection of massive fragments ($Z > 2$) whose relatively large momenta may significantly affect the kinematic reconstruction of the PLF breakup.

Just as it would be inappropriate to consider fragments originating from the TLF, so to would it be inappropriate to analyze incomplete events. To this end a simple Monte-Carlo simulation was developed. The simulation considered a simplified case in which a PLF with atomic number $Z = 20$ and velocity vector components $(v_\parallel, v_\perp) = (8, 0)$ splits into three massive fragments in a process consistent with fission of an equilibrated PLF. The simulation

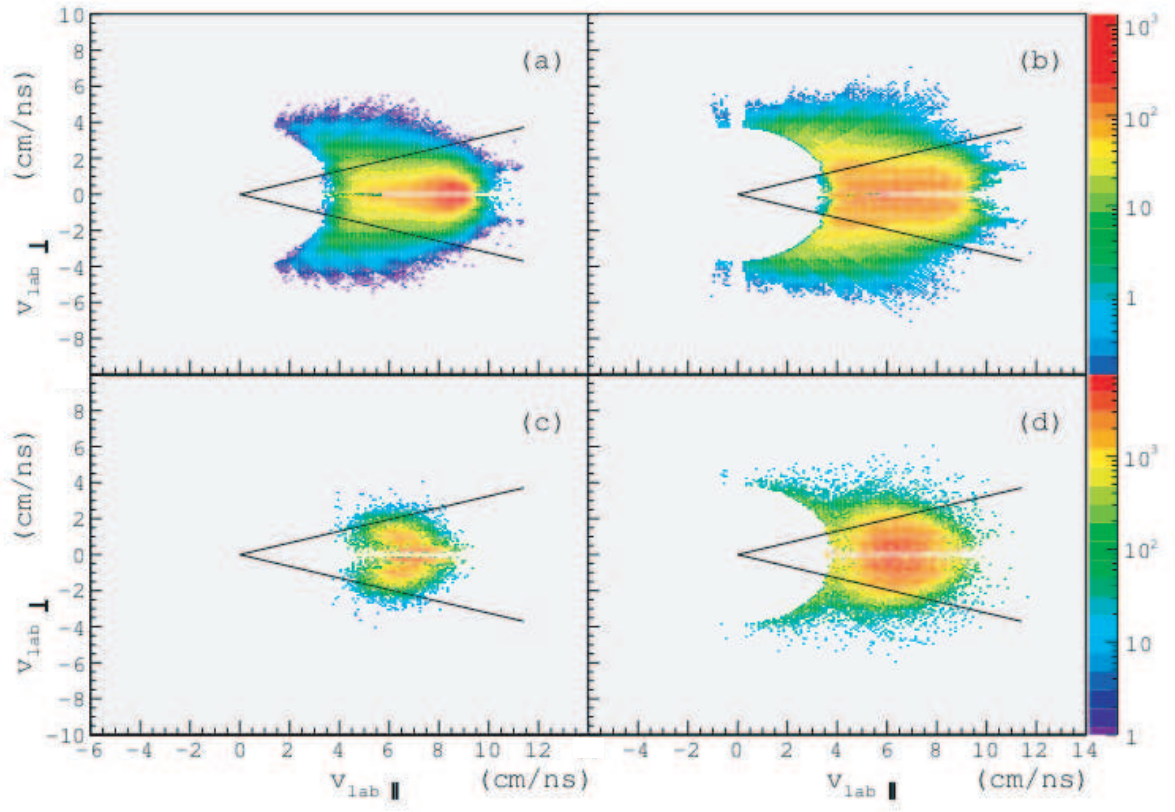

FIG. 9: (a) Logarithmic contours of the invariant cross section (arb. units) for charged particles with larger atomic number (Z_H) detected in two-body events plotted in the laboratory. (b) Logarithmic contours of the invariant cross section (arb. units) for charged particles with smaller atomic number (Z_L) detected in two-body events plotted in the laboratory. (c)-(d) CLAT+GEMINI+CSR model predictions for the invariant cross section of the heavy (left panel) and lighter (right panel) fragments produced in the binary split of the PLF.

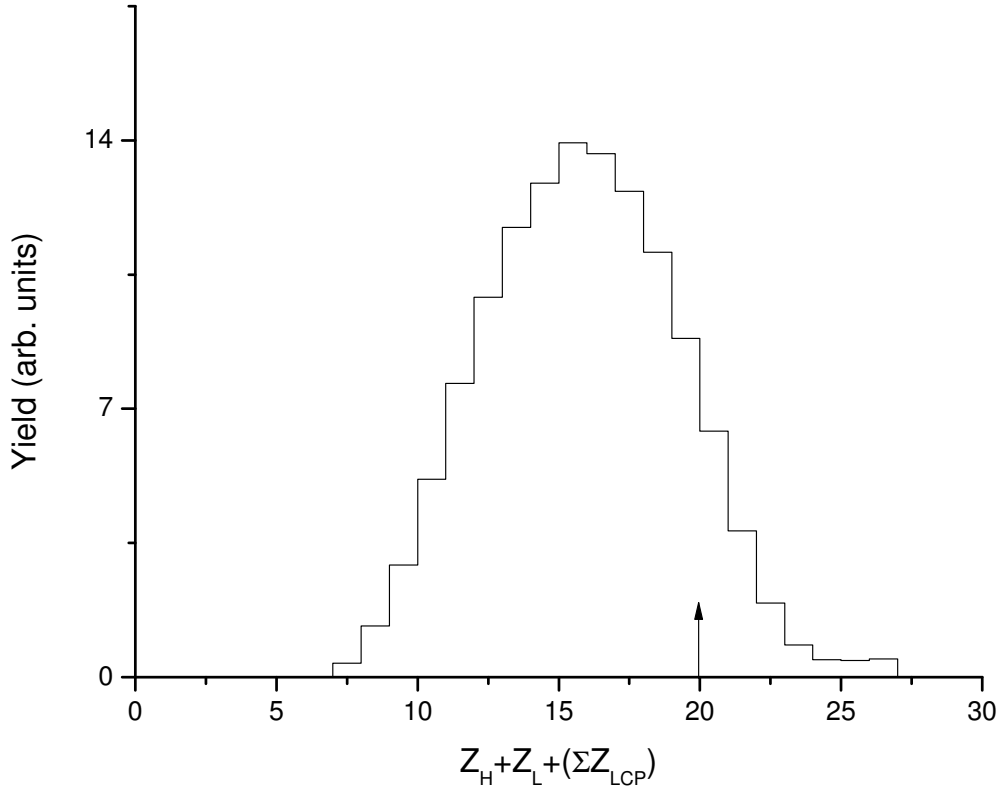

FIG. 10: Distribution of total atomic number identified in the forward 18 degrees of the laboratory in two-body PLF splits

calculated the probability that the fragments were measured by determining if they struck a calibrated detector. The percent of three fragment PLF splits misidentified as two fragment splits for such an idealized situation, is approximately 10%. However, the measured yield of three fragment PLF splits is a factor of six less than that measured for two fragment splits. This suggests that the percent of incorrectly identified events is less than 10%. Therefore the Monte-Carlo simulations suggest that the shift in the summed atomic number distribution is not due to missing massive fragments and a kinematic reconstruction of binary PLF splits is possible.

Turning to this kinematic analysis, an important variable in the study of PLF fission systematics is the angle between the fission axis and the direction of the PLF motion. This relationship is illustrated in Fig. 11 where moving from bottom to top in the figure,

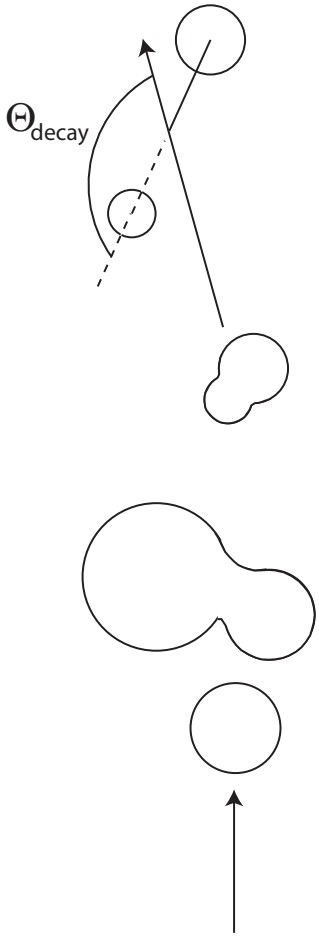

FIG. 11: Definition of the decay angle (Θ_{decay}) deduced from the vector components of the reaction products produced in the binary split of the PLF.

the projectile and its progeny are followed through the course of the heavy-ion reaction. First, the projectile approaches the target. Next, a di-nuclear complex is formed. Then, the excited and possibly deformed PLF separates from the TLF following an "orbiting" trajectory. Finally, the PLF breaks into two pieces. The original direction of the PLF before the split can be reconstructed using the properties of the measured fission fragments and the relationship presented in Eqn. 2. In the equation, A_H & A_L are the mass numbers of the "heavy" and "light" fragments respectively and the indicies represent the same relationship for the velocity vectors $\bar{\mathbf{v}}_H$ & $\bar{\mathbf{v}}_L$.

$$\bar{\mathbf{v}}_{PLF} = \frac{A_H\bar{\mathbf{v}}_H + A_L\bar{\mathbf{v}}_L}{A_H + A_L} \tag{2}$$

At any time during the course of the reaction, light charged particles may be emitted.

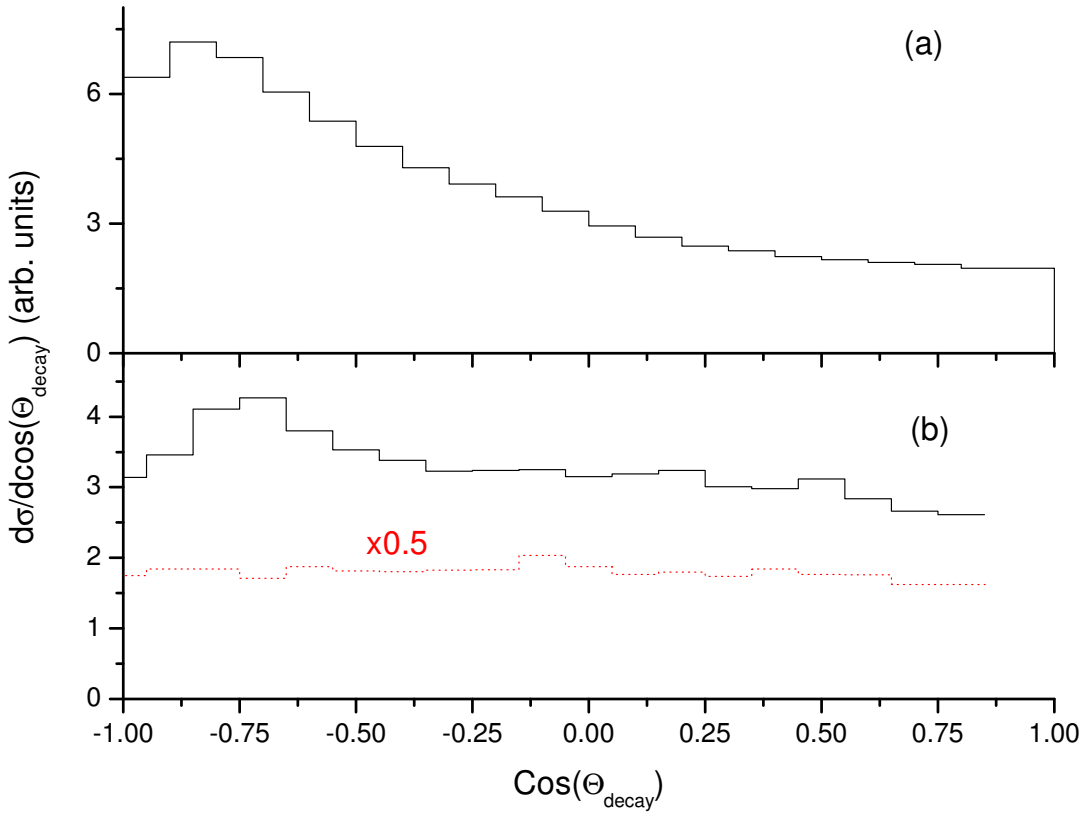

FIG. 12: Measured differential cross section (arb. units) versus the cosine of the decay angle for all two-body events. (a) Experimental data from the ^{48}Ca+^{124}Sn reaction (b) The solid black line presents the CLAT+GEMINI+CSR model predictions of the ^{48}Ca+^{124}Sn and the dotted red line represents the model calculation considering *only* the decay of the excited PLF.

However, their contribution to the kinematic reconstruction is assumed to be negligible. The angle between the fission axis and the original motion of the PLF is well understood for cases in which the PLF is equilibrated[38]. For such nuclei, the angular distribution is symmetric about $cos(\Theta_{decay}) = 0$.

The angular distribution observed when the analysis is performed for all events in which two massive fragments (Z_H & Z_L) were detected is presented in Fig. 12(a). The distribution is peaked at $cos(\Theta_{decay}) = -0.85$. The angular distribution predicted by the the CLAT+GEMINI+CSR model is presented in Fig. 12(b) as a solid black line. The location of the peak in the simulated distribution is in qualitative agreement with that visible in the

data. Also presented for comparison in Fig. 12(b) as a dotted red histogram is the result of the CLAT+GEMINI+CSR calculation considering only contributions from the decay of the PLF. Such a separation is obviously only possible in a simulation. The latter distribution lacks a peak, which suggests that this component may be associated with the progeny of the TLF in the experimental data. One must point out that the difference in the height of the peak to tail component in the data is approximately four times that observed in the simulation. Therefore, one cannot exclude other dynamic decay contribution(s) from either the PLF or TLF.

The angular distribution of binary PLF splits detected in the forward 18° of the CHIMERA array may offer a better experimental rejection of TLF contributions. The angular distribution which results from this event selection is presented in Fig. 13 as solid symbols. The data are not symmetric about $cos(\Theta_{decay}) = 0$. However, the CLAT+GEMINI+CSR model predictions, which considers both PLF and TLF sources, is presented as a solid red line in the same figure. The simulated distribution is symmetric and therefore suggests that the event selection does not appear to contain significant contributions from the TLF. This also suggests that the experimentally observed asymmetry is not an experimental artifact. The data are peaked at angles $cos(\Theta_{decay}) = -1$ which are consistent with the "aligned" break-up of the PLF along its direction of flight and in a configuration in which the smaller fragment (Z_L) is slower than the larger one (Z_H). This ordering relationship has been termed the "hierarchy effect".

In addition to symmetric angular distributions, the relative velocity of the fragments produced in the fission of equilibrated PLFs has been known to follow "Viola" systematics[39]. These systematics relate the size of the fissioning system to the total kinetic energy imparted to the fission fragments. The systematics have been expanded to relate the size of both fragments to the total kinetic energy released in asymmetric splits[40]. However, these systematics are not valid for systems as small the the Ca-like PLF produced in the present study. Instead, the present work assumes the kinetic energy is equal to the potential energy (U_c) of two "touching" uniformly charged spheres. The radii of the spheres is assumed to be that of the final fragments and is estimated using the standard relationship between the nuclear mass and matter radius (see Eqn. 1). The expression for the potential energy in

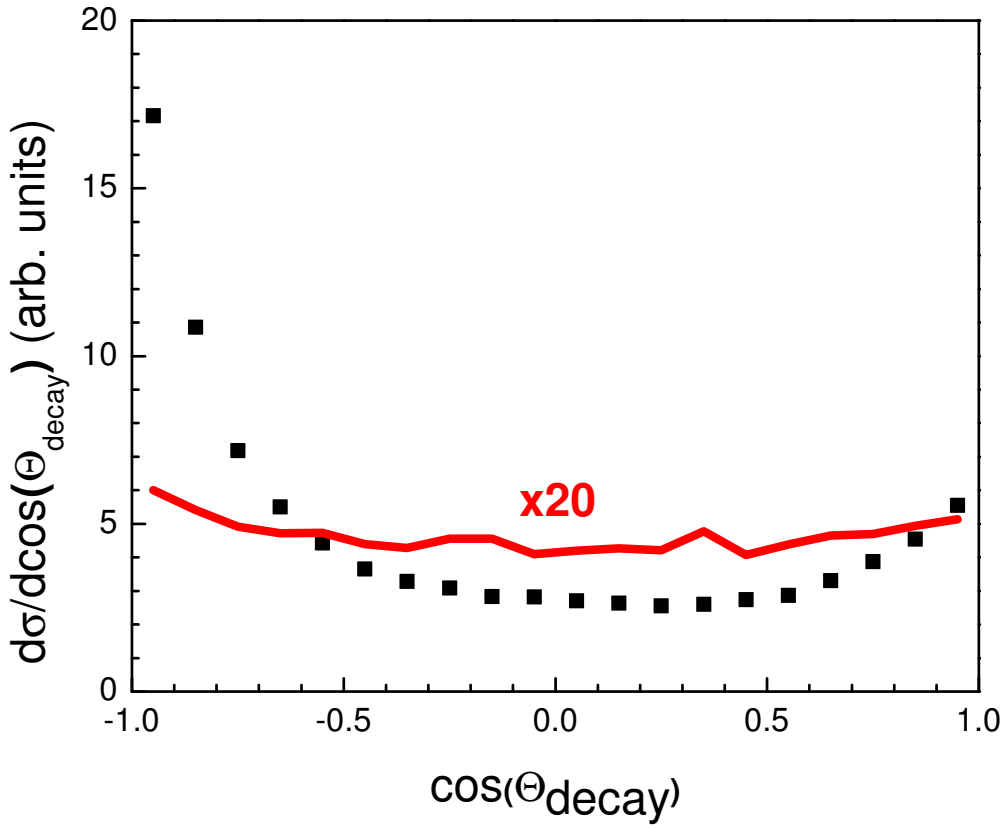

FIG. 13: Differential cross section (arb. units) versus the cosine of the decay angle for two-body events in which both fragments (Z_H & Z_L) were detected within the forward 18° cone. Solid symbols represent the data measured for the ^{48}Ca+^{124}Sn reaction. The cross section predicted by the CLAT+GEMINI+CSR model is represented by a solid line. The model predictions have been increased by a factor of twenty to allow a better comparison of the shape of the angular distributions.

MeV for such a configuration may be expressed as,

$$U_c = \frac{1.44 * Z_H * Z_L}{1.2 * \left(A_H^{1/3} + A_L^{1/3}\right)}. \tag{3}$$

After estimating the total kinetic energy of the fission fragments, their relative velocity (V_c) may be calculated using the principle of momentum conservation.

Next, the analysis investigated whether the measured relative velocity between the PLF fission fragments is consistent with the above systematics. The observed relative velocity is

defined by the relation,

$$\bar{\mathbf{v}}_{\mathrm{Rel}} = \bar{\mathbf{v}}_{\mathrm{H}} - \bar{\mathbf{v}}_{\mathrm{L}}. \tag{4}$$

The logarithmic contours in Fig. 14(a) represent the double differential cross section for PLF splits in the forward cone of the CHIMERA array as a function of the cosine of the decay angle and the normalized relative velocity $\frac{\bar{\mathbf{v}}_{\mathrm{Rel}}}{V_c}$. For a large fraction of the observed PLF splits the relative velocity is significantly larger than that expected ($\frac{\bar{\mathbf{v}}_{\mathrm{Rel}}}{V_c} = 1$) of touching spherical nuclei. The velocity is especially high for decay angles $cos(\Theta_{decay}) = -1$ and $cos(\Theta_{decay}) = 1$. In the latter case, the smaller fragment Z_L is faster than the larger one Z_H. This order is the opposite of that described by the "hierarchy effect". The logarithmic contours in Fig. 14(b) represent the double differential cross section predicted by the CLAT+GEMINI+CSR model. The predicted events display a symmetric angular distribution as demonstrated previously and the normalized velocity is centered around a value of one. The model predictions are consistent with systematics of asymmetric fission of equlibrated PLFs but clearly deviate from the observations.

One natural explanation for the observations of both the classical hierarchy and its opposite, is that the PLF splits into two pieces directly (or soon after the projectile interacts with the target). This scenario is consistent with the geometric reaction model described above. If such a model were to successfully describe the data, one would expect a direct relationship between the impact parameter and the PLF splits with high relative velocity between the fragments. Before comparison with the geometric model the data were examined to see if a variable independent of the kinematic reconstruction of the PLF was sensitive to the collision centrality. One observable canonically associated with the collision centrality is the multiplicity of charged particles and its sensitivity has been demonstrated for semi-peripheral collisions (c.f. Fig. 8). The following will use this observable to independently characterize the data presented in Fig. 14(a).

The data which deviate from the systematics developed for fission of equilibrated nuclei appear to fall into two classes. The first class corresponds to PLF splits in which the smaller fragment Z_L is slower than the larger fragment Z_H. This particular ordering of the size and speed of the fragments for this class of events is consistent with the "hierarchy effect". The class may be selected by the criterion $cos(\Theta_{decay}) < -0.6$ and is labeled the "backward" split of the PLF because the smaller fragment is found in the backward kinematic region of the PLF center-of-mass frame. A second class of events is consistent with the opposite ordering

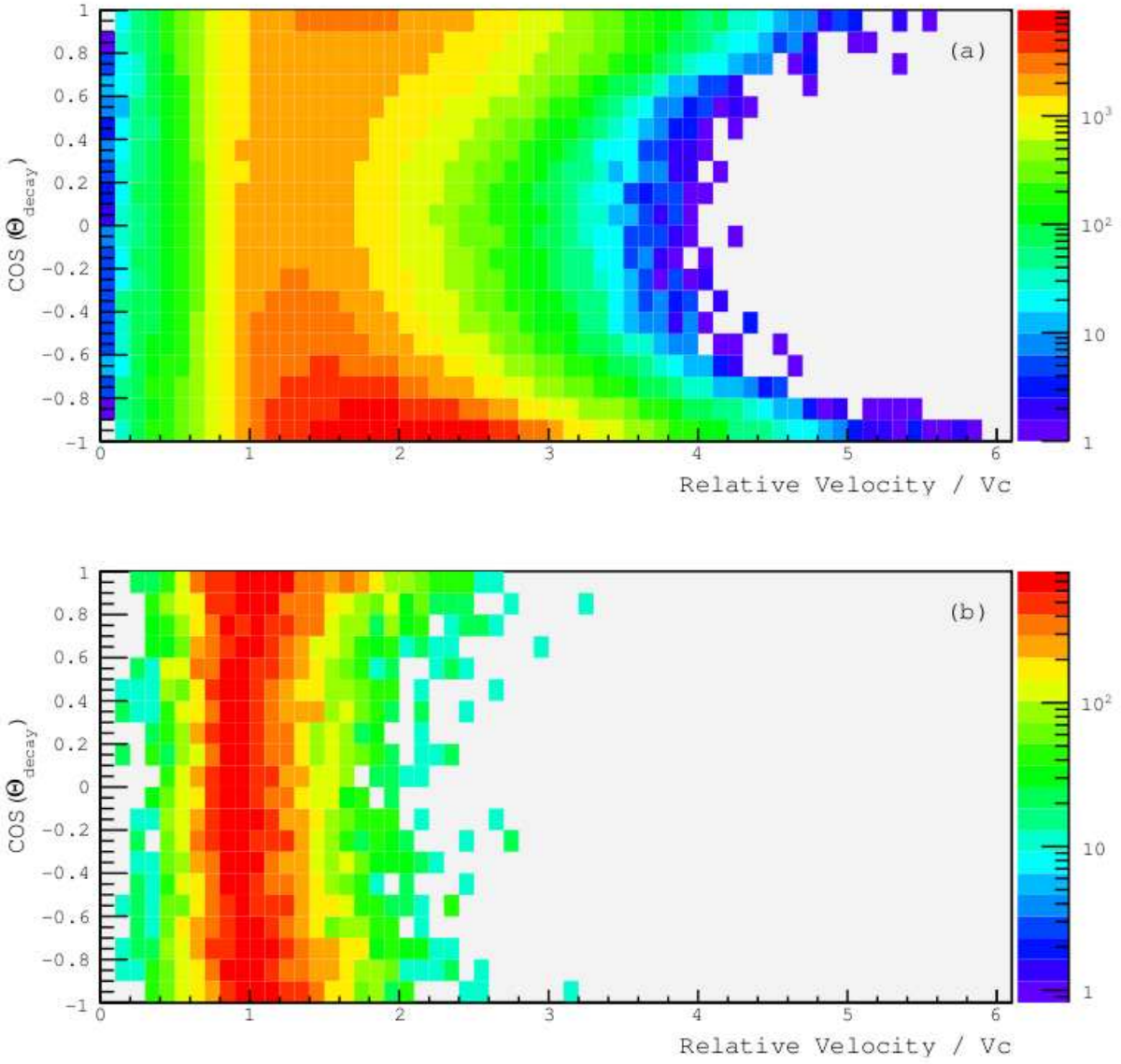

FIG. 14: Logarithmic contours of the cross-section (arb. units) for two-body events plotted versus $cos(\Theta_{decay})$ and the relative velocity between the fragments divided by that expected for fission of an equilibrated PLF (V_c). (a) Experimental data measured for the ^{48}Ca+^{124}Sn reaction. (b) CLAT+GEMINI+CSR model predictions for the same reaction.

of fragment speeds and sizes. These events may be selected by the criterion $cos(\Theta_{decay}) > 0.6$ and is labeled the "forward" split of the PLF. To ensure that the orientation is properly defined one may impose a further condition on the asymmetry (η) of the PLF split. The

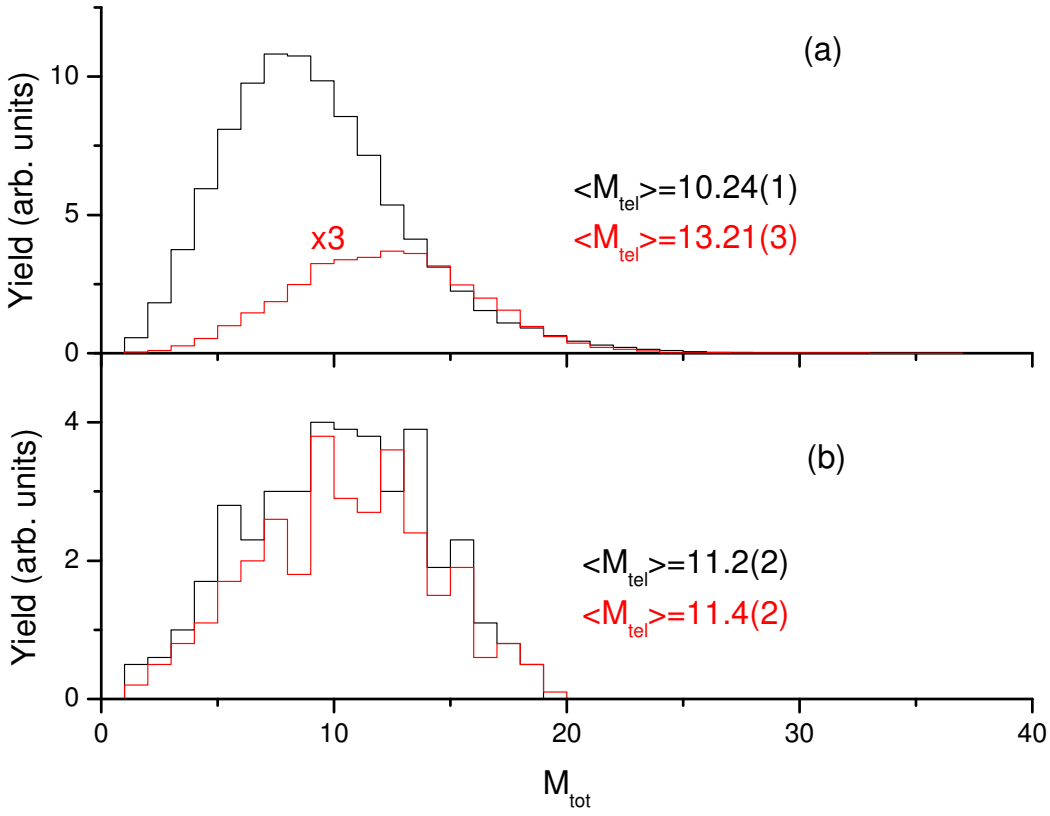

FIG. 15: (a) Experimental total multiplicity distribution for two classes of events: forward (red) and backward (black) asymmetric ($\eta > 0.5$) splits of the PLF. The multiplicity distribution for forward splits has been scaled by a factor of three to allow better comparison. (b) CLAT+GEMINI model predictions for the multiplicity of charged particles with laboratory velocity greater than 3 cm/ns for the two classes of PLF splits. The mean and error in the mean are listed in the figure with color coded text to coincide with that of the respective distributions.

asymmetry is defined by the expression:

$$\eta = \frac{A_H - A_L}{A_H + A_L}, \tag{5}$$

depending on the mass of the "heavy" and "light" PLF fission fragments (A_H & A_L). By selecting events with asymmetry ($\eta > 0.5$) one can be reasonably sure that statistical de-excitation of the fragments does not affect the assignment of the alignment direction.

The experimentally observed total multiplicity distributions for these two event classes

are presented in Fig. 15(a). Each distribution is approximately Gaussian in shape. The mean values which are denoted in the figure are different for the two distributions. The higher mean total multiplicity for forward splits of the PLF suggests that these events occur at a lower impact parameter with more projectile-target overlap. The predictions of the CLAT+GEMINI model are presented in Fig. 15(b) for comparison. To account for the response of the CHIMERA array, the calculation of the total multiplicity considered only charged particles with velocity greater than 3 cm/ns to remove from consideration those heavy fragments unlikely to leave the target foil and produce a measurable response in the detectors. Given such an approximation, the mean value of the distribution predicted by the model should be interpreted with care. However, it is encouraging to note that the mean of the predicted distributions are higher than those observed experimentally. This overestimate is in qualitative agreement with that presented for a different class of events in Fig. 8. The important result of the CLAT+GEMINI estimate of the mean total multiplicity is that the mean does not depend on the kinematics of the PLF fission, as expected.

To affect a direct comparison of the geometric production model with the experimental data, a novel analysis scheme was developed. The scheme leverages a number of the analysis details described above. By choosing "forward" and "backward" kinematic regions which are symmetric in the PLF rest frame, the contribution of equilibrated fission of the PLF to the yield in each case is expected to be constant. The yield ratio would be insensitive to the equilibrium contribution if this component is significantly less than the dynamic one. In addition the choice of asymmetric splits can be used to directly test the applicability of the geometric model. The reasoning for this is illustrated in Fig. 16. Two projectile-target collisions are considered: one at a semi-peripheral impact parameter (b_1) and the second at a more central impact parameter (b_2). If the interaction between the projectile and target were to split the projectile into two pieces whose sizes are determined by the geometric overlap, then a situation exists wherein both impact parameters (b_1 & b_2) may lead to the same asymmetry (η) of the PLF. However, these two collisions may lead to different kinematics if one assumes that the matter in the overlap region is slowed appreciably by the interaction. Namely the larger fragment will be faster than the smaller fragment for collisions at impact parameter (b_1) while the opposite ordering will take place for more central collisions. Given such a simple approximation of undoubtedly the complex collision process, the yield of the two event classes may be easily estimated. Of course one expects statistical fluctuations and

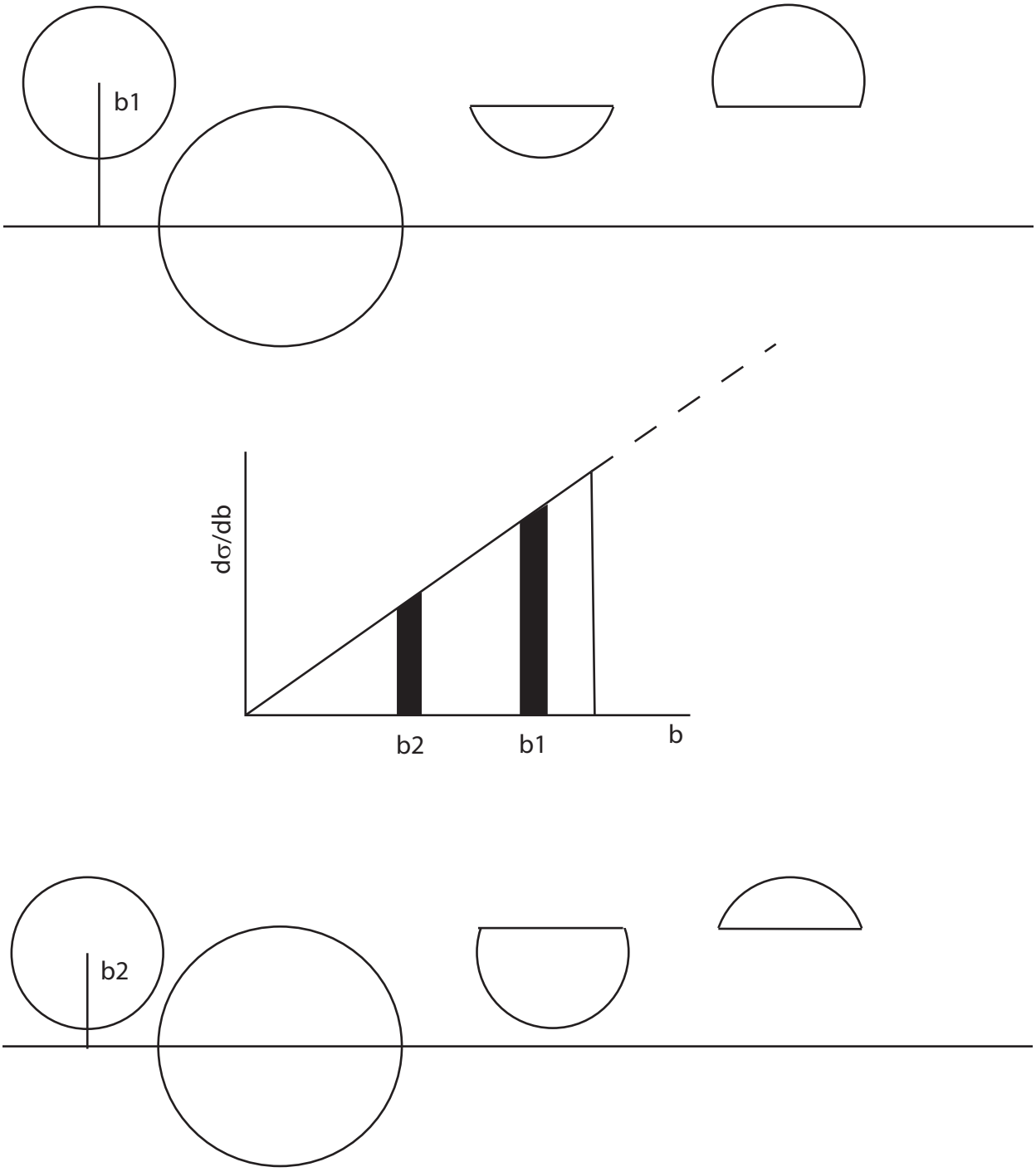

FIG. 16: Illustration of the geometric production model and how the asymmetry and the hierarchy of the split may be directly related to the yield for two event classes.

experimental uncertainties to broaden the asymmetry which would be observed in collisions at a fixed and sharply defined impact parameter. This concept is illustrated by solid bars of non-zero width which represent the integral yield for a range of PLF fragment asymmetry. The two bars represent the two possible ordering of the fragment sizes and speeds. The integral yield of one bar (Y) can be expressed as,

$$Y = \int_{b-\epsilon}^{b+\epsilon} \frac{d\sigma}{db} db. \tag{6}$$

In Eqn. 6 the parameter ϵ may represent the compound effect of statistical fluctuations and experimental uncertainties contributing to the choice of a asymmetry range.

To account for the contribution of PLFs which undergo equilibrium fission and otherwise mitigate systematic uncertainties associated with precise yield measurements, the ratio between the yield of the two event classes was determined for a series of PLF split asymmetries. The experimentally measured ratio between the yield of the backward (Y_b) to forward (Y_f) event classes is plotted versus the asymmetry of the PLF split in Fig. 17. The yield is observed to increase as the asymmetry of the split increases. This dependence is generally reproduced by the geometric model for the three lowest asymmetries considered. The predictions of the CLAT+GEMINI+CSR model are represented by the blue region. The model does not show a deviation from the a ratio of unity as the PLF split asymmetry is varied. The QMD+GEMINI+CSR model predictions are represented by the red region. Although the uncertainties are large, the QMD+GEMINI+CSR model predicts a trend opposite that observed in the data. It should be stressed that the error bars presented in the figure represent only the statistical uncertainties. Systematic uncertainties could contribute to the mean values, especially for the asymmetry range $0.7 \leq \eta \leq 0.8$. Competing process(es) such as fusion of the projectile and target at the presumably small impact parameter ($< b_2 >= 1.4$ fm) could deplete the "forward" PLF split component to the point where event pile-up contributes significantly to the measured ratio. Therefore, it may be appropriate to consider this latter data point to be a lower limit.

DISCUSSION

The inability of neither the CLAT+GEMINI+CSR model nor the QMD+GEMINI+CSR model reproduce the observed damping suggests that neither correctly accounts for the

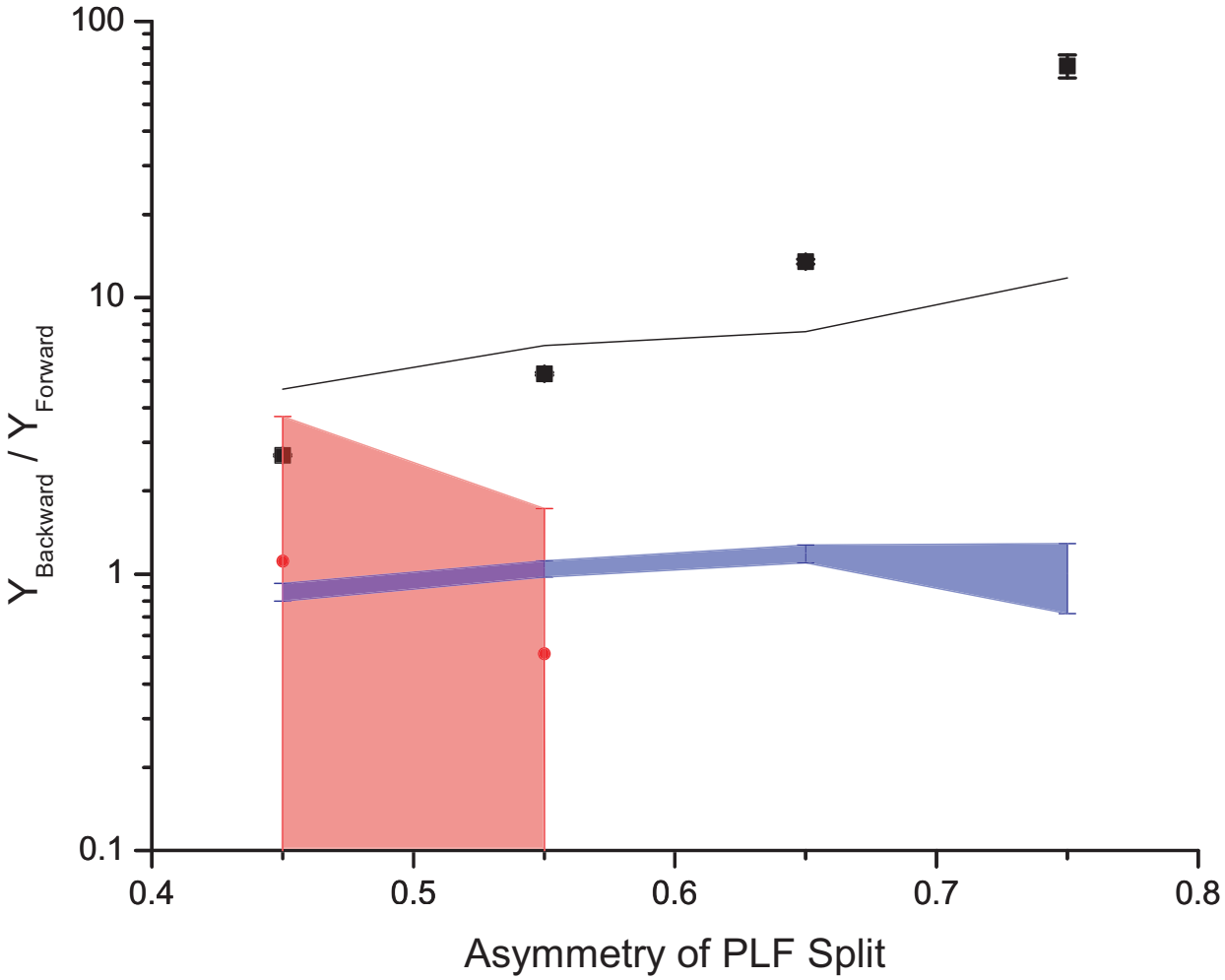

FIG. 17: Yield ratio of backward to forward splits of the PLF versus the asymmetry of the split. Solid symbols represent the experimental data. The solid black line denotes the predictions of the geometric model. Red and blue regions represent the predictions of the QMD+GEMINI+CSR and CLAT+GEMINI+CSR models respectively.

microscopic mechanisms which transform the projectile kinetic energy into internal degrees of freedom. It is difficult to conclude which parameter or physical process in these two models should be adjusted or added to account for the observed discrepancies. It is surprising to note that the QMD model predicts the opposite trend in the yield ratio. It seems that the model is more likely to predict the split in more central collisions. Perhaps this effect is related to the surprising similarity of the invariant cross section distributions for nearly all charged products (c.f. Fig. 4- 6 panels (e) and (f)).

Of the three models, the geometric production model reproduces the data relating the "forward" and "backward" yield components the best. However, it is premature to suggest that the PLF shears cleanly in the manner considered by the model. The model does not offer predictions for the excitation energy or laboratory scattering angle of the fragments produced in the split of the PLF. If these properties were known, a more realistic calculation accounting for the statistical de-excitation of these fragments and the CHIMERA detection efficiency could be performed. Geometric models attempting to predict these details have been attempted in the past with limited success[8]. Therefore, the present implementation is only helpful in interpreting basic trends in the data.

A process such as "dynamic fission" of the PLF is not considered explicitly by the geometric production model, and is still only conceptual. However, the relatively simple relationship between the asymmetry in the split of the PLF and collision centrality suggested by the analysis presented above, may provide a framework to realize such a model. The trend in the data appears to suggest a relationship between the degree of projectile-target overlap and the direct production of IMFs exists. A better understanding of the perturbation applied to the projectile in the collision with the target could also prove important to explorations of the dissipation mechanism(s) important in heavy-ion collisions at medium bombarding energies.

CONCLUSION

Events consistent with the split of the PLF formed in reactions of ^{48}Ca+^{124}Sn at 45 AMeV were isolated. The kinematics of the products produced in the split were analyzed and found inconsistent with the systematics expected for asymmetric fission of an equilibrated PLF. The fragment size and velocity hierarchy was found to be sensitive to the multiplicity of charged particles, an observable canonically associated with the reaction centrality. A novel analysis scheme suggests that the split of the PLF may arise from the geometrical overlap of the projectile and target.

This work was supported by the US Department of Energy Grant No. DE-FG02-88ER40414.

[1] D. R. Bowman et al., Phys. Rev. Lett. **67**, 1527 (1991).

[2] R. Charity, URL `www.chemistry.wustl.edu/~rc/`.

[3] J. Toke et al., Phys Rev. C **67**, 034609 (2003).

[4] W. A. Friedman and W. G. Lynch, Phys. Rev. C **28**, 16 (1983).

[5] C. Barbagallo et al., Z. Phys. **A324**, 97 (1986).

[6] W. U. Schroder and J. R. Huizenga, *Treatise on Heavy-Ion Science*, vol. 2 (Plenum, New York, 1984).

[7] H. Fuchs and K. Möhring, Rep. Prog. Phys. **57**, 231 (1994).

[8] B. Borderie et al., Ann. Phys. Fr. **15**, 287 (1990).

[9] E. De Filippo et al., Phys. Rev. C **71**, 044602 (2005).

[10] E. De Filippo et al., Phys. Rev. C **71**, 064604 (2005).

[11] J. Colin et al., Phys. Rev. C **67**, 064603 (2003).

[12] W. U. Schroder et al., Nucl. Sci. Res. Conf. Ser. **11**, 255 (1987).

[13] J. Lukasik and Z. Majka, Acta Phys. Pol. **24**, 1959 (1993).

[14] M. Alderighi et al., Nucl. Instr. Meth. **A489**, 257 (2002).

[15] L. C. Northcliffe and F. Schilling, Nucl. Data Tables **A7**, 233 (1970).

[16] F. Huber et al., Atomic and Nucl. Data Tables **46** (1990).

[17] C. F. Williamson et al., Tech. Rep. R-3042, CEA (1996).

[18] J. F. Janni, Atomic and Nucl. Data Tables **27**, 341 (1982).

[19] A. Pagano et al., Nucl. Phys. **A681**, 331 (2001).

[20] P. Russotto, Ph.D. thesis, University of Catania (2006).

[21] E. La Guidara, Ph.D. thesis, University of Catania (2004).

[22] J. Blocki et al., Ann. Phys. NY **105**, 427 (1977).

[23] J. Randrup, Nucl. Phys. **A307**, 319 (1978).

[24] J. Randrup, Nucl. Phys. **A327**, 490 (1979).

[25] J. Randrup, Nucl. Phys. **A383**, 468 (1982).

[26] J. Randrup, Ann. Phys. NY **112**, 356 (1978).

[27] J. Blocki et al., Ann. Phys. NY **113**, 330 (1978).

[28] J. Lukasik, Ph.D. thesis, Jagellonian University, Cracow (1993).

[29] M. Colonna et al., Phys. Rev. C **57**, 1410 (1998).

[30] V. Baran et al., Nucl. Phys. A **A632**, 632 (1998).

[31] A. S. Goldhaber, Phys. Lett. **B53**, 306 (1974).

[32] A. Bonasera et al., Nucl. Phys. **A463**, 653 (1987).

[33] W. Hauser and H. Feshbach, Phys. Rev. **87**, 366 (1952).

[34] A. J. Sierk, Phys. Rev. Lett. **55**, 582 (1985).

[35] L. G. Moretto and G. J. Wozniak, Prog. in Part. and Nucl. Phys. **21**, 401 (1988).

[36] R. Dayras et al., Nucl. Phys. **A460**, 299 (1986).

[37] J. Wilczynski, Phys. Lett. B **47**, 484 (1973).

[38] R. Vandenbosch and J. R. Huizenga, *Nuclear Fission* (Academic Press, New York, 1973).

[39] V. E. Viola et al., Phys. Rev. C **31**, 1550 (1985).

[40] D. J. Hinde et al., Nucl. Phys. **A472**, 318 (1987).

NSTAR-A Capture Gated Plastic Neutron Detector

I. A. Pawełczak, J. Tõke, E. Henry, M. J. Quinlan, H. Singh, and W. U. Schröder
Departments of Chemistry and Physics, University of Rochester, Rochester, NY 14627

Abstract

Development and performance of a new Gd-loaded plastic-scintillator neutron detector are discussed. The NSTAR ("Neutron Sandwich Transmuter/Activation-γ Radiator") detector has high detection efficiency for neutrons, from thermal to MeV energies. The detector is scalable, economic to construct of environmentally benign components, and can be ruggedized. The NSTAR operating principle is similar to that of Gd-loaded *liquid* scintillation detectors, where the scintillator has dual functions as neutron moderator and sensor of delayed capture γ-rays, but spatially separates scintillator from neutron converter components. The time dependent NSTAR response to neutrons consists of a prompt, energy related light flash followed by a delayed signal characteristic in both light output and delay time. This feature provides the basis for γ-neutron discrimination and for event-by-event multiplicity determination. Prototype detector modules consist of [12 x 20 x (50 or 100) cm^3] stacks of plastic scintillator sheets (Saint Gobain BC-408) alternating with thin Gd-loaded (0.5 wt. %) converter films (PDMS-SYLGARD 184), viewed by fast photomultipliers (Philips XP2041). NSTAR tests with Am/Be and pulsed-beam DD neutrons are in good agreement with theoretical estimates based on neutron transport simulations. Characteristics of the detector module include an average neutron capture time of $\langle t_c \rangle = (21.7 \pm 0.2)$ μs and a detection efficiency of $\varepsilon = (26 \pm 3)$ % for DD neutrons. The NSTAR has been applied to determine the event-by-event multiplicity distribution of DD generator neutron bursts.

Keywords:
Neutron detectors
Gd loaded scintillators
Neutron multiplicity meters